ELPH

Annual Report 2020

Research Center for Electron Photon Science
Tohoku University

Preface

This booklet summarizes all activities of the Research Center for Electron-Photon Science (ELPH) for the fiscal year 2020. Together with the ELPH Annual Report for activities of individual faculty members published separately, we intend to provide a broad overview of our activities, including research and facility operations.

On April 1, 2021, I was newly appointed as a director of ELPH. Since then, I have been continuing efforts to maximize the use of the electron accelerators and the smooth operation of the facility in order to maximize research results through joint research and collaboration.

ELPH is a university-based accelerator facility and operates a 1.3 GeV electron booster-synchrotron and a high-power (10 kW) 60-MeV electron linear accelerator. Our facility has been a 'Joint Usage/Research Center' certified by the Ministry of Education, Culture, Sports, Science, and Technology (MEXT) since 2011 and has provided easy access to electron accelerators to researchers in Japan and abroad to promote cutting-edge research.

Due to the global outbreak of the Coronavirus, our activities were severely restricted in many ways through FY 2020. The government's declaration of a state of emergency forced us further to avoid experimental activities, and almost all face-to-face activities, such as seminars, workshops, and lectures, were switched to online.

Even under such difficult circumstances, however, we attempted a series of hadron-physics experiments with the minimum number of personnel required to operate the accelerator and take data. We finally succeeded in conducting long-term physics experiments. Although many of the experiments by external users were not scheduled to follow the infection control measures required by Tohoku University, we made every effort to ensure that local-user experiments could be carried out under challenging conditions.

As a result, we were able to secure more than 2,000 hours of accelerator operation time in FY2020, the same as in previous years, and the number of users reached 1,300 day*people/year, the largest number since 2011. I would like to take this opportunity to thank all of our collaborators for their support.

Even during the corona epidemic, the importance of outreach activities to the general public has led us to create a "virtual facility tour" video and make it available on our website so that people interested in our facility can view the accelerators and the large research setups in each laboratory at any time.

Even today, research and educational activities are still limited because the Coronavirus has not been yet completely controlled. We, however, will make efforts to continue stimulating joint use and research further and developing new research fields with our accelerators.

I would like to have your continued warm support.

Toshimi Suda,
Director, Research Center for Electron Photon Science, Tohoku University

ELPH Annual Report 2020

Contents

I. Papers

Ⅱ. Status Report

Ⅲ. List of Publication

Ⅳ. Members of Committees

Ⅴ. Approved Experiments

I. Papers

(ELPH Experiment : #2933)

Measurement of Charge Collection Efficiency of SOI Pixel Sensor with PDD structure

Miho Yamada[1], Ryuhei Abe[2], Shikie Iwanami[2], Hitoshi Murayama[2], Kazuhiko Hara[2], Toru Tsuboyama[3], Akimasa Ishikawa[3], and Ayaki Takeda[4]

[1]*Tokyo Metropolitan College of Industrial Technology, Arakawa, 116-8523*
[2]*Graduate School of Pure and Applied Sciences, University of Tsukuba, Tsukuba, 305-8571*
[3]*Institute of Particle and Nuclear Studies, High Energy Accelerator Research Organization, Tsukuba, 305-0801*
[4]*Faculty of Engineering, University of Miyazaki, Miyazaki, 889-2192*

Charge collection efficiency and detection efficiency of an SOI pixel sensor, XRPIX6E, which has Pinned Depleted Diode (PDD) structure have been measured. The SOI pixel detector is a monolithic type sensor, which is composed of two silicon wafers, one with a signal readout circuit and another acting as a radiation sensor, the two isolated by a SiO_2 layer. The PDD structure consists of multi layers of p/n implants under SiO_2 layer. PDD suppresses the sensor leak current, allows high speed charge collection, and results in high efficiency charge collection. XRPIX is being designed as an X-ray imaging detector for astronomy physics. We expect that PDD improves radiation tolerance against total ionizing dose (TID) effect since the p/n implants could be used for applying voltages to control potential under the SiO_2 layer to compensate the potential shift induced by TID effect. XRPIX has also a good sensitivity to detect high energy charged particles. We studied the charge collection and charge share properties of XRPIX for developing of a high position resolution pixel detector to be used for high-energy collider experiments.

§1. Introduction

Monolithic type pixel sensors are being developed for high-energy collider experiments such as ILC, Belle II upgrade, and so on. High spatial resolution and low material budge are key considerations for highly efficient particle identification and event reconstruction. As monolithic type pixel detector integrates signal readout circuit and radiation sensor volume in (typically) single wafer, it has an advantage of realizing small pixel size and suppressing multiple scattering; thus high spatial-resolution vertexing/tracking and high efficient event reconstruction, including heavy flavor particles, could be expected. We have been developing monolithic pixel detectors by utilizing fully-depleted Silicon-on-Insulator (SOI) CMOS technology (0.2 µm process of Lapis Semiconductor Co., Ltd.). FPIX2, an SOI sensor developed by us, performed a position resolution of 0.65 µm [2], which is the world best value performed by semiconductor detectors. SOFIST, an ILC prototype vertex detector, achieved both high-position resolution and hit-time recording capability, fulfilling the specifications adopted to the ILC bunch collision structure. We obtained 1.4 µm of position resolution and 1.55 µs of time resolution by SOFIST1 and 2, respec-

tively [3, 4]. Remaining development issues are high position resolution to be achieved with a thinned sensor and high radiation tolerance. A sensor with a thickness of 50 µm should achieve a position resolution of 10 µm while implementing the necessary functions inside the pixel area. It is expected that Pinned Depleted Diode (PDD) structure achieves both high radiation tolerance and high spatial resolution.

PDD is a structure having fixed potential regions through buried p/n-wells (BPW/BNW) with high impurity concentrations implanted under the buried oxide (BOX) layer as shown in Figure 1 [1]. An fixed negative potential suppresses the potential of positive charges in the BOX induced by TID effect. Otherwise, the positive charges cause malfunctioning of MOSFET signal readout circuit implemented above the BOX layer. PDD has multiple layers of different impurity concentrations surrounding the sense node to form a stepped potential for efficient charge collection. The charge collection efficiency and charge share depend on the shape of the stepped potential. In Figure 1, $V_{\mathrm{BPW\_PIX}}$ is to vary the voltage for the stepped potential. One of the testbeam purposes is to evaluate the charge collection/share by varying $V_{\mathrm{BPW\_PIX}}$ for studying the effects of the PDD structure in performing high spatial resolution.

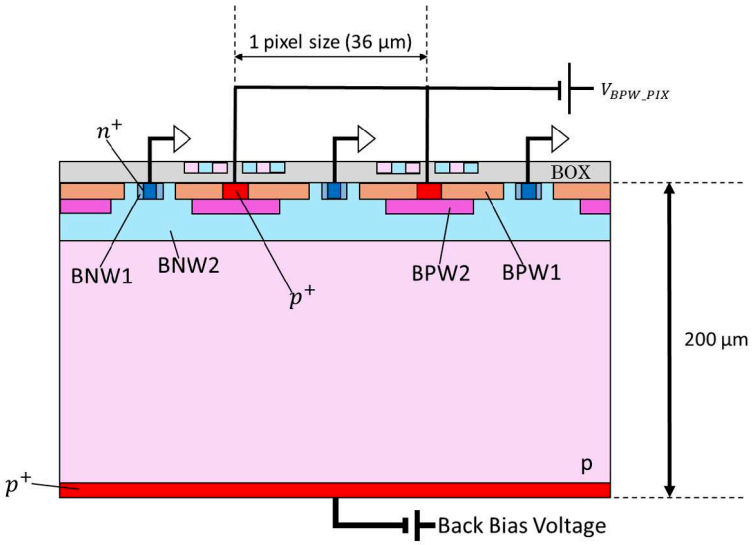

Fig.1. Cross section of PDD structure (XRPIX6E). n^+ with BNW1 is the pixel sense node. The PDD structure of XRPIX6E consists of p^+, BPW1, BPW2 and BNW2. The voltages of BPW1 and BPW2 are pinned by $V_{\mathrm{BPW\_PIX}}$. The voltage of BNW2 is fixed by another electrode surrounding the entire pixel array. The back bias voltage is for depleting the sensor. The sensor is 200 µm thick.

§2. Experimental Setup

We have tested XRPIX6E [1] which has PDD structure with positrons of ELPH for evaluating charge collection and charge share. Main XRPIX6E parameters are shown in Table 1. Signal integration and reset are repeated periodically until XRPIX6E receives an event trigger, then readout of all the pixels is initiated. The frame rate is about 30 frames/s. The XRPIX6E chip is covered by a Copper jacket as illustrated in Figure 2 for cooling down the sensor to 0 °C. Nitrogen gas is flew inside the Copper jacket

to minimize humidity to avoid condensation on the chip surface. There are holes in the Cu jacket, chip socket, sub-board, thermal insulator and the Al plate to suppress multiple scattering of the beam.

The voltage for the sensor back bias is -200 V and that for BPW ($V_{\mathrm{BPW\_PIX}}$) is -1.6 V as nominal. $V_{\mathrm{BPW\_PIX}}$ is varied from -0.4 V to -1.6 V for evaluating the charge collection.

Table 1. Main sensor parameters of XRPIX6E

parameter	value
Chip size	4.45 mm $\times$ 4.45 mm
Active area	1.7 mm $\times$ 1.7 mm
Pixel size	36 µm $\times$ 36 µm
Pixel array	48 $\times$ 48 pixels
Sensor thickness	200 µm
Sensor wafer	p-type FZ ($>$ 25 k$\Omega \cdot$ cm)

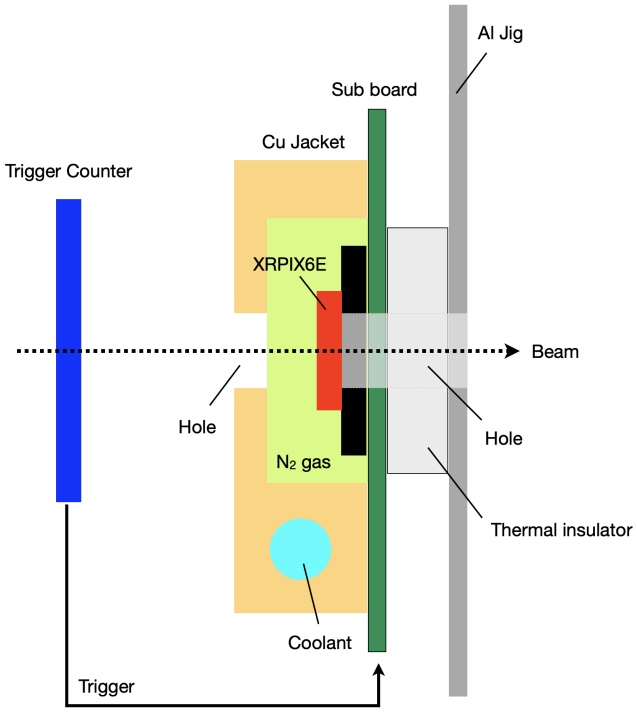

Fig.2. Setup in the beam test.

§3. Result

3.1 Detection of Minimum Ionizing Particles

The XRPIX6E is tested on detection of minimum ionizing particles (MIPs) of 600 MeV/c of positron beam. The pixel hit is defined if the signal exceeds a threshold of the comparator implemented in each pixel. If the neighboring pixels are defined also as the hit, the charges of those two or more pixels are added to construct the cluster charge since the charge is shared among multiple pixels. The cluster charge is shown in Figure 3. Most probable value of 2410 $\pm$ 11 ADC is obtained by fitting with the

Landau distribution. The expected cluster charge is calculated using the pixel gain, e-h pair creation energy, number of induced e-h pairs per 1 μm and the sensor thickness as follows;

$$47/1000 \text{ ADC/eV} \times 3.6 \text{ eV/e-h} \times 80 \text{ e-h/μm} \times 200 \text{ μm} \sim 2700 \text{ ADC} \quad (1)$$

We have successfully detected the MIP signal with the SOI sensor with PDD structure and observed most of the charges are collected.

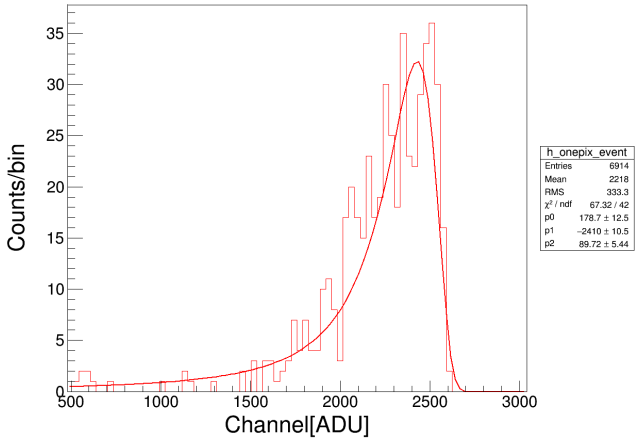

Fig.3. Cluster charge of MIPs.

3.2 Charge Collection

The potential around the sense node depends on the $V_{\text{BPW\_PIX}}$ as mentioned above. Hit position is reconstructed by weighted center of the charges. The cluster charge distribution as a function of $V_{\text{BPW\_PIX}}$ has been evaluated as shown in Figure 4 for different $V_{\text{BPW\_PIX}}$ values. The most probable values of all the distributions stay not change much, but the sigma decreases with increasing $V_{\text{BPW\_PIX}}$ as shown in Figure 5, which is explained by the decrease of the distribution tail. It is evident that $V_{\text{BPW\_PIX}}$ can control the charge collection/share. The increase of charge collection efficiency with $V_{\text{BPW\_PIX}}$ for the cases when the beam traverses the pixel boundary explains the observed changes of the distribution.

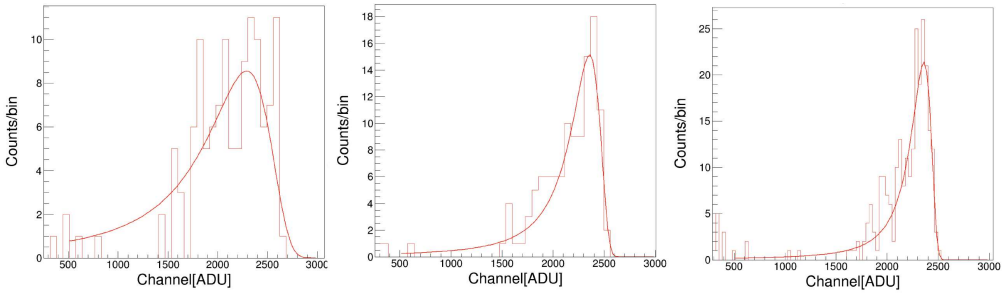

(a) (b) (c)

Fig.4. Cluster charge as a function of $V_{\text{BPW\_PIX}}$. (a)$V_{\text{BPW\_PIX}} = -0.4$ V , (b)$V_{\text{BPW\_PIX}} = -1.0$ V , (c)$V_{\text{BPW\_PIX}} = -1.6$ V .

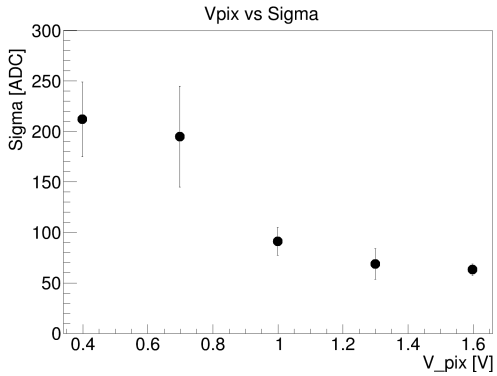

Fig.5. Sigma of the cluster charge as a function of $V_{\mathrm{BPW\_PIX}}$.

Acknowledgment

We would like to express our thanks to the facility staff of Research Center for Electron Photon Science (ELPH) at Tohoku University for providing high quality electron beam. The authors also acknowledge Prof. Takeshi Tsuru of Kyoto University for providing us high quality XRPIX6E chips, and valuable advice and important work done by his graduate students.

References

[1] S. Harada *et al.*, Nucl. Instr. and Meth. A **924** (2019).

[2] D. Sekigawa *et al.*, Springer Proc. in Phys. **213** (2018).

[3] M. Yamada *et al.*, JINST 13 C01037 (2018).

[4] S. Ono *et al.*, presented at PIXEL2018, Taipei, 2018.

(ELPH Experiment : #2915, #2943)

Performance evaluation of electron-multiplier tubes using a high-intensity electron beam for the T2K muon monitor

Y. Ashida[1], A.K. Ichikawa[2], M. Ishitsuka[3], N. Izumi[3], T. Honjo[4], T. Kikawa[1], T. Kobata[4], T. Matsubara[5], H. Nakamura[3], and K. Yasutome[1]

[1]*Department of Physics, Kyoto University, Kyoto, 606-8502*
[2]*Department of Physics, Tohoku University, Sendai, 980-8578*
[3]*Department of Physics, Tokyo University of Science, Noda, Chiba,278-8510*
[4]*Department of Physics, Osaka City University, Osaka, 558-8585*
[5]*Institute of Particle and Nuclear Studies, High Energy Accelerator Research Organization(KEK), Tsukuba, 305-0801*

The electron-multiplier tube (EMT) is a candidate device of the muon monitor for the future high-intensity beam operation in the T2K experiment. Performances of the EMT were evaluated using a high-intensity 90 MeV electron beam from the injector LINAC at ELPH, Tohoku University in 2019-2020. The EMT was found to satisfy requirements of linearity and radiation tolerance for the future high-intensity beam operation in the T2K experiment. However, there observed about 2% decrease of the signal at the beginning of the beam exposure. This initial decrease will be studied in more detail in the next beam test in 2021 for a practical application of the EMT as the muon monitor.

§1. Introduction

The T2K experiment is a long-baseline neutrino oscillation experiment to measure the neutrino oscillation parameters [1]. An intense (anti-)neutrino beam is produced at J-PARC (Japan Proton Accelerator Research Complex) and measured by the far detector, Super-Kamiokande, which is located 295 km away from J-PARC. The beam protons from the J-PARC accelerator impinge a graphite target, and charged pions are produced. Those pions decay in flight into pairs of a muon and a muon (anti-)neutrino.

The muon monitor is placed at 118 m from the target and measures the profile and intensity of the muon beam to indirectly monitor the neutrino production in real time [2]. The current muon monitor consists of 7×7 arrays of Si PIN photodiodes and ionization chambers. They have shown an excellent performance since the beginning of the T2K experiment [3]. The J-PARC main ring beam power as of 2021 is 510 kW. It will be increased up to 1.3 MW in the future [4, 5]. The Si PIN photodiodes and ionization chambers will not be applicable for the future high-intensity operation because of their issues of radiation tolerance and linearity, respectively.

As a candidate for a new muon monitor device, we have proposed and studied the electron-multiplier tube (EMT), which is equivalent to a photomultiplier tube without a photocathode. The EMTs were installed in the J-PARC muon monitor pit in 2017 and showed a good response to the muon beam [6]. In addition, to precisely evaluate the performance of the EMT and conclude its feasibility as the new

muon monitor device, electron beam tests were performed at ELPH, Tohoku University in two periods: November 27-28 in 2019 (#2915) and November 10-11 in 2020 (#2943).

§2. Experimental Setup

2.1 Beamline and detectors

We used a 90 MeV electron beam from the injector LINAC at ELPH. Figure 1 shows the experimental setup of the beam test. We utilized four kinds of detectors.

- The EMT (custom-made based on Hamamatsu R9880U) connected to a dedicated divider circuit is the main detector to be tested.
- Two Si sensors (Hamamatsu S3590-08), the same type as the current muon monitor, are used for comparisons to the EMT.
- A Current Transformer (CT) measures the beam current.
- An 8×8 Si array (Hamamatsu S13620-02) measures the beam profile.

The CT sat on the most upstream of the beam. The EMT, Si sensors, and Si array were attached on electric linear actuators so that they can be moved on and off the beam by remote control. Signals from the detectors were recorded by waveform digitizers (CAEN DT5725 and DT5740), after amplification or attenuation in some cases. This detector arrangement was optimized by FLUKA simulations to minimize the effect of the multiple scattering.

2.2 Beam profile and intensity

As a result of the beam profile measurement by the Si array in the first period of the beam test, the beam width was found to be $\sigma = 1.5$ mm, which is much smaller than the detector size (∼10 mm). In order to irradiate the detector uniformly, the EMT and Si were moved horizontally and vertically by the actuators during the beam exposure in the second period of the beam test.

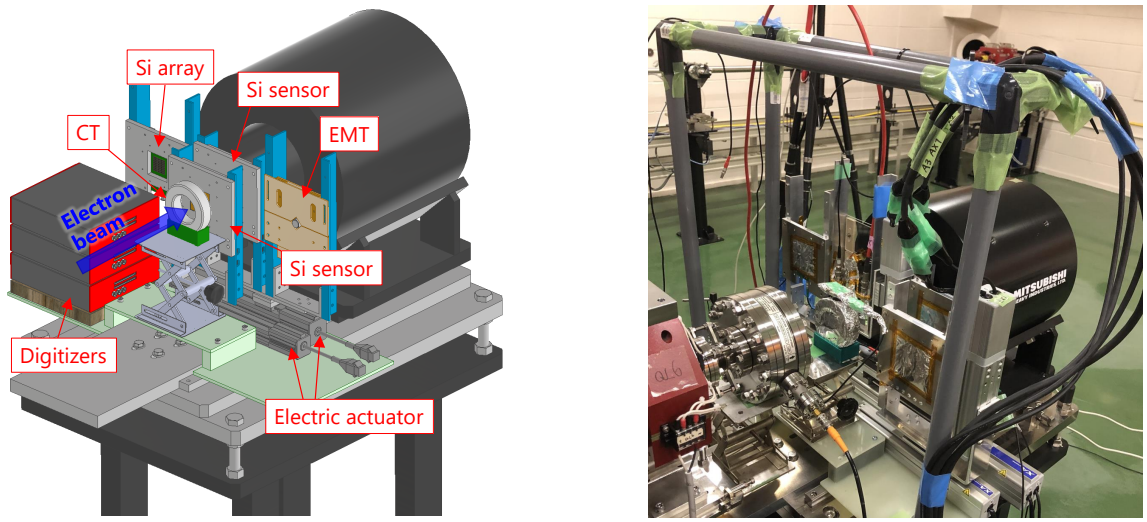

Fig.1. Design (left) and photograph (right) of the experimental setup of the beam test.

There were three settings of the beam intensity, which roughly correspond to 1 pC, 300 pC, and 20 nC per pulse. Since the 1 pC/pulse is comparable to the J-PARC muon beam intensity, the detector response including linearity was evaluated in this setting. In the 300 pC/pulse and 20 nC/pulse settings, a large amount of the electron beam irradiated the detectors in a short time for studies of the stability and radiation tolerance. First, beam operations with the 1 pC/pulse and 300 pC/pulse settings were alternated to check the initial response for each EMT. Then, beam operations with the 1 pC/pulse and 20 nC/pulse settings were alternated to evaluate the radiation tolerance.

§3. Results

3.1 Linearity

The linearities of the Si and EMT were evaluated by comparisons of their signal yields to the beam current as shown in Fig. 2. The beam current was determined by a frequency-domain analysis of the CT signal waveform since it is expected to have a good linear response to the beam current. The Si and EMT yields were obtained by the integral of their signal waveforms. Although the linearity of the Si is good up to the intensity equivalent to the current J-PARC muon beam, it gets worse from around the intensity equivalent to the future J-PARC muon beam. On the other hand, the EMT has a good linearity up to much higher intensity.

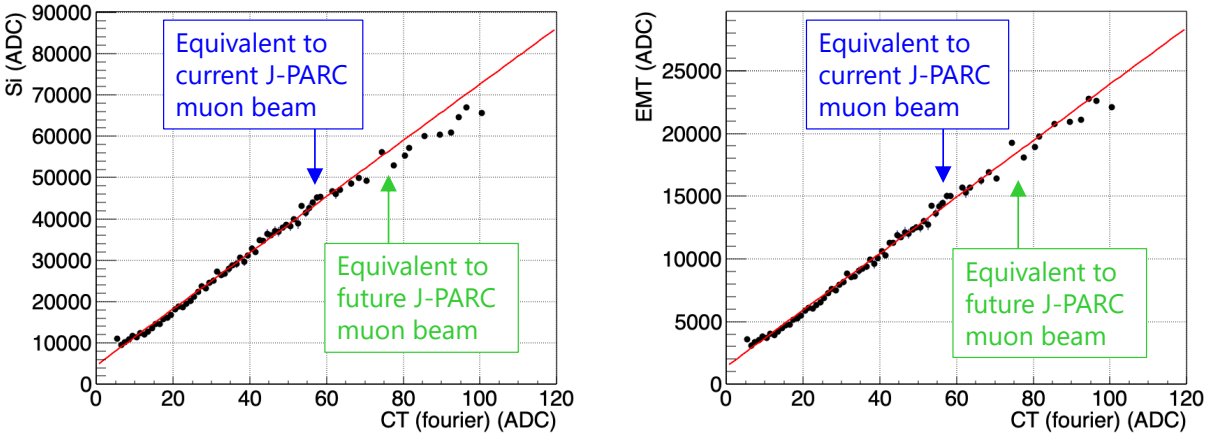

Fig.2. Signal yields of the Si (left) and EMT (right) compared with that of the CT which is equivalent to the beam current. The vertical axes represent the average yields of the Si and EMT in given ranges of the CT yield.

3.2 Radiation tolerance

Figure 3 shows the changes of the EMT yield with the high-intensity electron beam irradiation. The equivalent operation days at J-PARC were estimated as follows.

1. The total amount of the delivered electron beam was calculated by summing up the pulse beam currents determined by the CT.
2. The efficiency of the electron beam hitting the detector was estimated from the beam profile measured by the Si array and multiplied to the amount of the electron beam.

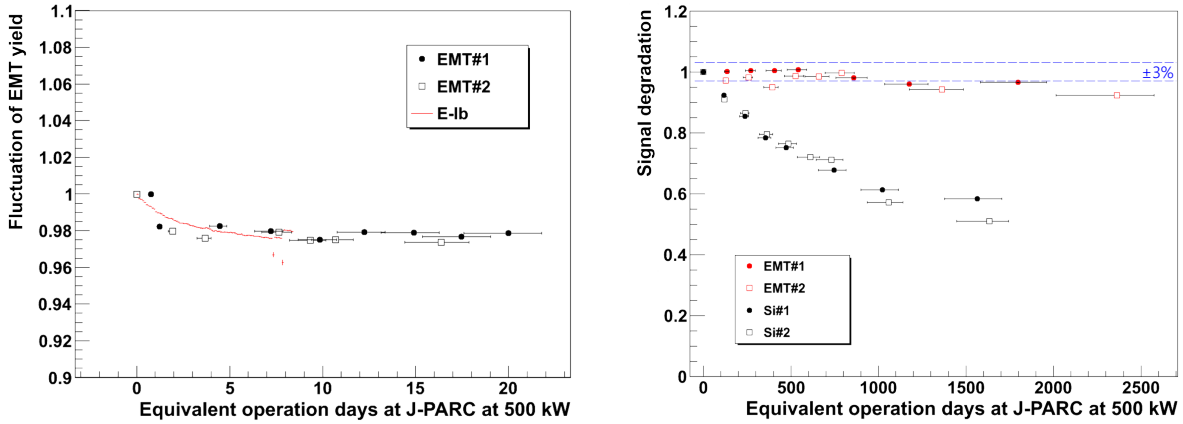

Fig.3. Changes of the EMT yield with the high-intensity electron beam irradiation. Left: results of alternate beam operations with the 1 pC/pulse and 300 pC/pulse settings compared with the result of the test operation of the EMT at J-PARC (E-lb). Right: results of alternate beam operations with the 1 pC/pulse and 20 nC/pulse settings compared with the Si yield.

3. It was converted into the equivalent operation days at J-PARC using the number of muons on the detector at the J-PARC 500 kW beam operation and the ratio of the dE/dx of the 90 MeV electron to the MIP muon.

The response of the EMT is stable within ±3% up to the accumulated beam exposure corresponding to 1000 days of the J-PARC operation at 500 kW, which is also equivalent to 380 days of the J-PARC operation at 1.3 MW. On the other hand, the response of the Si decreases rapidly. From these results, we concluded that the linearity and radiation tolerance of the EMT are much better than those of the Si, and fulfill the requirements for the future high-intensity operation in the T2K experiment [7, 8]. However, there was about 2% decrease of the EMT signal yield at the beginning of the beam exposure. Similar behaviors were observed in the test operation of the EMT at J-PARC [6]. Since this effect may be a problem for a practical application of the EMT as the muon monitor device, it is necessary to be studied in more detail in the next beam test in 2021.

§4. Summary

The muon monitor made of Si sensors and ionization chambers has shown the excellent performance in the T2K experiment. However, it has issues of linearity and radiation tolerance for the future high-intensity beam operation. The EMT is a candidate for the muon monitor device for the high-intensity operation. We evaluated the performances of the EMT using a high-intensity 90 MeV electron beam at ELPH, Tohoku University. The linearity and radiation tolerance of the EMT are found to be much better than those of the Si, and fulfill the requirements for the future high-intensity operation in the T2K experiment. However, we observed about 2% decrease of the signal at the beginning of the beam exposure. Although similar decreases were observed in the test operation of the EMT at J-PARC, it is not yet well understood. In addition, we also do not understand the main cause of the radiation damage

of the EMT and the change of the electron beam profile at different intensities at ELPH. They will be investigated in the next beam test in 2021.

Acknowledgment

The authors are grateful to the ELPH accelerator staffs for supplying a superb beam, especially to Shigeru Kashiwagi, Takatsugu Ishikawa, and Manabu Miyabe for their great support and coordination. This work was supported by MEXT KAKENHI Grant Numbers 25105002, 16H06288, 15J01714, and 17J06141, and the U.S.-Japan Cooperation Program in High Energy Physics.

References

[1] K. Abe *et al.*, Nucl. Instr. Meth. A **659** 106-135 (2011)
[2] K. Matsuoka *et al.*, Nucl. Instr. Meth. A **624** 591-600 (2010)
[3] K. Suzuki *et al.*, Prog. Theor. Exp. Phys. **2015** 5, 053C01 (2015)
[4] K. Abe *et al.*, arXiv:1609.04111 (2016)
[5] K. Abe *et al.*, arXiv:1908.05141 (2019)
[6] Y. Ashida *et al.*, Prog. Theor. Exp. Phys. **2018** 10, 103H01 (2018)
[7] T. Honjo, master thesis in Osaka City University (2021)
[8] N. Izumi, master thesis in Tokyo University of Science (2021)

(ELPH Experiment : #2944)

Study of high-rate capabilities of CITIROC1A and PETIROC2A ASICs

R. Honda[1], T. Ishikawa[2], S. Kajikawa[3], Y. Kimura[4], H. Noumi[5], K. Shirotori[5], R. Tatsumi[4], and N. Tomida[5]

[1]*Institute of Particle and Nuclear Studies(IPNS), High Energy Accelerator Research Organization (KEK), Tsukuba 305-0801, Japan*
[2]*Research Center for Electron Photon Science(ELPH), Tohoku University, Sendai 982-0826, Japan*
[3]*Department of Physics, Tohoku University, Sendai 980-8578, Japan*
[4]*Department of Physics, Osaka University, Toyonaka 560-0043, Japan*
[5]*Research Center for Nuclear Physics (RCNP), Osaka University, Ibaraki, Osaka 567-0047, Japan*

We investigated high-rate capabilities of application specific integrated circuit (ASIC), CITIROC1A and PETIROC2A, developed by Weeroc to select a suitable readout ASIC for a scintillating fiber detector used in a charmed-baryon spectroscopy at J-PARC. A test experiment was conducted at the Research Center for Electron Photon Science (ELPH). Scintillating fiber detectors consisting the fibers with diameters of 1.0 mm and 0.5 mm were irradiated with electrons and positrons converted from the high-intensity bremsstrahlung-photon beam. Multi-pixel photon counter (MPPC) attached to a fiber end surface were read by CITIROC1A and PETIROC2A under the high-rate condition up to 1.1 MHz/mm detector segment corresponding to the input signal rate of 1.1 MHz. The signal loss ratio and the dead time due to signal pile-up in CITIRCO2A were 3.9% and 37 ns, respectively. Significant second pulse was observed caused by oscillation of the pre-amplifier in PETIROC2A, and it appears around 60 ns after the first pulse.

§1. Introduction

We are planning to conduct an experiment for charmed-baryon spectroscopy at the Japan Proton Accelerator Research Complex (J-PARC) as the J-PARC E50 experiment [1] by utilizing the high-intensity, high-momentum pion beam delivered at the high-momentum beam line at in the Hadron Experimental Facility [2]. The charmed-baryons (Y_c^{*+}) is produced via the meson induced reaction, $\pi^- p \to D^{*-} Y_c^{*+}$, where the 20 GeV/$c$ pion beam is driven on a 4-g/cm^2 liquid hydrogen target. The Y_c^{*+} mass spectrum is obtained by the missing mass method from the four-momenta of a beam pion, a target proton, a scattered D^{*-}.

As the production cross section of Y_c^{*+} is expected to be as small as 1 nb [3], the high-intensity, 30 MHz pion beam is a key of the E50 experiment to compensate the small cross section. The beam rate at the target position is expected to be 1 MHz/mm. Thus, we developed scintillating fiber detectors having

high-rate capability at 1 MHz/mm as a tracking device to measure a beam trajectory. The intrinsic timing resolution of 1 ns in sigma and the detection efficiency of 97% are required to fiber detectors under the 1 MHz/mm condition. There are two kinds of scintillating fiber detectors, which are installed in the beam line; the focal plane fiber tracker consists of fibers with 1 mm diameters and is used to measure a beam momentum; the beam line fiber tracker consists of fiber with 0.5 mm diameters and is installed just before the target to reconstruct a reaction vertex. In 2018, we tested a prototype fiber tracker consisted of scintillating fibers with 1-mm diameters at Research Center for Electron Photon Science (ELPH) using high-rate electrons and positrons up to 1.9 MHz/mm [4]. In this test, an Application Specific Integrated Circuit (AISC), Extended Analogue SiPM ReadOut Chip (EASIROC) [5] was adopted for amplifying and shaping signals from photo detectors, which were multi-pixel photon counter (MPPC), Hamamatsu Photonics S13360-3050. The obtained timing resolution at the 1 MHz/mm condition was sufficiently good; however, the detection efficiency of 95% was lower than the requirement. The shaped signal in EASIRIOC was not enough narrow to keep the detection efficiency, and thus the efficiency was decreased due to signal pileup. In addition, we found that EASIROC shows a strange behavior under the high-rate condition, that is, an amplified signal width is 30-40% decreased as the incoming signal rate is increased. This implies that the amplified signal in EASIROC becomes smaller when the input signal rate is high. Detail description was given in Ref. [4]. Unfortunately, we could not find a reason of this behavior, but we concluded that EASIROC is not suitable for the readout ASIC of the scintillating fiber trackers in the E50 experiment.

We selected two candidates of the readout ASIC. One is CITIROC1A [6], which is updated EASIROC and has a similar architecture that of EASIROC. The other is PETIROC2A [7], which is developed for a time-of-flight (TOF) measurement for TOF positron emission tomography (TOF PET). A Front-end electronics (FEE) was developed to evaluated CITIROC1A and PETIROC2A. We carried out a test experiment on the second photon beam line at ELPH using electrons and positrons converted from bremsstrahlung-photon beam. FEEs with PETIROC2A and CITIROC1A were tested with the scintillating fiber detectors to study performances of ASICs under the high-rate condition.

§2. CITIROC1A and PETIROC2A

CITIROC1A is an updated EASIROC. Its architecture is almost the same as that of EASIROC. The block diagram of CITIROC is illustrated in Fig. 1. The number of input channel of CITIROC is 32. The programmable 8-bit digital to analog converter (DAC) called InputDAC is installed at the input stage. InputDAC provides DC voltage to adjust bias voltage of a photo sensor. CITIROC has two amplification lines called high gain and low gain. Both lines have a pre-amplifier and a slow shaper (SSH); the slow shaper is used for a charge measurement. The pre-amplifier gain and slow shaper shaping time are programmable. After the slow shaper, a capacitor, which is represented by SCA and PD in Fig. 1, is located. By disconnecting the capacitor from the slow shaper, a pulse height is store in the capacitor. SCA is controlled by an external signal, hold HG and hold LG. On the other hand, PD is controlled by the external signal or an internal signal generated by a discriminator. This feature provides automatic

pulse height recording. The stored DC voltage is multiplexed and transferred to an external analog-to-digital converter (ADC). There is another shaper having a shorter shaping time called fast shaper (FSB). The shaped signal is fed into two discriminators. One is for timing measurement. Discriminated logic signals are output in parallel. The other one provides a logic signal to control PD. There are two 10-bit DACs providing voltage thresholds for two discriminators. In order to adjust the voltage threshold channel-by-channel, additional 4-bit DAC is installed in each channel.

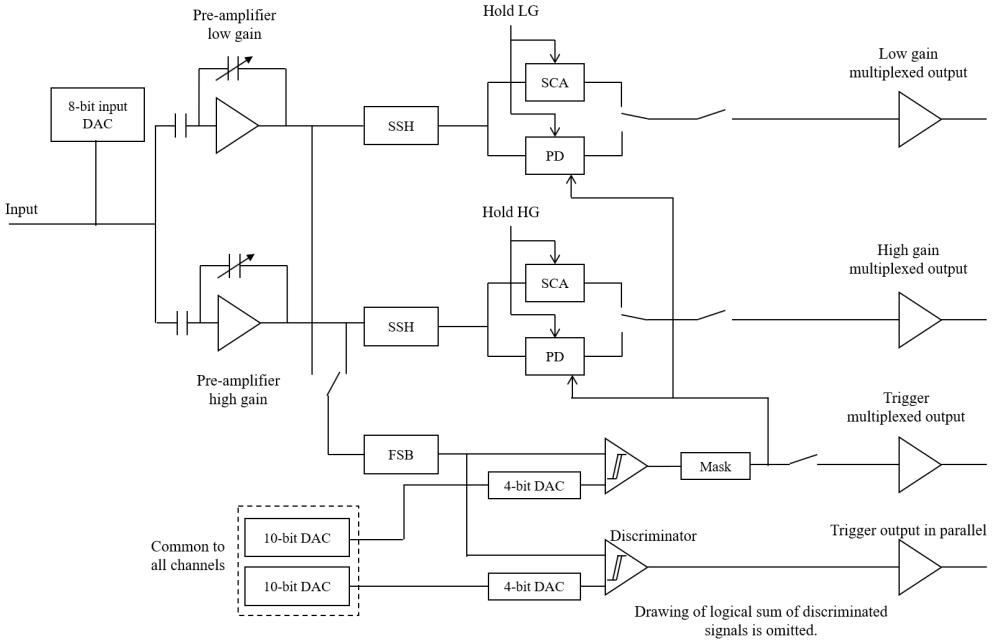

Fig.1. Block diagram of a channel in CITIROC1A. CITIROC1A has double gain structure with two pre-amplifiers. SSH is a slow shpaer for a charge measurement. SCA and PD are a capacitor to store a pulse height. Hold HG and LG are external signals to control switches before capacitors. FSB is a fast shaper for a timing measurement. Analog and logic signals are multiplexed and output except for a trigger output.

The feature of CITIROC is that this ASIC has charge measurement lines. By measuring the stored voltage in SCA or PD by an external ADC, we can obtain a clear photo peak spectrum. This allows us to adjust and monitor MPPC gain condition precisely.

PETIROC2A is an ASIC dedicated for the high-resolution timing measurement for TOF-PET. The block diagram is illustrated in Fig. 2. The number of input channel of PETIROC2A is also 32. This ASIC has a built-in termination resister before the 8-bit InputDAC. The pre-amplifier, which has wider bandwidth than that of CITIROC, is installed before the discriminator. The amplification factor is fixed, 40. Owing to this pre-amplifier, a faster signal rise time and a narrower amplified signal width are expected comparing to those from CITIROC. The discriminator voltage threshold is given by a common 10-bit DAC and 6-bit DAC channel-by-channel. Discriminated logic signals are output in parallel. The charge measurement line is branched before the pre-amplifier. Thus, we could not see a single photo-electron (p.e.) signal. In a TOF-PET application, 511 keV gamma rays are detected by inorganic scintillator. As PETIROC2A is dedicated to detect a 511 keV gamma ray, 1 p.e. measurement is not considered. In this

ASIC, although there are internal ADC and time-to-digital converter (TDC), they are not used in the E50 experiment.

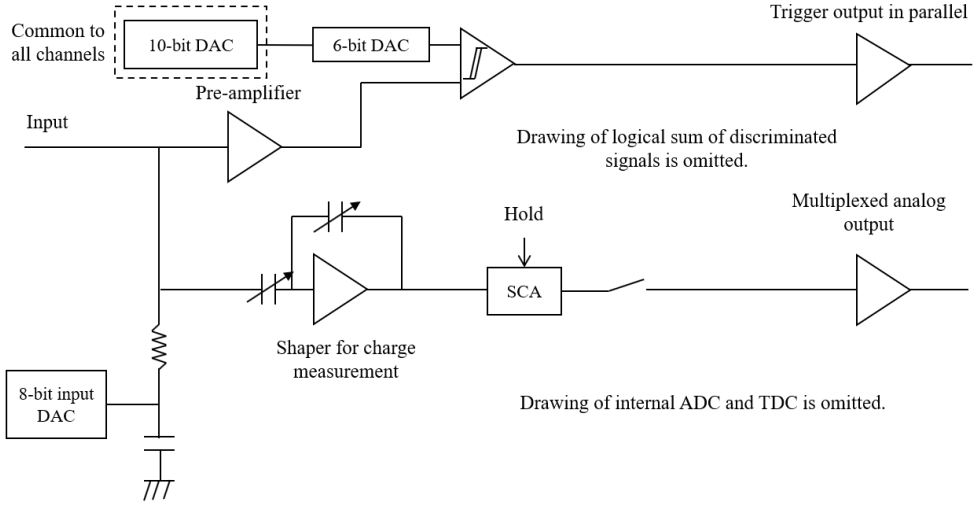

Fig.2. Block diagram of a channel in PETIROC2A. PETIROC2A has a internal termination register. The fixed gain pre-amplifier is located in the trigger line. The discriminator voltage threshold is given by a common 10-bit DAC and a 6-bit DAC channel-by-channel. The logic signals are output in parallel. A shaper is placed for the charge measurement. This shaper does not amplify a signal. The shaped signals are multiplexed and are output from an analog output port. Internal ADC and TDC are committed from the diagram.

§3. Front-end electronics

The picture of the developed FEE is shown in Fig. 3. FEE is comprised of an analog board, which has a CITIROC1A chip or a PETIROC2A chip, and a digital board, which has a field-programmable gate array (FPGA) , Xilinx Kintex-7 (XC7K-160T-1FBG676). The ASIC on the analog board is controlled by the FPGA. The FPGA receives the discriminated logic signals from the ASIC. An ADC (AD9220) is located on the digital board for the charge measurement; however, it did not work in this test experiment. The FPGA communicates with a personal computer (PC) with gigabit Ethernet through an optical fiber module, SFP. Since the FEE has two SFPs, the data transfer speed is up to 2 Gbps. The communication protocols, the user datagram protocol (UDP) or the transmission control protocol (TCP), are provided by silicon TCP (SiTCP) [8]. The digital board has an RJ45 connector to receive a clock signal in order to synchronize FEEs.

A special TDC for a trigger-less continuous timing measurement, streaming TDC, was developed in the previous test experiment at ELPH in 2018 [9]. The streaming TDC was implemented into the FPGA. The TDC timing precision was 0.97 ns. Thus, the FEE measures the timing of the leading and trailing edges of the logic signals from ASIC without a trigger signal and transmits leading edge timing and time-over-threshold (TOT) information for all the incoming signals to a PC.

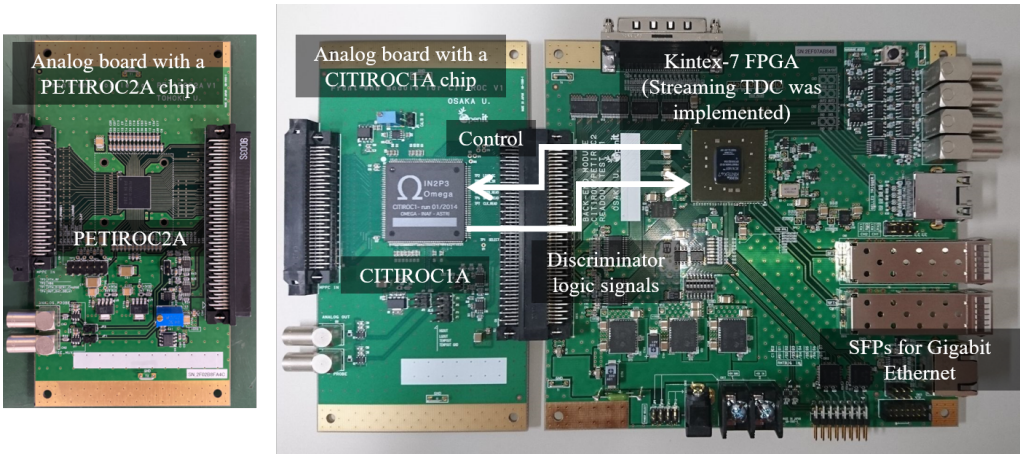

Fig.3. Photograph of an FEE. Two kinds of analog boards for CITIROC1A and PETIROC2A and a digital board. The ASIC is controlled by a FPGA and the discriminator logic signals are fed into the FPGA. FPGA communicates with a PC through two SFP modules.

§4. Experiment

4.1 Detectors

We used two types of scintillating fiber detectors. One is a prototype fiber tracker, which was tested in the previous work [4, 9]. The prototype fiber tracker comprises four sets of three scintillating fiber telescopes, which consists of a 1-mm diameter scintillating fiber, Kuraray SCSF-78M. In a set of telescopes, the fibers are arranged at tilt angles of 0° (X), +30° (U), and −30° (V) with respect to the vertical direction. The prototype fiber tracker has 128 fibers in total. An MPPC, Hamamatsu Photonics S13360-1350 is attached to the end surface of each fiber. The structure of the prototype fiber tracker is similar to that of the focal plane fiber tracker. In this report, we call this detector as the fiber detector A (FD-A).

The other fiber detector is a set of fiber telescopes that makes up the beam line fiber tracker for the E50 experiment. For simplicity, we call this detector as the fiber detector B (FD-B). Fig. 4 shows a photograph of the FD-B. The configuration of telescopes is the same that of FD-A; a set of telescopes has X, U, and V layers. A scintillation fiber, Kuraray SCSF-78M, is placed in a same manner; however, its diameter is 0.5 mm. A layer consisted of the fibers arranged in a staggered configuration as shown in Fig. 4. A layer has 512 fibers in total. Two horizontally adjacent fibers are combined to a readout channel. End surface of two fibers is connected to an MPPC, Hamamatsu Photonics S13361-1350AE-08, which will be released as an official product; this is an 8x8 array type MPPC package. The layer is divided to four readout unit, which contains 128 fibers, that is, 64 readout channels. The fibers in the unit are read by an S13361-1350AE-08.

There were four reference counters. Each reference counter consists of a plastic scintillator bar, Eljen Technology EJ-228, with a cross section of 6x6 mm^2 and a length of 150 mm. Scintillation lights are collected by a metal-package photomultiplier tube (PMT), Hamamatsu Photonics R9880U-113 attached to one end surface.

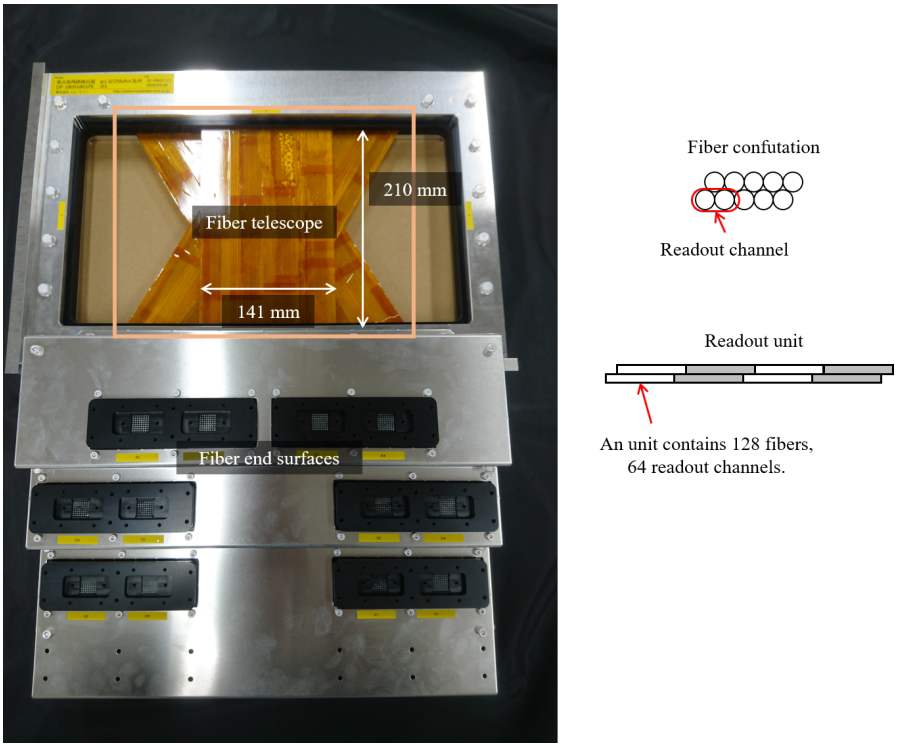

Fig.4. Photograph of FD-B. The X, U, and V layers are seen in the effective area. 12 MPPC arrays are attached to the fiber end surfaces. The fibers in a layer are arranged in a staggered configuration. Two circled fibers are combined as a readout channel. A layer is divided to four readout units.

4.2 Experimental setup

The reference counters, the FD-A, and FD-B were installed along a photon beam direction as shown in Fig. 5. We additionally installed a Chrenkov timing counter; however, this counter is not used in the analysis in this report. See details in Ref. [10]. The reference counter 1 and 2 were placed horizontally and perpendicular to the vertical axis, respectively. The reference counter 3 and 4 were tilted $\pm 30^\circ$ respect to the the vertical axis, respectively. The signals from the reference counters were discriminated by a NIM discriminator. The discriminated logic signals were sent to a hadron universal logic (HUL) module [11]. The streaming TDC [9] was implemented into a FPGA on HUL. FEEs and the HUL were synchronized by a 50 MHz master clock signal transmitted by a HUL.

We used three FEMs with a PETIROC2A chip and two FEMs with a CITIROC1A chip. The FEEs with a PETIROC2A were connected to first nine layers from the upstream of FD-A. 64 channels in a readout unit in the X layer of FD-B were read by the FEEs with a CITIROC1A. We started with this configuration and swapped two FEEs with a PETIROC2A and two FEEs with a CITIROC1A during the beam time to test all the combination between ASICs and fiber detectors. The streaming TDC data were transferred to a PC with two Intel Xeon E5-2630 v4 processors and 256 GB main memory through a network switch Fiberstore S3800-24F4S. The link speed was up-converted from gigabit Ethernet to 10 gigabit Ethernet by the switch. The data acquisition (DAQ) software dedicated for a trigger-less DAQ ran on the PC. About the DAQ software, see details in Ref [9].

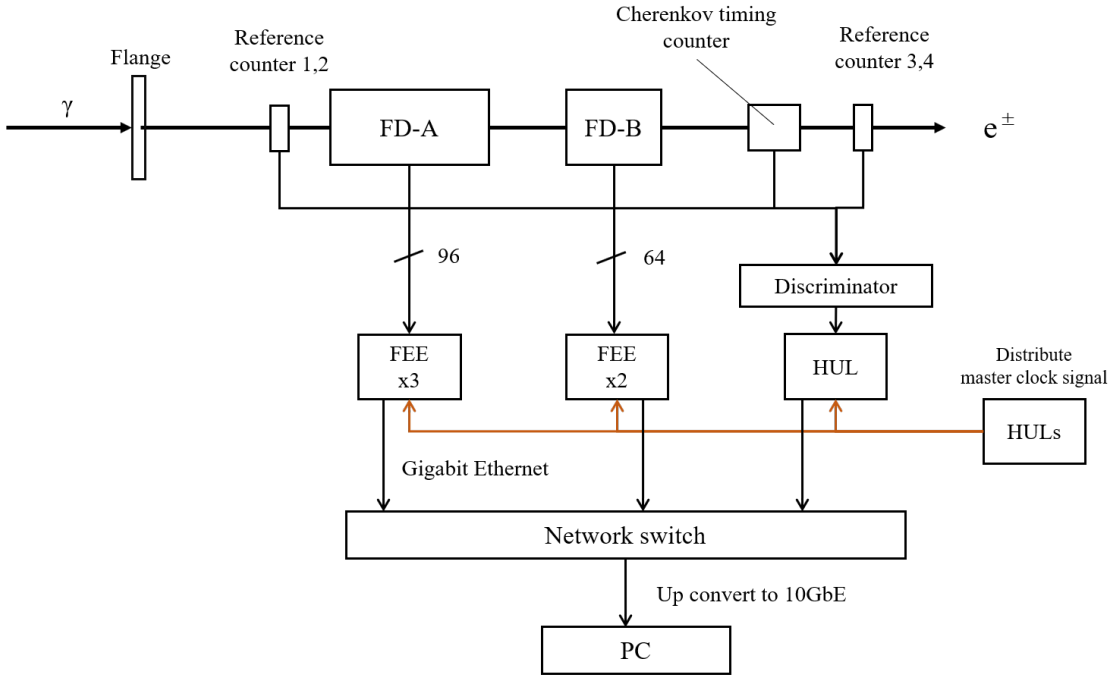

Fig.5. Experimental setup. The detectors are installed along the photon beam direction. 96 channels of FD-A are read by three FEEs and 64 channels in a readout unit are read by two FEEs. The discriminated logic signals of the reference counters and the Cherenkov timing counter are read by a HUL. The orange lines represent a 50 MHs master clock. FEEs and the HUL send streaming TDC data to a PC by gigabit Ethernet. The network speed is up-converted by a network switch.

4.3 Experimental condition

The detectors were irradiated with electrons and positrons converted from bremsstrahlung-photon beam. A spill duration was 10 s. Electrons and positrons momenta were not analyzed, and were distributed up to 1.3 GeV/c, which was an electron energy in the accelerator. We took data by gradually increasing the counting rate up to 1.1 MHz/mm detector segment corresponding to the 1.1 MHz input signal rate. The overvoltage (V_{OV}) condition for MPPCs were summarized in Table. 1. The definition of overvoltage is the difference between bias voltage applied to MPPC and breakdown voltage of MPPC. Two bias conditions were tested because the amount of signal width decrease of EASIROC depended on the overvoltage. In EASIROC, more signal width decrease was happened the higher overvoltage was applied. The higher overvoltage was applied to MPPCs reading FD-B to compensate smaller light yield due to smaller fiber diameter by increasing the photo detection efficiency of MPPC. The voltage threshold for the discriminators in CITIROC1A and PETIROC2A were set to 3.5 p.e. The amplification factor of pre-amplifier in CITIROC1A was 25 and 17 for FD-A and AD-B, respectively. As the trigger-less DAQ system was used, there was no hardware trigger. All received data were recorded in the PC without any filtering.

Table 1. Overvoltage setting for MPPCs.

Detector	V_{OV}-#1 (V)	V_{OV}-#2 (V)
FD-A	3.5	4.5
FD-B	4.5	5.5

§5. Analysis and results

5.1 Hit time interval

As we took data using the trigger-less DAQ system, we had a complete set of detector hit data in a spill. First, we divided a spill duration of 10 s to three time analysis frames (0-1.5 s, 1.5-6.5 s, 6.5-10 s) because the electrons and positions rate were gradually changed by a factor of 3 in a spill duration. Thus, a histogram for a hit time interval for each channel was obtained in each time frame; it provides a single rate if we assume that a detection efficiency is 100%. Fig. 6 (a) and (b) are the typical time interval histograms for a readout channel in FD-B under the 1.1 MHz/mm condition for CITIROC1A and PETIROC2A, respectively. Fig. 6 (c) is a unzoomed figure of Fig. 6 (b) in the vertical axis. The horizontal axis is a time interval from a previous hit in the TDC channel; A TDC channel is equal to 0.97 ns. The strong peak is seen in Fig.6 (c) around the 40 TDC channel. The amplified signal in PETIROC2A seems to be oscillated; this probably makes second logic signal. Even if we set higher voltage threshold, this strong peak does not disappear. One can find a wave structure in Fig. 6; this comes from a bunch structure of electrons in the accelerator. The solid line is a fitting function defined as,

$$\boldsymbol{A exp}(-\boldsymbol{\lambda t})(1+\boldsymbol{B sin}(\boldsymbol{\omega t}-\boldsymbol{\alpha})), \tag{1}$$

where A, B, λ, ω, and α are fitting parameters. λ is a rate, that is, a incoming charged particle rate at a fiber position. In this report, we simply call λ the rate.

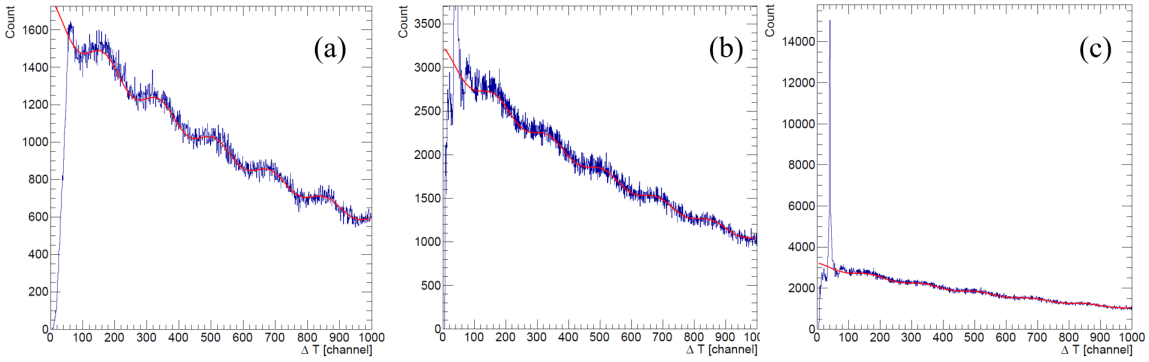

Fig.6. Hit time interval distribution for a fiber under the 1 MHz/mm condition with the overvoltage of 4.5 V. (a) Time interval distribution for CITIROC1A reading FD-B. (b) The same histogram for PETIROC2A. (c) Unzoomed histogram of (b).

One can find event losses around $x = 0$ due the signal pileup. By comparing Fig6 (a) and (b), the drop starts from smaller x in Fig.6 (b). It reflects the narrower signal width of PETIROC2A. However, data up to around 60 TDC channel cannot be used due the second pulse. From Fig. 6 (a), the loss ratio

is obtained from a ratio between the area of the fitting function and the area of the histogram. Thus, the loss ratio of 3.9% was obtained for CITIROC1A. This result is better than the loss ratio of 5% for EASIROC obtained in the previous work under the 1 MHz/mm condition [4]. In the test experiment, we set the smaller pre-amplifier gain of 17 than the gain of 75 for EASIROC in the previous work; it probably results the smaller loss ratio. By assuming that the dead time of CITIROC1A follows the paralyzable model, the dead time of 37 ns was obtained. This was also smaller than that of EASIROC. For Fig. 6 (b), although it is difficult to estimate the loss ratio due the second pulse, the loss ratio should be larger than that of CITIROC1A because the measurement is inefficient up to around 60 ns.

5.2 Time over threshold

Fig. 7 (a) and (b) show the measured time-over-threshold (TOT) distributions for CITIROC1A and CITIROC2A, respectively. Blue and red histograms are for a few kHz/mm condition and 1.1 MHz/mm condition, respectively. The horizontal axis is the TDC channel. In Fig. 7 (a), a peak around 30 TDC channel corresponds to the signals from electrons and positrons. Peaks around 10 TDC channel are probably dark noise. As the rate was low, dark noise was relatively enhanced. In Fig. 7 (b), a peak around 10 TDC channel corresponds to the signals from electrons and positrons. Signals from dark noise is not seen because the signal width is too narrow. The minimum measurable signal width of the streaming TDC is 7 ns, and signals with smaller TOT values are actually not detected.

Peak position of the red histogram is slightly shifted to the lower side. The peak position of the red histogram in Fig. 7 (a) was decreased to 97% of blue one. For Fig. 7 (b), we estimated the shift using the mean value of histogram because the distribution is not smooth. Thus, the mean value of the red histogram was 93% of blue one.

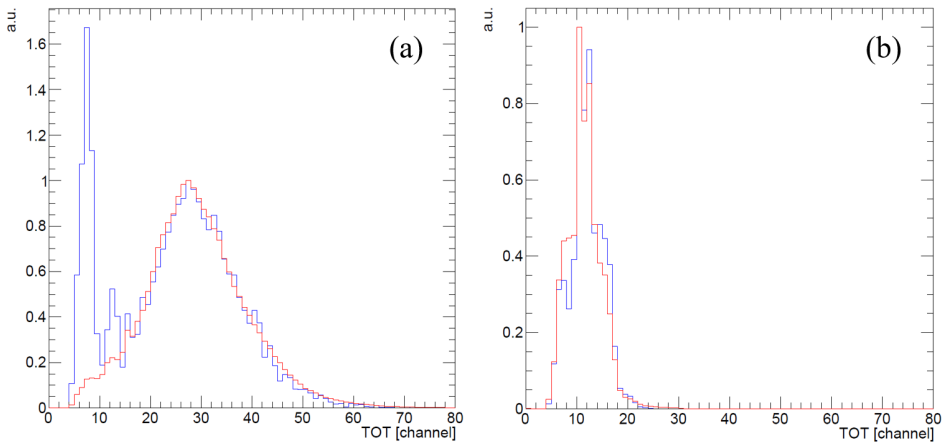

Fig.7. (a) TOT distribution for a fiber for CITIROC1A. (b) TOT distribution for a fiber for PETIROC2A. Blue and red histograms are for a few kHz/mm condition and 1.1 MHz/mm condition, respectively. The overvoltage setting was 4.5V.

§6. Discussion

The amplified signal width of PETIROC2A was expected to be narrower than that of CITIROC1A. Actually, the obtained hit time interval distributions imply that the signal width of PETIROC2A is narrower. However, double or more pulses are seen in PETIROC2A due to the oscillation of the pre-amplifier; it makes the measurement inefficient up to around 60 ns. The second pulse is critical from the view point of the trigger-less DAQ system. As all the hit data are transferred to PCs, the presence of a second pulse doubles amount of data. On the other hand, the loss ratio and the dead time of CITIROC1A at the 1.1 MHz/mm condition were 3.9% and 37 ns, respectively. The detection efficiency still does not reach to 97%; however, we found that the smaller pre-amplifier gain setting provides the smaller dead time. More gain settings should be investigated to minimize the dead time while keeping a timing resolution.

For CITIROC1A and PETIROC2A, the decreasing of the TOT were small if the rate was increased. As the decreasing of the TOT value in EASIROC was 30-40% at the 1 MHz/mm condition, better results were obtained. By considering these results, we decided to use a CITIROC1A chip as the readout ASIC for the scintillation fiber detectors in the E50 experiment.

§7. Summary

We conducted the test experiments at ELPH to investigate the high-rate capabilities of the CITIROC1A and PETIROC2A ASICs and determined the appropriate ASIC for scintillation fiber detector readout in the E50 experiment. These ASICs were tested under the high-rate condition up to 1.1 MHz/mm using the signals from the scintillating fiber detectors. The CITIROC1A chip showed the loss ratio of 3.9% and the dead time of 37 ns at 1.1 MHz/mm; these results better than those of EASIROC obtained in the previous work [4]. The amplified signal width in PETIROC2A seems to be narrower than that of CITIROC1A; however, the oscillation of the pre-amplifier makes a second discriminated logic pulse. The timing measurement is inefficient up to the hit time interval of around 60 ns due to the second pulse. Therefore, we decided to adopt CITIROC1A as the readout ASIC for the scintillating fiber detectors.

The analysis for FD-A are still on going. In addition, we should perform more detail analysis for the rate dependence of the TOT value and the timing resolution. Those result should be summarized in the future.

Acknowledgment

We would like to acknowledge the grate efforts of the ELPH members for the stable beam operation and the support for the test experiment. We would like to thank the technical support from the members of the Open Source Consortium of Instrumentation (Open-It).

References

[1] H. Noumi et al., KEK/J-PARC-PAC 2012-19 (J-PARC E50 Proposal) (2012) (available at: http://www.j-parc.jp/researcher/Hadron/en/pac_1301/pdf/P50_2012-19.pdf).

[2] K. H. Tanaka et al., Nucl. Phys. A 835, 81 (2010).

[3] S. H. Kim, A. Hosaka, H. C. Kim, H. Noumi, and K. Shirotori, Prog. Theor. Exp. Phys. 2014, 103D01 (2014).

[4] T. Aramaki et al., ELPH annual report 2018, Tohoku University, 44 (2019).

[5] S. Callier et al., Physics Procedia 37, 1569 (2012).

[6] J. Fleury et al., JINST 9, C01049 (2014).

[7] S. Ahmad et al, 2018 IEEE NSS/MIC, 1-4 (2019).

[8] T. Uchida, IEEE Trans. Nucl. Sci. 55, 1631 (2008).

[9] R. Honda et al, Prog. Theor. Exp. Phys. 2021, ptab128 (2021).

[10] T. Akaishi et al., ELPH annual report 2018, Tohoku University, 58 (2019).

[11] Hadron Universal Logic Module (available at: http://openit.kek.jp/project/HUL) [in Japanese].

(ELPH Experiment : #2937)

Development of Photon Tagging System at BM4 beam line

M. Kaneta[1], T. Akiyama[1,2], K. Fukada[3], H. Fujioka[3], T. Fujiwara[1], K. Itabashi[1,2], R. Kino[1], M. Mizuno[1], S. Nagano[1], S. Nagao[1], S. N. Nakamura[1], Y. R. Nakamura[1], K. Okuyama[1,2], K. Tachibana[1], Y. Toyama[1,2], K. Uehara[1,2], and H. Umetsu[1]

[1]*Department of Physics, Graduate School of Science, Tohoku University,*
[2]*Graduate Program on physics for the Universe, Tohoku University(GP-PU)*
[3]*School of Science, Tokyo Institute of Technology*

The NKS2 experiment is promoting the hadron photo-productions and hyper nuclear spectroscopy experiment at ELPH. The photon tagging system is the important part of the system to identify the photon production time and the energy. Because of problem of the tagger which was installed after the Great East Japan Earthquake, we started the development of the new tagger as the third generation. The project was a part of NKS2 performance optimization for the Λn final-state-interaction measurement in $\gamma + d \rightarrow \Lambda + K^+ + n$ reaction. We will report the design concept, constructions, and the performance of the 3rd generation tagger.

§1. Motivation

In the NKS2 experiment, a photon tagger identifies the photon beam generation time and the energy by measuring the energy and time of electrons that have lost energy due to bremsstrahlung. The photon tagging counters (a.k.a tagger) installed in the BM4 bending magnet. The locations of the NKS2 spectrometer and the tagger are shown in Fig. 1.

Until the Great East Japan Earthquake, we had been using a tagger (Ref. [2]), which consists of a plastic scintillator and a PMT connected by an optical fiber. It is called the first-generation tagger.

The plastic scintillator consisted of two layers, a narrow one called the finger (to determine the energy of the scattered electrons) and a wider one called the backup (to determine the time), and the counters were named TagF and TagB. The combination of TagF and TagB hits was used to generate a trigger signal from scattered electrons which lost the energy by bremsstrahlung.

Due to the damage caused by the earthquake, we developed a new second generation tagger (Ref. [3]) with a Silicon Photo-Multiplier (SiPM, Geiger Mode APD device) directly connected to a plastic scintillator. SiPMs not only have the advantage of being small and operating in a magnetic field, but they also have the advantage of being less expensive than PMTs (e.g., comparing with fine-mesh dynode PMTs) that operate in a magnetic field. The SiPMs used in the second-generation tagger were MPPC S10931-100P from Hamamatsu Photonics (for TagF) and MPPC array S11828-3344MC(X1) (for TagB). The plastic scintillator was EJ-204 (equivalent to Saint-Gobain BC-404) from ELGEN system.

Semiconductor sensors are more vulnerable to radiation damage than PMTs. In the stage of at the development, we estimated that they would last 10 years with the same ring operation as before. The second-generation tagger was installed in 2016 and has been used for experiments. Figure 2 is a photo of the second-generation Tagger.

During the beamtime in the first semester of 2019, it was found that waveforms of some TagBs were wrong, and some had no signal. After that, we measured the dose around the BM4 bending magnet during the period when the ring was in operation with a γ/neutron dosimeter and found that the dose

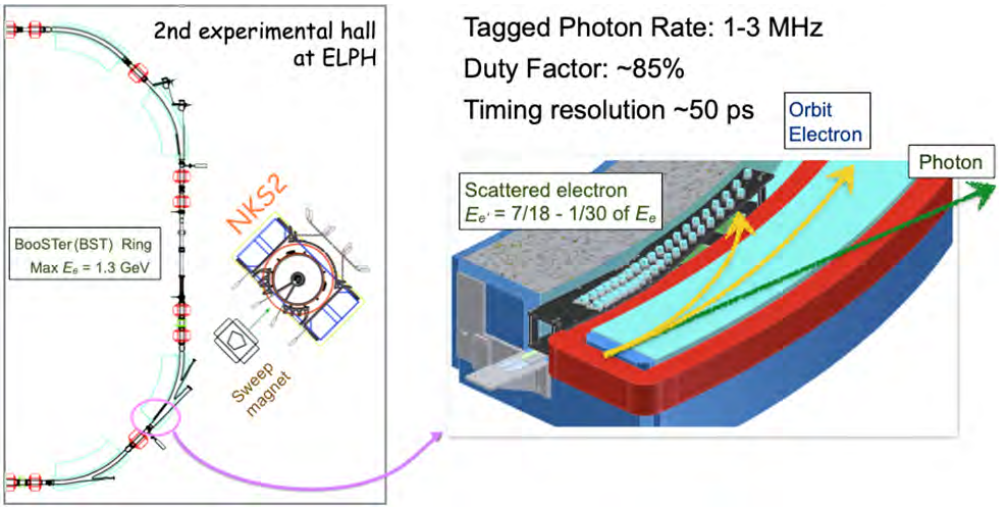

Fig.1. The location of the tagger and the NKS2 spectrometer in the second experimental hall are shown on the left. The right figure shows the position of the tagger placed in the bending magnet.

Fig.2. Photo of the second-generation tagger. The TagF/TagB units are lined up on top of the frame.

was about 10 times higher than expected.

In addition, the orbits of electrons assumed when finalizing the scintillator alignment in the second-generation tagger did not match the orbits of the electrons in the BST rings. This led to the problem that the tagger did not capture all the correct scattered electrons. The phenomena was confirmed by a simulation study as shown in Fig. 3.

In the tagger, four TagFs and one TagB were connected to MPPCs soldered to the same printed circuit board, and the unit was designed to be rearranged to accommodate the correct orbit of scattered electrons. However, it turned out that rearranging the units to match the current conditions of the ring's orbiting electrons was not possible due to its size in some locations. Furthermore, the close distance between TagF and TagB meant that background electrons which we want to reject were being generated as triggers. The backgrounds are the electrons scattered by the walls of the vacuum chamber and internal columns.

Therefore, it was necessary to develop the third-generation tagger that was completely redesigned, including the size and placement of the scintillator and the connection method of the MPPC.

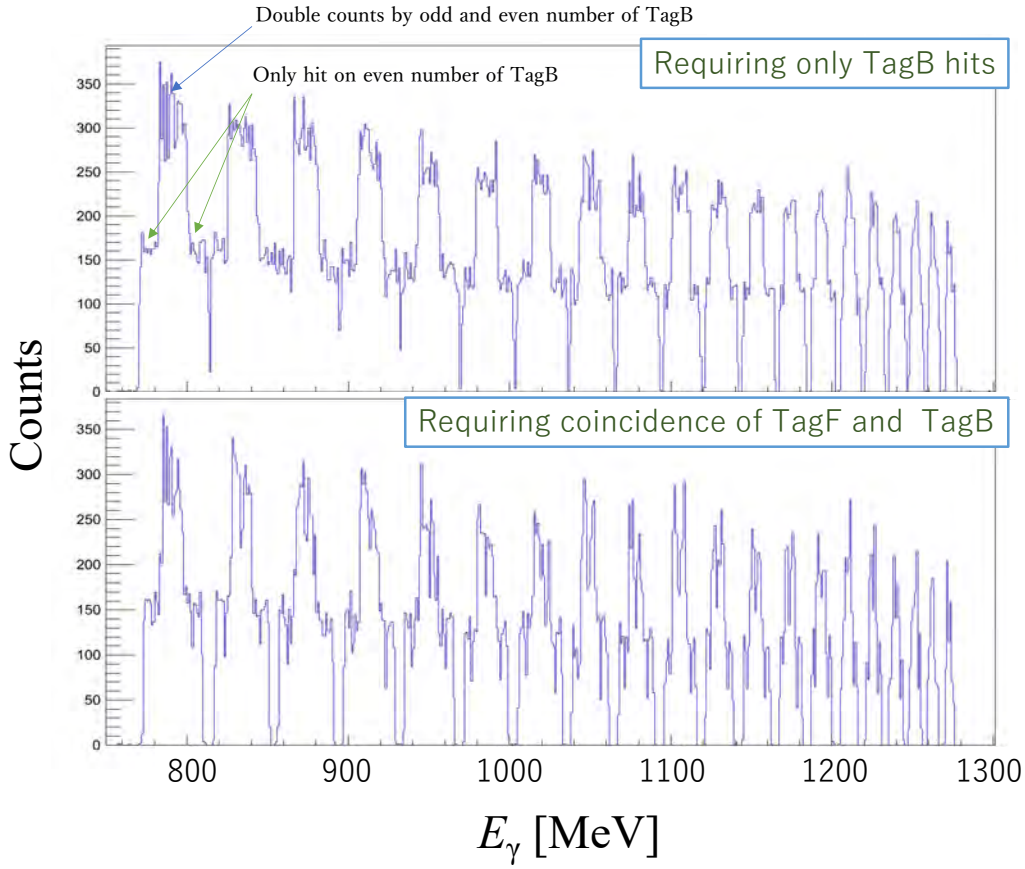

Fig.3. Simulation results of Hit distribution as a function of γ-ray energy without (top side figure) and with (bottom side figure) coincidence of TagF and TagB. The OR of the hit signal of TagB was taken during the data taking, which corresponds to the top side figure. The gaps in the distribution mean that there are some γ-ray energy regions that were not measured.

§2. Design

We started the development of our new tagger in late 2019. The MPPC used is a recent one, if possible, but the amplifier circuit for TagB uses basically the same design, and the type of plastic scintillator is not changed to reduce the development elements.

The concept of the design is as follows.

- Ensure that 5 MeV is covered for the energy of the scattered electrons.
  - In the second-generation tagger, all the widths were made the same, which resulted in an energy coverage of about 1 to 6 MeV.
  - Considering the resolution of the drift chamber, the measurement width of 1 MeV for γ ray was too fine and over specification.
- The TagF should be made in two layers and placed so that the center of the second layer of scintillators is at the overlap of the first layer of scintillators to avoid counting off due to the border.
- The scintillator is fixed to the enclosure, and the printed circuit board (PCB) with the MPPC is connected to the top and bottom of the frame.
  - If the MPPC is damaged due to radiation damage, etc., be prepared to replace easily the PCB.
- Increase the division of the frame so that the tagger can be removed without moving BM4.
  - The second generation was split into two parts, but in order to remove it, BM4 had to be moved, which took a lot of time and effort.
  - By making it easy to move out, we can eliminate radiation damage to the tagger except for our own beamtime.

The scintillator placement was optimized using GEANT4 based simulation. Figure 4 shows an example of the arrangement. The frame needs to be divided into several parts. Therefore, it became necessary to separate the scintillators from each other.

First, we made several layout plans to arrange them uniformly. Depending on where the actual enclosure would be divided, we combined the layout plans to determine where to place the individual scintillators.

Note that we had compared the hit patterns of the second-generation tagger with experimental data and simulations, because it was necessary to check for inconsistencies in the geometry and magnetic field maps used in the simulations.

The number of divisions of the frame parts was set to 3. Figure 5 shows the 3D CAD assembly drawing. The scintillator is fixed in the holes drilled in the top and bottom plates. The top panel has square holes for the MPPC and screw holes for mounting the printed circuit board (called MPPC unit). The shape of the MPPC unit is circular to make it easier to consider the interference between units. The MPPC units of TagF and TagB are shown in Fig. 6

The light shielding is done by attaching aluminum tape to the side of each of the frame, and by inserting an O-ring between the MPPC unit and the frame. That method eliminates the need to peel and re-gluing the light shielding when replacing the MPPC unit, as was the case with the second-generation tagger.

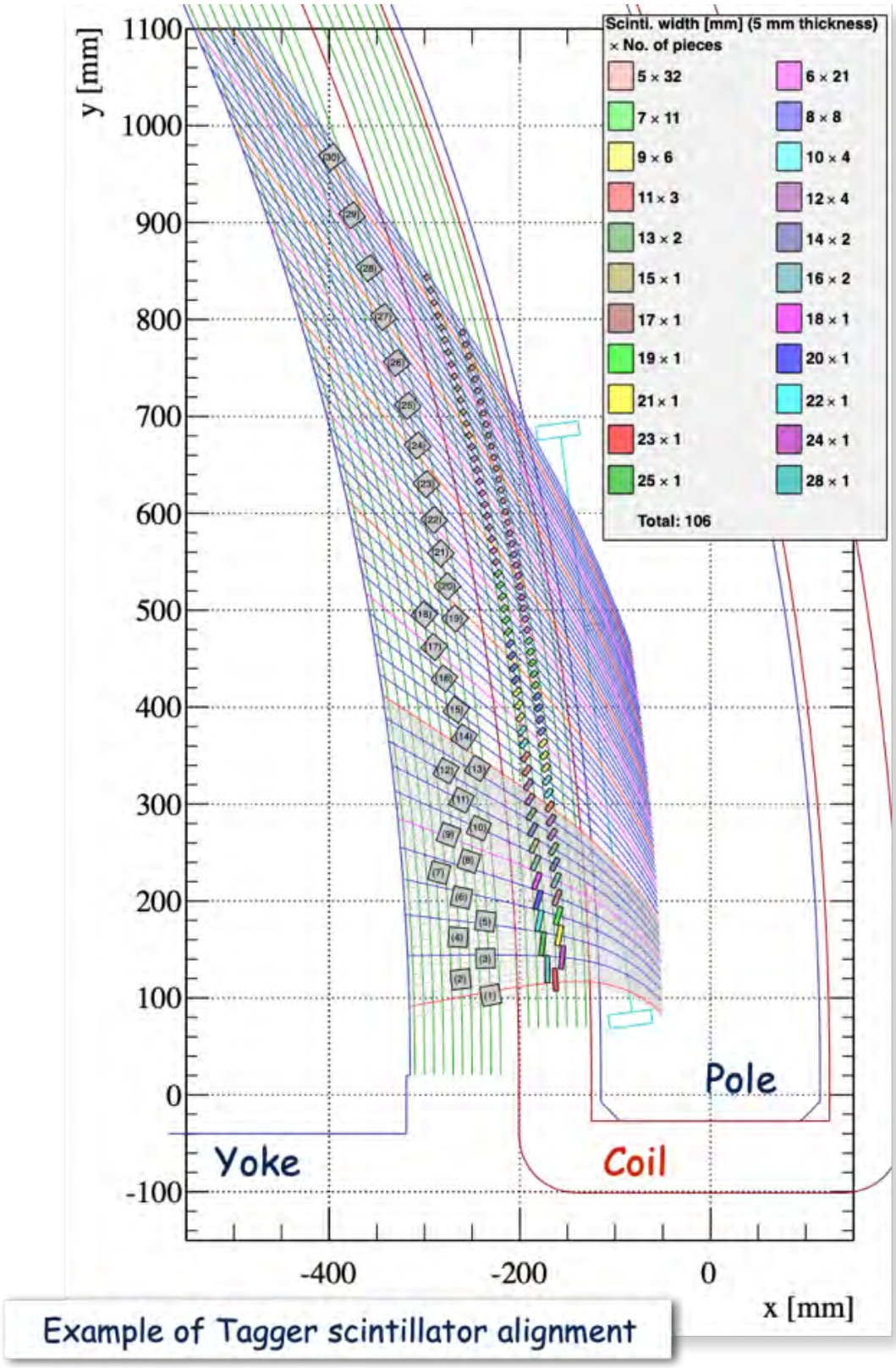

Fig.4. Example of electron trajectory and TagF/TagB placement plan by the simulation. An automatic placement algorithm is programmed with input parameters that are the distance from the center of the radius of curvature of the dipole magnet, the distance between the scintillators, and the overlap margin of the scintillators.

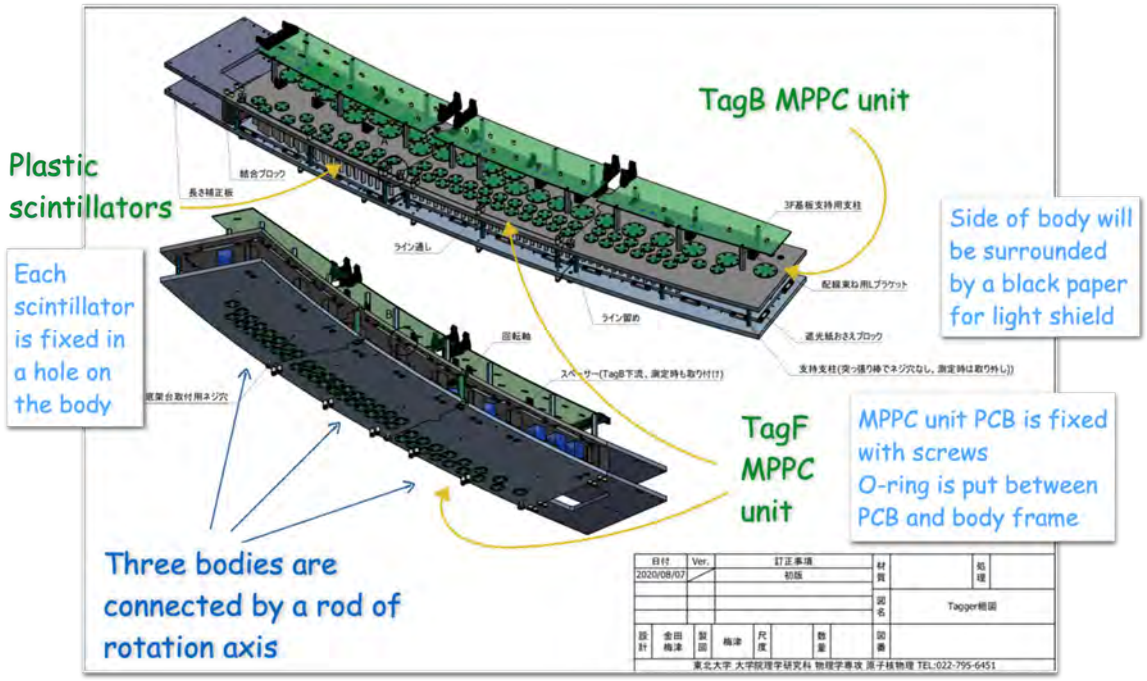

Fig.5. Assembly drawing of the tagger frame. The design was done using three-dimensional CAD.

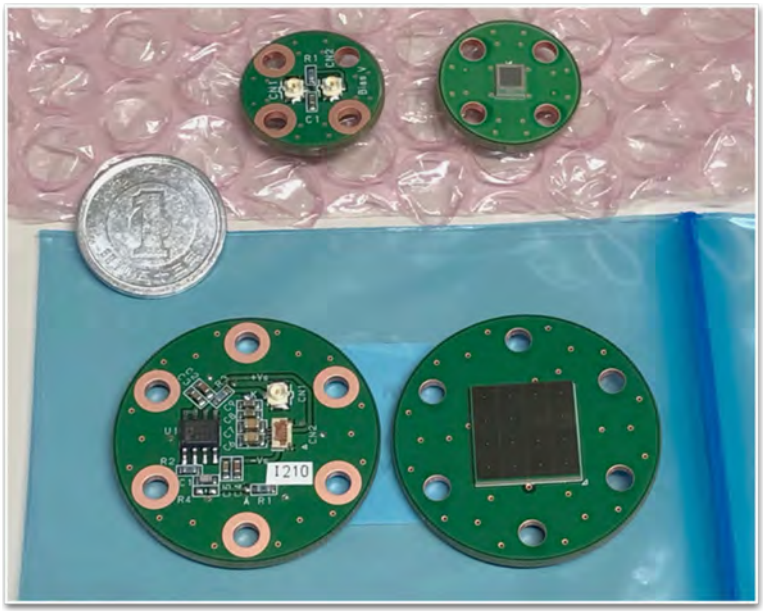

Fig.6. Photo of the MPPC unit. The upper side photo is the TagF-MPPC unit, which is mounted resistor, capacitor, and surface mount coaxial connector on the opposite side of the MPPC. The bottom side photo is the TagB-MPPC unit. The 4×4 array type MPPC is selected to detect photon from 20×20 mm^2 scintilator. On the other side, there are surface-mount coaxial connectors for the amplifier circuit and signal readout, and flexible flat cable connectors for the power supply of the amplifier and the bias voltage of the MPPC. A one-yen coin (20 mm diameter) is placed for size comparison.

In the third-generation tagger, MPPC S14160-3015PS was used for TagF and MPPC array S13361-3050NE-04 was used for TagB. Since the time resolution is important for TagB, we have evaluated the performance of the combination of the scintillator alone and the amplifier circuit for TagB using cosmic rays. before finalizing the frame design. We confirmed that the time resolution is less than 90 ps as σ. In addition, we are measuring the time resolution and detection efficiency using positron beams in the GeV γ irradiation hall in March 2020. The results show that the timing resolution is the same with cosmic-ray test and more than 99% detection efficiency.

§3. Assembling

The tagger is installed in the yoke of the BM4, therefore non-magnetic materials were used. ABS plastic is used for the frame, which is the main material.

After assembling the frame alone, we checked if it is possible to install/uninstall the tagger without moving the BM4 magnet. It turned out that there was no problem moving it in and out, but if you get too close to the screws that hold the vacuum chamber near the BM4 entrance, the light shielding window on the side may have damage. Therefore, a protective board was installed to prevent the screws from encountering the tagger during installing and uninstalling.

We will describe the assembly procedure in the following. The surface of the TagF scintillator is coated with a diffuse reflective material (EJ-520: a bright white paint consisting of titanium dioxide pigment). For the TagB scintillator, 100-μm thick aluminized mylar was used as the reflective material.

To fix the scintillators to the frame, the scintillators were placed in square holes and then glued with white silicone resin (RTV rubber). After all the scintillators were fixed to the upper and lower plates, those plates were fixed with columns. The screws used for fixing were also made of plastic.

After the MPPC units were installed, signal lines for TagF/TagB and bias voltage lines for TagF are wired by the connector on the front-end side and the MPPC units with a coaxial cable (1.13 mm diameter). The TagB MPPC unit's amplifier power supply and bias voltage to the MPPC are supplied via a printed circuit board attached to the top of the frame. A flexible flat cable is connected between this voltage supply board and the MPPC unit. The photo of the tagger assembled is shown in Fig. 7.

At the entrance of the BM4 magnet, there is a distribution board with bias voltage, amplifier power supply, and connectors for signal readout. Figure 8 shows the part of tagger at the entrance of BM4.

The TagF bias voltage is common to all TagF MPPC units and is distributed to each MPPC unit from the board. The TagF signal is distributed from coaxial cable to MIL connector and then connected to the readout circuit, NIM-EASIROC.

The TagB bias voltage is passed through a voltage distribution box (using the transistors produced in development of the second-generation tagger) and then connected to a multi-conductor cable with MIL connectors. This voltage distribution box allows for fine adjustment of the voltage for each channel. The TagB signals are connected from the amplifier output from each channel to the discriminator by a coaxial cable (RG-174/U) with LEMO connectors.

Fig.7. A picture of the tagger assembled. The tagger is placed in a frame made of aluminum to prevent it from tipping over. The upper side in photo related to a part which goes into the back of the dipole magnet. The other edge will locate the entrance side of the magnet. Note that the power supply PCB is not mounted in the picture.

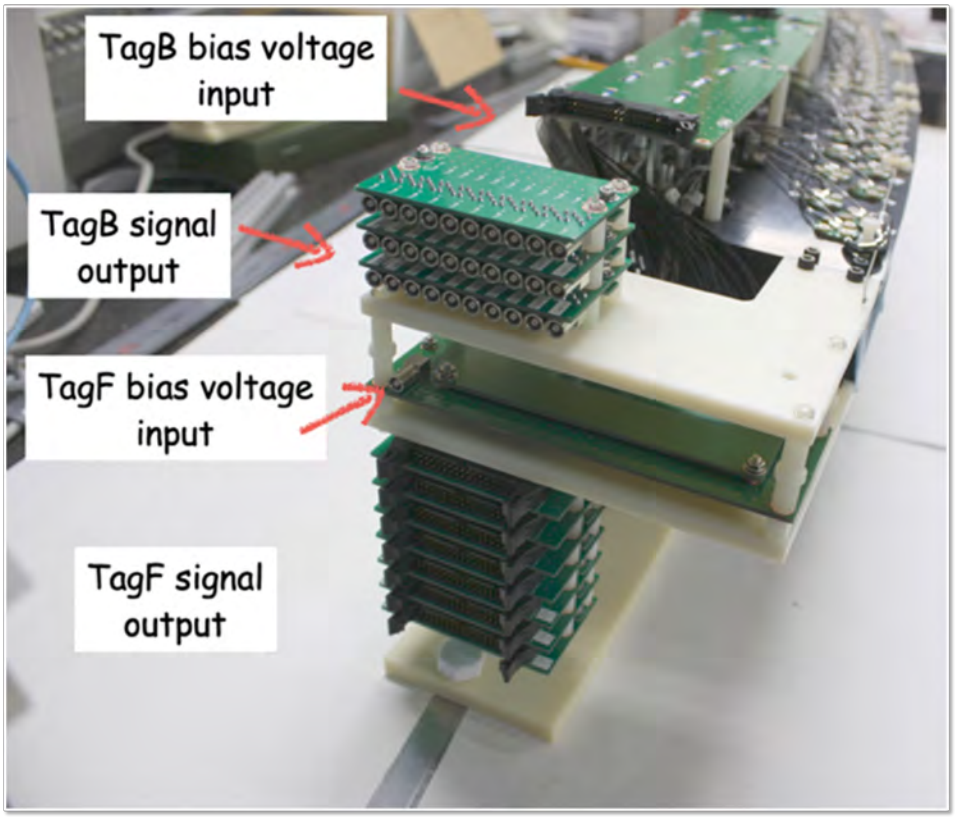

Fig.8. A picture of front-end of the tagger. The connectors for the signal readout and voltage supply of TagF and TagB are seen.

§4. Performance

The construction of the tagger was completed in May 2021. After checking the signal by cosmic-rays and ^{90}Sr/^{90}Y β source, we did performance tests at the 2nd experimental hall. At the beginning of June 2021, the tagger was installed in BM4, and the data acquisition system was tested by a set-up of the tagger and plastic scintillator hodoscopes placed downstream of the photon beamline as a reference counter.

In July 2021, the whole NKS2 trigger is also being tested in a real data acquisition environment. For physical data acquisition, we combined the tagger trigger signal with the multiplicity triggers of the Inner and Outer Hodoscopes of NKS2 for data collection.

The original plan was to use a trigger circuit with an FPGA module that would select the combination of TagF and TagB hits online. However, the LVDS FAN IN/OUT module to split the signals was not available in time, so we used the OR of TagB hits as the trigger signal from the tagger.

We confirmed a performance of beam bunch separation by Time-of-flight (TOF) distribution of TagB and Inner Hodoscope (IH). We choose one IH (called IHR2) which is close to γ beam line and is less fluctuation of flight path depend on momentum.

Figure 9 show an example of TOF distribution of which time difference is between TagB No. 30 (related to higher edge of electron energy) and IHR2. We can see the main peak and periodical peaks of 2 ns span. The main peak corresponds to true event that the gamma reacts at the target and we want

to use for physics analysis. The other peaks are accidental coincidence and the structure is reflected to the beam bunch structure. In the figure, the time-walk correction is not applied, but it shows the performance to separate the bunch.

Due to the conversion by material, the tagged photons are not always reach the target. To obtained cross-sections of reactions, the photon transmittance need to be determined.

We used a Lead glass calorimeter to detect the photon at the downstream of NKS2. The ratio of number of photon and valid hits on the tagger will be used the photon transmittance. The calculation method and its detailed description can be found in Ref. [5].

The photon transmittance is shown in Fig. 10. The horizontal axis is the segment number of TagF, where the smaller number corresponds to the lower energy of scattered electrons.

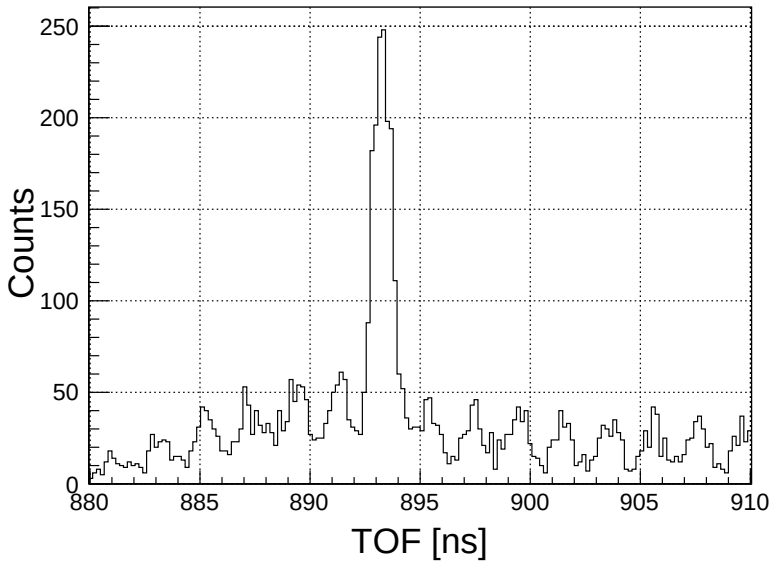

Fig.9. TOF distribution computed the time difference between TagB No. 30 and IHR2. Time-walk correction is not applied.

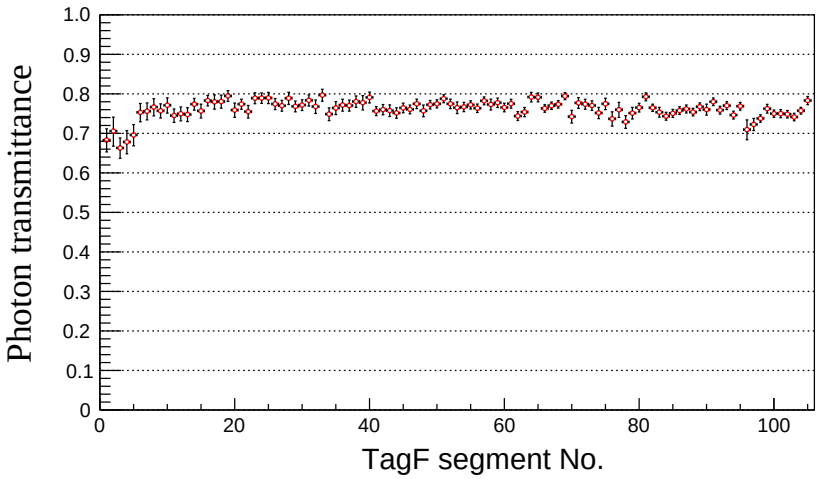

Fig.10. Photon transmittance as a function of TagF segment number is shown. Smaller (larger) segment number correspond to lower (higher) electron energy.

In the data collection, the OR of TagB hits was used as a trigger. To remove the background, the following conditions were required. There must be hits on two layers of TagF in consecutive segment numbers, and TOF of TagF and TagB must be in a certain time window. The results shows that the photon transmittance is about 70% to 80%. Those value are comparable to them obtained by the previous taggers.

§5. Trigger System

In order to construct an optimal trigger using the tagger, we need to select the appropriate combination of TagF and TagB online. For that purpose, we will construct a trigger logic using FPGA modules. The FPGA module we selected is the Hadron Universal Logic module (HUL), which was developed for the J-PARC Hadron Hall experiments. The circuit plan is shown in Fig. 11

Since the logic signal from the detector needs to be sent to the scaler in addition to the line to the HUL, an LVDS Fan In/Fan Out module is required. A prototype of the Fan In/Out module is currently being tested. After mass production of the module, we plan to test the trigger system using the beam.

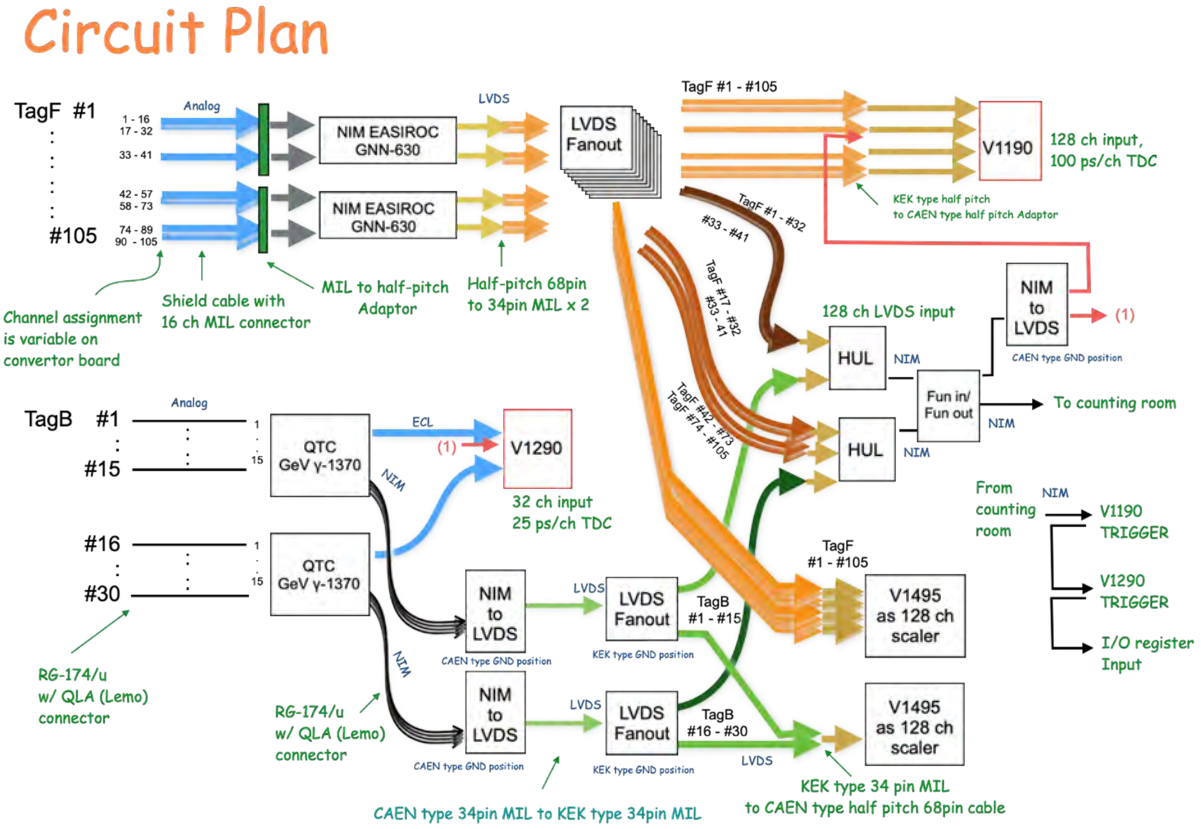

Fig.11. The trigger circuit plan of the tagger are illustrated. We will use a FPGA module, the Hadron Universal Logic (HUL) module for the trigger decision selected combinations of TagF and TagB hits.

§6. Summary

In the NKS2 experiment, hadron production and hyper-nuclear spectroscopy experiments using photon beams are in progress. The photon tagging system is important to identify the production time and energy of γ rays. We have developed a new tagger because the previous tagger was found to be defective. The tagger is designed to be easily removed outside in the other beamtime when we are not using to reduce radiation damage to the tagger. The structure of the tagger is such that it can be easily replaced even if the semiconductor, which is a component of the tagger, is damaged by radiation. We installed the tagger in the NKS2 system and evaluated its performance using the photon beam. We were able to observe the bunch structure of the accelerator beam and show that the accidental background can be removed. We also measured the photon transmission coefficient and obtained the same value as before.

Acknowledgment

We would like to thank the accelerator group for their contribution to the operation of the accelerator. In addition, we thank the ELPH staff for their support of our experiments.

References

[1] M. Kaneta *et al.*: Nucl. Instrum. Meth. **A866** (2018) 88-103.
[2] H. Yamazaki *et al.*: Nucl. Instrum. Meth. **A536** (2005) 70-78.
[3] T. Nishizawa *et al.*: IEEE Trans. Nucl. Sci. **61** (2014) 1278-1283.
[4] T. Ishikawa *et al.*: Nucl. Instrum. Meth. **A875** (2017) 193-200.
[5] T. Ishikawa *et al.*: Nucl. Instrum. Meth. **622** (2010) 1-10.

(ELPH Experiment : #2937)

Development of an Aerogel Cherenkov Counter with an MCP-PMT for e/π Separation

K. Tachibana[1], T. Akiyama[1,2], K. Fukada[3], H. Fujioka[3], T. Fujiwara[1], K. Itabashi[1,2], M. Kaneta[1], R. Kino[1], M. Mizuno[1], S. Nagano[1], S. Nagao[1], S. N. Nakamura[1], Y. R. Nakamura[1], K. Okuyama[1,2], Y. Toyama[1,2], and K. Uehara[1,2]

[1]*Graduate School of Science, Tohoku University,*
[2]*Graduate Program on physics for the Universe, Tohoku University(GP-PU)*
[3]*School of Science, Tokyo Institute of Technology*

We are developing an aerogel Cherenkov counter with MCP-PMT as an electron/positron veto counter in the NKS2 experiment. In the feature physics program, we will use higher photon beam rate (several times than before). Higher rate of electron and positron background due to pair production make an efficiency of data acquisition lower. Therefore, it is necessary to remove electrons and positrons at the trigger level. In the development, we evaluated the performance of the prototype detector and found that the detector makes the trigger rate lower in the feature physics program.

§1. Introduction

We are planning a Λn interaction measurement via Final State Interaction (FSI) in $\gamma + d \to K^+ + \Lambda + n$ reaction using real photon beam with NKS2 spectromenter [1] at ELPH. We will use a higher beam rate (Tagged photon rate: up to 5 MHz) than that of previous experiments which measure the strangeness photoproduction cross section. The current NKS2 trigger requires multiplicity of hodoscopes and photon tagger timing, and there is no electron veto counter to reject charged particles on the beam plane because of avoiding kinematic bias in data. That's why, we have been taking data all of charged particles including the electron/positron background. There is concerned about the deterioration of data acquisition (DAQ) efficiency due to the generation of a large amount of electron/positron background from high intensity real photon beams. Therefore, it is necessary to increase the DAQ efficiency by removing electrons and positrons at the trigger level in the higher beam rate. It is expected that the DAQ efficiency is about 70% with the trigger rate of 2 kHz and increases up to 90% with 1 kHz.

The requirements of the detector are: 1) small enough to fit into the limited space of an existing detectors (less than 40 mm thickness), 2) stable operation in 0.42 T magnetic field and 3) performance to withstand the expected electrons and positrons rates. In order to satisfy the requirements, aerogel of refraction index 1.01 was selected as the cherenkov radiator, and microchannel plate photomultiplier tubes(MCP-PMT) was chosen as photon detectors.

The maximum momentum of pions produced in the $\gamma + d$ reaction is about 1 GeV/c, and the maxi-

mum momentum of electrons and positrons is 1.3 GeV/c. To separate electron/positron from pion in the momentum range, we selected aerogel with a refractive index of 1.01 as the cherenkov radiator.

In the early stages of development, tests with fine-mesh dynode type PMT (HAMAMATSU H6152-01B) and SiPMs (HAMAMATSU MPPC S13360 series) are also being conducted. The test using the fine mesh dynode type PMT shows that we could not recognize one photon peak due to the gain. In the development of the detector with SiPMs, we had difficulty in removing the noise. Finally, we selected the microchannel plate photomultiplier tube (MCP-PMT, HAMAMATSU R10754-07-M16) as the photon sensor. The MCP-PMT we choose is developed for the TOP counter at the KEK Belle II experiment, and has been used in the experiment [2].

The MCP-PMT has 4×4 anode pads (5.28 mm square and 0.3 mm spacing) and the signal can be read independently. The effective area of photocathode is 23×23 mm^2. There are two stages of microchannel plate for amplification. Typical high voltage between photocathode to anodes is 2000 to 3600 V in order to satisfy the specification of MCP gain.

§2. The set-up of the experiment

The feasibility study was done in the second experiment hall at ELPH in July, 2021. The counters located at the downstream of the NKS2 spectrometer.

Figure 1 shows the schematic view of our set up. The aerogel was placed in a dark box and the MCP-PMT was placed on the bottom. The sides of the aerogel were wrapped with a Teflon sheet (0.1 mm) as a diffuse reflector.

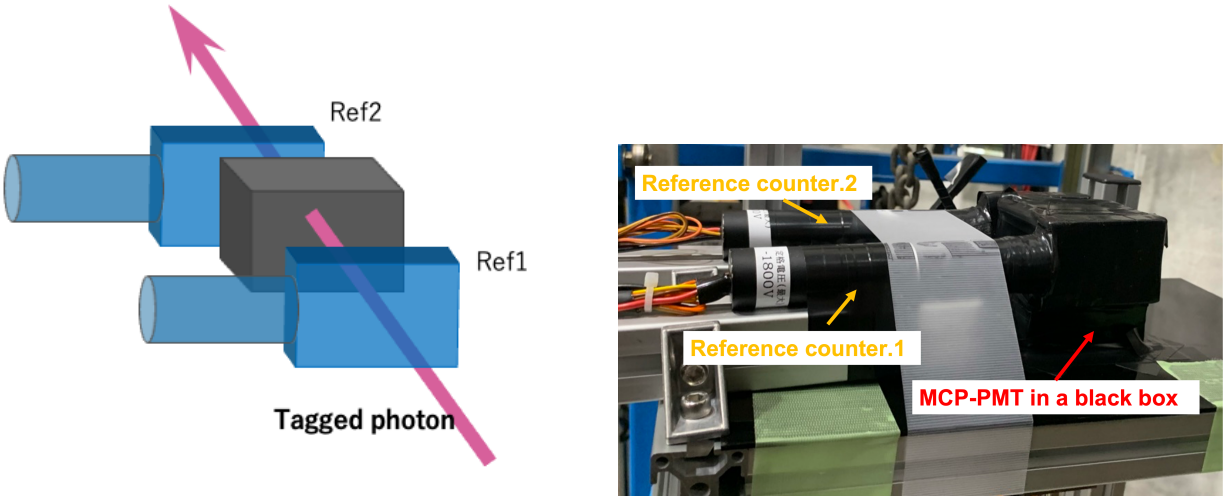

Fig.1. Left figure shows the schematic view of the counters setup and right figure is the photo of the setup. The photon beam passes from the lower right to the upper left in the figure. Two reference counters are placed in front of and behind the aerogel counter. The reference counter consists of a 12-mm thick plastic scintillator and a PMT (HAMAMATSU H6612). The upstream reference counter is an active target for photon conversion. One MCP-PMT is set on the bottom side of the aerogel counter.

The DAQ system was independent from the NKS2, but the tagged photon trigger signal was provided from the NKS2 DAQ system. The trigger signal for the test was the coincidence of hits of two reference counters and tagged photon.

The upstream reference counter was an active target of 12-mm thickness of plastic scintilltor. The radiation length is about 10 times of the NKS2 liquid deuterium target (30-mm tickness). The typical tagged photon rate was about 1 MHz in the beam time. The electron/positron rate by the reference counter corresponding to 10 MHz of tagged photon rate on the liquid deuterium target. Therefore, the e^-/e^+ rate in the aerogel counter was about twice of the rate we planned in the Λn FSI experiment.

We used a discriminator with charge-to-time convertor (called QTC) which was developed at ELPH [3]. QTC had a role of amplifier for short time and small signal from MCP-PMT.

The hit timing was recorded by CAEN V1290 multi-event/multi-hit TDC. The TDC has 25 ps timing resolution (LSB) and full-scale rage of 52 μs.

Note that we will use four MPC-PMTs for the actual detector. To avoid direct hit of photon beam, two MCP-PMTs will stay top and bottom, respectively. In the test, we will obtain one fourth of number of photoelectron with respected to the actual detector.

The average number of photoelectrons in the setup is expected to be 2.5. To estimate the value, we computed the number of Cherenkov photon in a region of wavelength (160$-$850 nm) with considering the quantum efficiency of the photocathode and the fraction of the aerogel end-face covered by the one MCP-PMT. We need to take into account the reflectivity on the reflector and the transmittance in the aerogel for the more realistic estimation, however, we assumed that those value are 100%.

It is difficult to count number of photoelectron from the pulse height (or charge) from one anode pad. Considering the multi-hit effect on one pad, the average number of photoelectrons reduced from 2.5 to 2.1.

§3. Analysis

As the first step, we select the MCP-PMT hits with selecting the timing to be close to reference counters. The number of hit channels of MCP-PMT are shown in Figure 2. We can see the tail of higher number of hit in the distribution. It is expected that the probability in region with more than 7 hits is less than 1%. The tail is not come from photoelectrons.

Since the MCP-PMT has almost no thermal noise, it is thought that tail component come from due to crosstalk. The typical photoelectron signal and crosstalk is shown in Fig. 3. The signals are from 4 pads that are located on the line of an edge of pad array.

The Time-of-flight (TOF) distribution of one channel of MCP-PMT and reference counter 1 is shown in Fig. 4. The black histogram are from the events where there are valid hit of reference counter 1 and 2, and the value of TOF is in the expected range.

The cross talk signal is delayed from photoelectron signal as seen in Fig. 3. It is the reason why we see the two peaks in the TOF distribution. We chose the earliest hit among 16 channels of MCP-PMT in each event as the candidate of photoelectron signal.

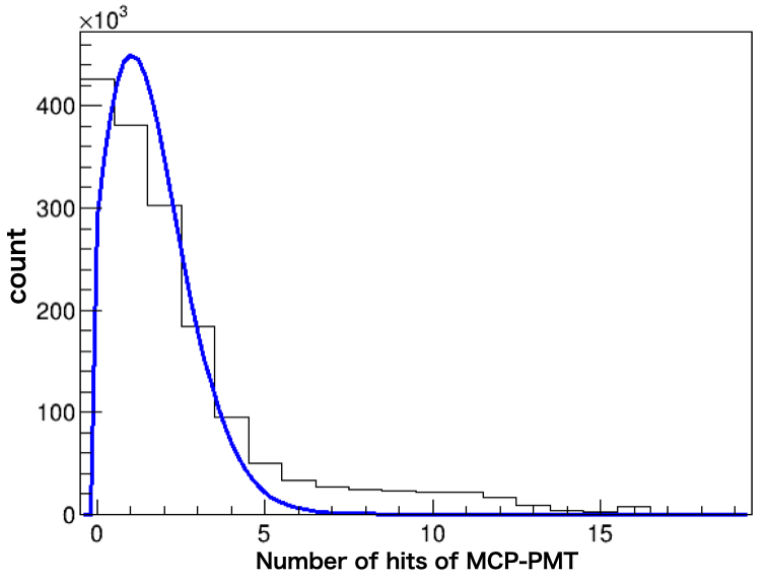

Fig.2. The number of hit channel distribution is shown. The curve is the result of fit by Poisson distribution. The average of Poisson distribution is 1.5.

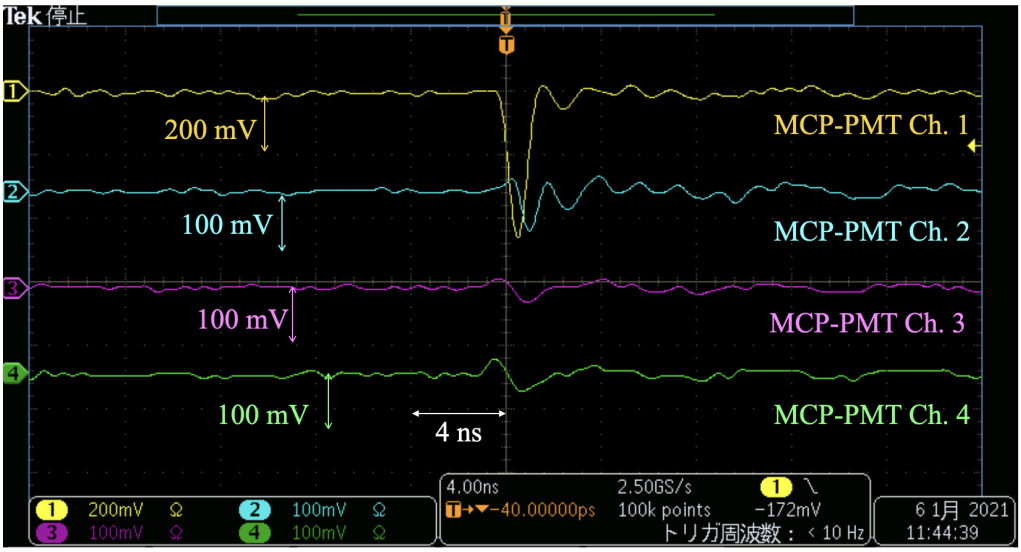

Fig.3. Signals from four channels of MCP-PMT with aerogel (n=1.01) are observed by an oscilloscope. A typical photoelectron signal has a waveform that can be seen in channel 1. The crosstalk signals are found in channel 2 - 4. Photoelectron signal (negative) induces positive signals neighboring pads. The signal bounces back in a negative direction and then reducing with oscillation. The first negative signal in crosstalk is delayed about 1 - 2 ns from photoelectron signal.

The TOF distribution of photoelectron candidate is superimposed as red histogram in Fig. 4. The red histogram is fit by gaussian, and we selected earlier than 2 σ far timing from peak as the hit of photoelectron.

The selection of photoelectron hit by TOF range was processed channel for each channel. The number of photoelectron distribution is shown in Fig. 5. The tail shown in Fig. 2 is disappeared. We obtained 1.4 as average number of photoelectrons by fitting.

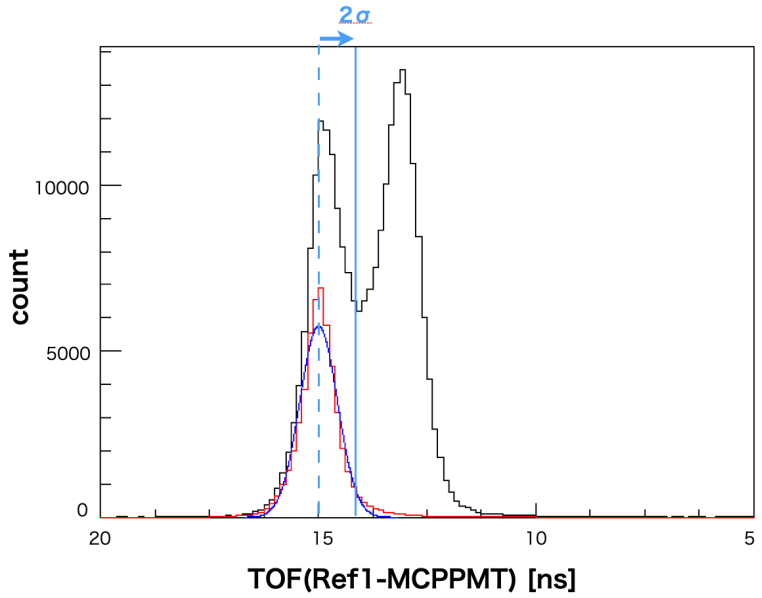

Fig.4. TOF distribution of MCP-PMT in a given channel. Smaller number (right hand direction) means later hit signal on MCP-PMT.

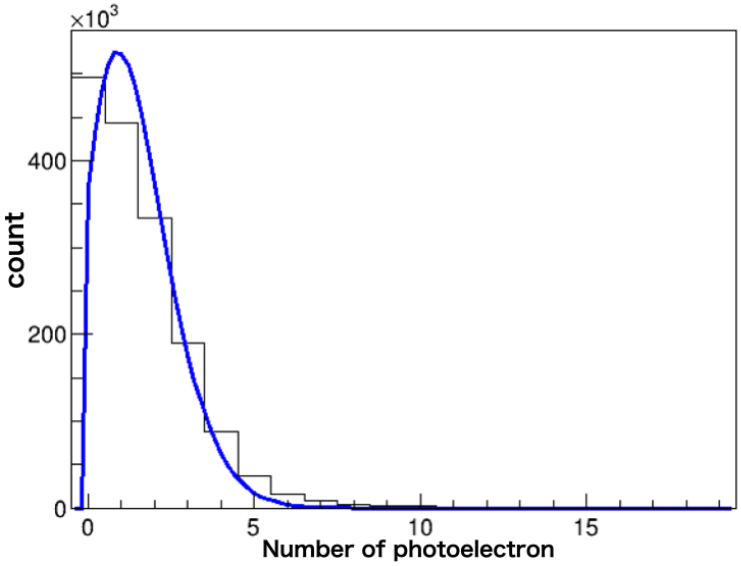

Fig.5. The number of photoelectrons are obtained after crosstalk removal. The tail in large number of hits seen in Fig. 2 has been removed. The average number of photoelectrons is 1.4 by fitting of Poisson distribution.

§4. Result

From the feasibility study with photon beam, we obtained that the number of photoelectrons was 1.4 after removing the crosstalk. We will use four MCP-PMTs for the actual detector and it indicates that we expect 5.6 photoelectrons with the aerogel.

Previous experiments had shown that the trigger rate was about 2 kHz and the efficiency is 65% when the tagged photon rate was 3.5 MHz. The Λn FSI experiments will be conducted at a maximum of 5 MHz tagged photon rate. In the condition, the trigger rate will be more than 4 kHz and the DAQ efficiency will be dropped down to less than 50%.

By installing the aerogel electron veto counter with MCP-PMT, 99.6% of electron and positron events can be removed when more than one hit is required. Even if requiring more than two hits, 97.8% of events can be removed. The trigger rate on the tagged photon rate of 5 MHz is expected as more than several kHz. The removing power makes the trigger rate less than order of a few 10 Hz at 5 MHz tagged photon rate by one photoelectrons requirement.

§5. Summary

We are planning to perform the Λn FSI experiment under high tagged photon rates (up to 5 MHz). In the experiment, we are concerned about the deterioration of DAQ efficiency due to the large amount of background caused by electron/positron pair production. We plan to introduced the aerogel cherenkov electron veto counter with using MCP-PMT to remove the electron/positron background at the trigger level for efficient data taking. The prototype was fabricated and tested with photon beam. The results shows that the trigger rate became less than a few 10 Hz at 5 MHz tagged photon rate by installing the counter.

Acknowledgment

The authors would like to thank the ELPH accelerator staff for provide the stable operation of accelerator.

References

[1] M. Kaneta *et al.*: Nucl. Instrum. Meth. **A866** (2018) 88-103.

[2] K. Matsuoka *et al.*: Nucl. Instrum. Meth. **A766** (2014) 148-151.

[3] T. Ishikawa *et al.*: Nucl. Instrum. Meth. **A875** (2017) 193-200.

(ELPH Experiment : #2500, #2501)

Status of LEPS2-solenoid experiment in 2020

Atsushi Tokiyasu[1], Yuta Sada[1], and LEPS2 collaboration

[1]*Research Center for Electron Photon Science, Tohoku University, Sendai, 982-0826*

The preparation of LEPS2-solenoid experiment is on-going at SPring-8. This experiment is aiming to investigate various hadron photo-production reactions. In FY2020, data for the detector calibration with a nuclear target was performed following FY2019. Main detectors are almost ready, and detector calibration is scheduled with a liquid hydrogen target in FY2020. Analysis method for Bγ was established and a new detector for the beam monitoring was installed in FY2020.

§1. Overview of LEPS2-solenoid experiment

The LEPS2-solenoid experiment is an upgrade experiment of LEPS experiment at SPring-8. It is aiming to study hadron photo-production mechanism by using a high-intensity γ beam (upto 5 Mcps) and a large detector spectrometer system. γ beam is produced via a backward Compton scattering with the energy range from 1.4 to 2.9 GeV. The overview of the LEPS2 spectrometer system is shown in Fig. 1. The LEPS2 spectrometer system is composed of Start Counter(SC), Time Projection Chamber(TPC), Drift Chambers(DCs), Aerogel Cherenkov Counter (AC1, AC2), Resistive Plate Chamber (RPC), and Barrel-γ. These detectors are installed inside solenoid magnet with the strength of 1T, and used to detect both of charged particles and γs from the hadron reactions. The performance of each detector is reported elsewhere.

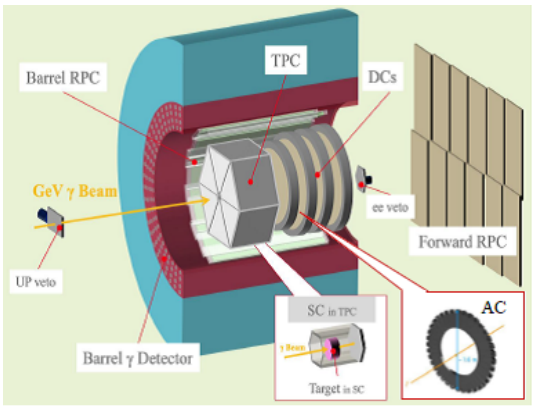

Fig.1. LEPS2 spectrometer system

§2. Progress in FY2020

Following the previous year, we continued taking the data for the detector calibration by using a nuclear target made of copper or polyethylene . Main progresses in FY2020 is 1) the establishment of the analysis technique of Bγ, which is EM calorimeter surrounding the target [1] and 2) the installation of a beam monitor system [2].

As for 1), Bγ gains were found to be unstable because the photo-multipliers were operated the magnetic field. We installed additional magnetic shield for each PMTs, and confirmed the MIP peaks with cosmic-ray data **??**. By using this peak, we can perform the gain tuning of each segment.

As for 2), we installed a scintillator-based beam rate monitor near the beam dump2. By changing the focusing point of laser injected to the storage ring, we measured a energy dependence of the transmission 3. We confirmed that the transmission varies depending on the beam condition. This results will be used for reducing systematic error for the long-term data taking.

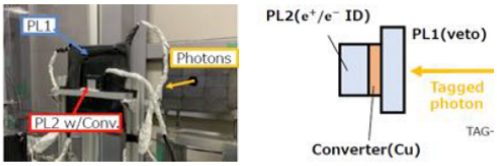

Fig.2. Setup for the transmission measurement

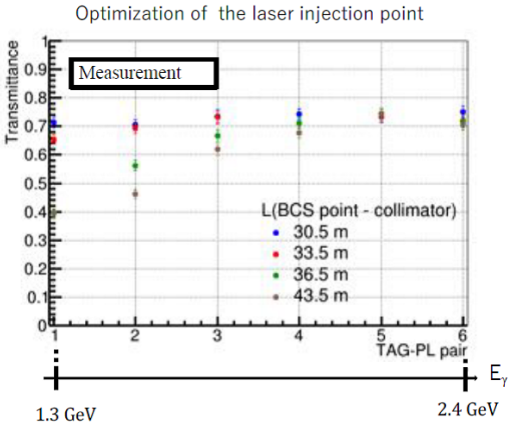

Fig.3. Transmission v.s. Photon Energy

In addition to these progress, we installed almost all AC2 detectors, and their data taking is on-going.

§3. Plans for FY 2021

Main detectors has become ready by the end of FY2020, we will take the data for the calibration of Tagger, SC, TPC, DC, Bγ, BRPC, FRPC, AC2. From early FY2021, we will start taking data with a liquid hydrogen target. By using this target, we will perform the detector commissioning with various physics channels, such as $\gamma + p \rightarrow K^+ + \Lambda$ reaction. After finishing the commissioning with a liquid hydrogen target, we will start taking data with a liquid deuterium target. The first physics motivation is a search for the $K^- pp$ bound state which decays to Λ and proton. The feasibility study with simulation are on-going. In addition, 3rd layer of Bγ and neutron counter will be newly installed in FY2021. The data taking system is under preparation.

References

[1] R. Mizuta: Master Thesis, Gifu Univ.

[2] H. Saito: Master Thesis, Tohoku Univ.

(ELPH Experiment : #2958)

Evaluation of silicon sensors with high timing resolution

Taikan Suehara[1], Mami Kuhara[1], Yu Kato[2]

[1]Department of Physics, Faculty of Science, Kyushu University（744 Motooka, Nishi-ku, Fukuoka 819-0395）

[2]Department of Physics, Graduate School of Science, the University of Tokyo

（7-3-1 Hongo, Bunkyo-ku, Tokyo 113-0033）

We are developing silicon sensors with high timing resolution. Three inverse-type avalanche photodiodes (APDs) were placed on the beam to obtain signal strength and timing correlation by the positron beam at ELPH. Signal of 5-100 fC was observed, and timing resolution of ~200 psec were obtained, mainly due to the jitter caused by analog noise. Further improvements on the readout electronics are necessary to evaluate the timing performance of APDs more precisely.

§1. ビームテストの概要

本グループは、国際リニアコライダー(ILC)におけるカロリメータでの活用を目指し、時間分解能のよいシリコンセンサーとして LGAD (Low Gain Avalanche Detector)の研究を行っている。LGAD は LHC アップグレードのため開発が進んでおり、従来の半導体検出器としてのシリコンセンサーにアバランシェ増幅層を付加することにより 30 ピコ秒程度の高い時間分解能が得られるデバイスである[1]。我々は従来のリーチスルー型と共に増幅層が内部にあることで位置依存性を減らし、時間分解能も改善できる可能性があるインバース型も検討している。従来から光センサーとして用いられる APD (Avalanche Photo-Diode)は LGAD と同等の構造を持つため、我々は数種類の内部構造が異なる浜松ホトニクス社製 APD の荷電粒子による反応を調べている。

本ビームテストは APD のビームに対する応答(信号強度、位置分解能)を測定するために行った。ビームタイムは 2021 年 2 月 16 日～19 日で、別のグループと共同で行った。(優先権は 2 日間。) 陽電子のエネルギーは約 770 MeV である。測定器には 3 個の同種の APD センサーをスタックし、Skiroc2-CMS という ASIC に接続してその信号強度および時間情報の読み出しを行った。Skiroc2-CMS はセルフトリガーで動作し、2 つ以上の APD から閾値を超える信号が得られた場合に、その時間差から時間分解能を求めることができる。

§2. センサーの応答

インバース型APD S8664-50Kの応答(信号強度)を図1に示す。Ch39は3個のAPDのうち中央のセンサーであり、残りの2つのAPDにヒットがあった場合ほとんどの場合粒子が通過すると期待される。青と緑の線はセルフトリガーであり、トリガー閾値の都合で約20 fCを越える電荷量(増幅後)の信号のみが検出されている。赤は両端のAPDのみでトリガーをかけた場合であり、信号は5

fC程度から得られていることがわかる。これは通常のシリコンセンサーの信号量と同等であり、APDの感度層の薄さがゲインと相殺されていると考えられる。

図2は2つのセンサーのtiming correlationを示したものである。信号量は2つとも30-40 fCとし、time walkは補正している。2つの信号の間には明らかなtiming correlationが見られたが、これから1チャンネル当たりの時間分解能を求めると270 psecとなった。チャンネルや信号量により多少の違いは見られるが、今回の測定では200ピコ秒を大きく下回る時間分解能は得られなかった。これは予測される30ピコ秒程度の時間分解能より明らかに悪い。この原因として、Skiroc2-CMSのノイズと立ち上がり時間によるアナログジッターが予想される。アナログジッターは信号の時定数とノイズに関係しており、Charge injectionを用いてSkiroc2-CMSのジッターを計測すると、ノイズ環境にもよるが30 fCの信号量では200ピコ秒程度のジッターが存在した。Skiroc2-CMSは電力消費の制限とカロリメータに用いるため広いダイナミックレンジが要求されることからノイズ性能は十分高いとは言えない。(信号量が多ければ50ピコ秒以下の時間分解能は得られる。)

今回の測定では、前回(2019年[2])に得られた約400ピコ秒程度よりはよい時間分解能が得られたが、今後更に精度のよい測定には更に低ノイズかつ高速のアンプが必要となる。今回得られた信号量を基準に、高速アンプおよびノイズ軽減策により今後高精度の時間測定を目指す。

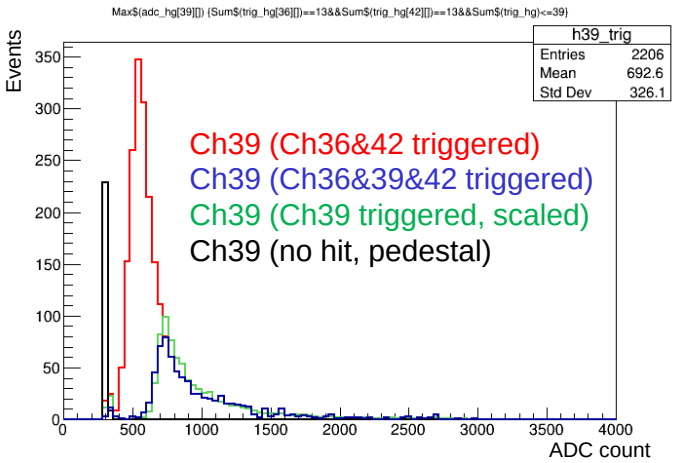

図 1 S8664-50K の ADC 分布。900 ADC count がおよそ 30 fC の電荷量に相当。

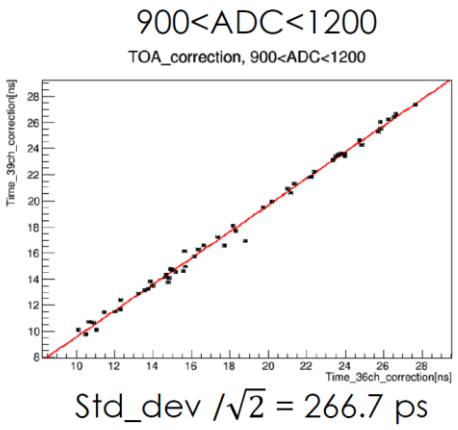

図 2 2 つの S8664-50K を用いた時間相関。30-40fC の信号において 266.7 psec の相関が得られた。

謝辞

ビームテストに当たりELPH加速器の運転および受け入れを行っていただいたELPHスタッフの皆様、特に直接受け入れを担当いただいた宮部学氏に感謝します。

参考文献

[1] McCarthy, Thomas G., Upgrade of the ATLAS Liquid Argon Calorimeters for the High-Luminosity LHC, arXiv:1612.07102 (2016).

[2] Taikan Suehara, Yuto Deguchi, Yuto Uesugi, Yu Kato, and Ryo Yonamine, Development of novel silicon sensors with high time and spatial resolution, arXiv:2101.01996 (2021).

Development of the multi-layer mirror for the production of a high-energy photon beam by X-ray Compton scattering

Norihito Muramatsu[1], Shinsuke Suzuki[2], Haruo Ohkuma[3,4], Schin Daté[3], Kazuhiro Kanda[5], Shuji Miyamoto[5], Tetsuo Harada[5], Takeo Watanabe[5], Hajime Shimizu[1], Manabu Miyabe[1], Atsushi Tokiyasu[1], and Masahiro Okabe[1]

[1]*Research Center for Electron Photon Science, Tohoku University, Sendai, Miyagi 982-0826, Japan*
[2]*Japan Synchrotron Radiation Research Institute (SPring-8), Sayo, Hyogo 679-5198, Japan*
[3]*Research Center for Nuclear Physics, Osaka University, Ibaraki, Osaka 567-0047, Japan*
[4]*Aichi Synchrotron Radiation Center, Seto, Aichi 489-0965, Japan*
[5]*Laboratory of Advanced Science and Technology for Industry, University of Hyogo, Kamigori, Hyogo 678-1205, Japan*

§1. Introduction

We are developing a new method to produce a high-energy photon beam via Compton scattering of X-rays at an electron storage ring. In our project [1], soft X-rays of 92 eV are obtained from a short undulator (total length: 2.28 m, period length: 7.6 cm) installed in the straight section for BL07 at NewSUBARU, and backwardly reflected into the storage ring by using a Mo/Si multi-layer mirror. This method can increase the maximum energy of a produced photon beam up to 0.58 and 1.02 GeV for the electron beam energy of 1 and 1.5 GeV, respectively. These maximum energies are significantly higher than that achieved by laser Compton scattering, which has been usually adopted for a γ-ray source.

We have set up a large mirror chamber at BL07A [2] to place the Mo/Si multi-layer mirror with automatic stepping-motor stages in a vacuum of 10^{-6} Pa. An initial version of the mirror is put on an oxygen-free copper holder with water cooling. In addition, we have installed an X-ray wire scanner and gamma detectors [3]. The wire scanner measures profiles and intensities of both radiated and reflected X-ray beams, while the gamma detectors are used to get a rate, profile, and energy spectrum of the photon beam. The performances of these detectors have been individually examined at BL07A by using X-rays from the undulator and γ-rays from the residual-gas bremsstrahlung [4]. Now we are testing the Mo/Si multi-layer mirror and further developing a technique of X-ray reflection in the backward direction for the injection into a storage ring. This report describes the results of basic tests for the multi-layer mirror in terms of surface condition, heat load, and X-ray reflection.

§2. Examination of surface condition

A substrate of the Mo/Si multi-layer mirror is made of a low thermal expansion glass ceramic (Zerodur) with an area of 50×50 mm^2 and a thickness of 5 mm. Its reflective surface is cylindrically polished to make a focus on the electron beam at the 16.7-m upstream straight section of the storage ring. This

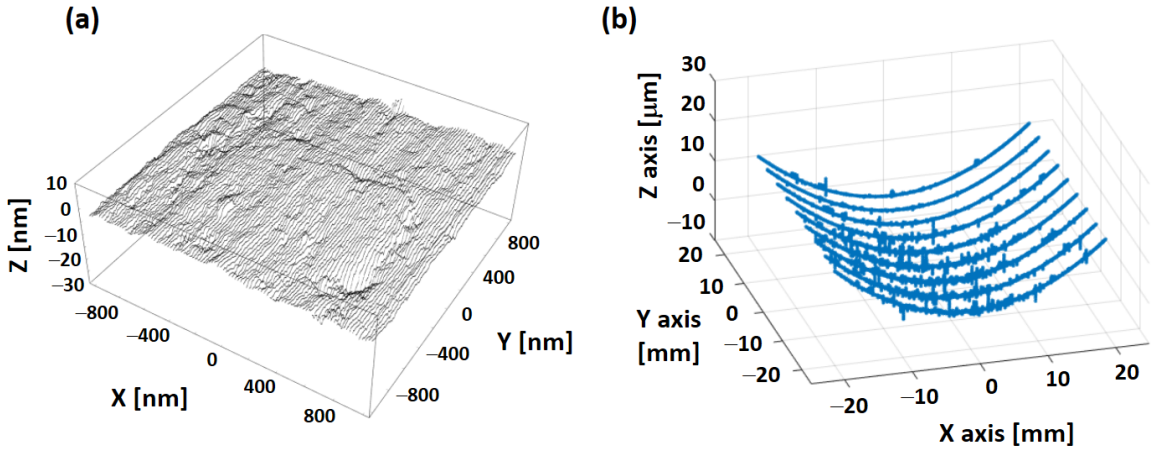

Fig.1. (a) Mirror surface roughness measured by an atomic force microscope in an area of 2×2 μm^2. (b) Mirror surface accuracy measured by an ultrahigh accurate 3D profilometer in an area of 40×40 mm^2.

cylindrical surface was made by bending the substrate with application of stress at two edges, then polishing a surface flatly, and finally releasing the stress [3, 4]. A curvature radius of the cylindrical surface, corresponding to the focal length of 16.7 m, was confirmed by measuring a depth of the mirror center and alternatively counting the number of Newton fringes. The reflective surface was coated by Mo/Si multi-layers with 50 periodic repetitions.

We examined the surface condition of a mirror substrate after polishing. The measurement was done at National Metrology Institute of Japan, which is a research center of AIST. Figure 1(a) shows a result of surface roughness obtained for a region of 2×2 μm^2 by using an atomic force microscope (AFM). The RMS value of surface roughness was measured to be 0.99 ± 0.46 nm without anisotropy. It was confirmed that the surface roughness of our multi-layer mirror is moderately good for the reflection of 92-eV X-rays ($\lambda = 13.5$ nm). Simultaneously, we measured surface accuracy in the central region of 40×40 mm^2 by using an ultrahigh accurate 3D profilometer. As shown in Fig. 1(b), a cylindrical surface is clearly formed even by using the unique method mentioned above. A mean curvature radius was measured to be 14.38 ± 0.06 m, which was shorter than the design value.

§3. Heat load test with X-ray irradiation

The heat resistant temperature of a Mo/Si multi-layer mirror is known to be 300°C. In addition, high heat load may result in the distortion of a mirror surface, although we adopted a low thermal expansion glass ceramic as a mirror substrate. Therefore, we tested heat load by irradiating X-rays on the multi-layer mirror that was installed inside the large mirror chamber at BL07A.

Figure 2 shows a result of temperature change when X-rays are incident on the mirror in a region of 10×10 mm^2 with the undulator setting where a component of 92 eV is peaked as the third harmonics of radiation. The mirror temperature was obtained by using a radiation thermometer thorough a ZnSe window, which was newly attached to the large mirror chamber for infrared transmission. In Fig. 2,

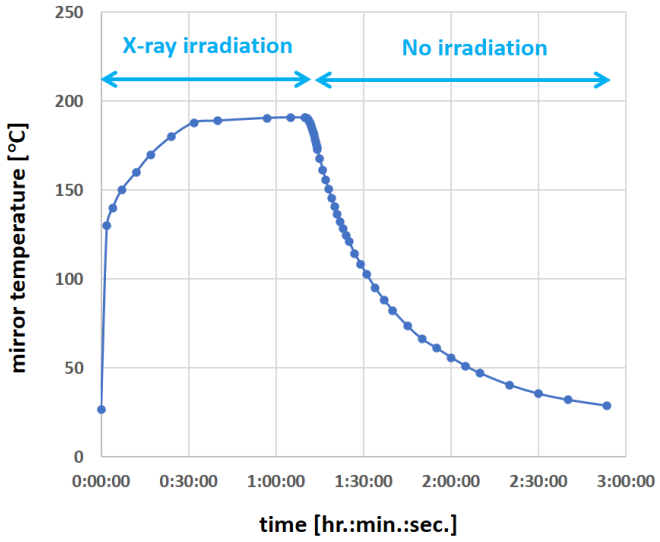

Fig.2. Temperature change of the Mo/Si multi-layer mirror with the irradiation of X-rays in an area of 10×10 mm^2. The irradiation was stopped after 70 minutes.

X-rays were irradiated for the first 70 minutes. A temperature of the whole mirror increased by about 100°C in two minutes and reached 190°C at maximum. After stopping the irradiation of X-rays, the mirror temperature gradually dropped over 100 minutes by thermal radiation. We have also confirmed that water cooling of the mirror holder was not effective because of bad heat conductance.

Expected heat load was estimated to be a few Watt by taking into account higher harmonic radiation that was not reflected. Nevertheless, bad heat contact of the multi-layer mirror in a vacuum causes a rapid increase of its temperature. We confirmed that the maximum temperature was lower than the heat resistant temperature of Mo/Si multi-layer coating.

§4. X-ray reflection test at BL07A

We further tested the performance of the installed Mo/Si multi-layer mirror. As described above, profiles and intensities of radiated and reflected X-rays can be monitored by using the wire scanner where micro current due to a photoelectric effect is detected with wire position shift. Figure 3 shows a result of vertical scanning with a horizontal wire. The profile of reflected X-rays is clearly seen beside a large peak of undulator-radiated X-rays, which contains high harmonic radiation other than a 92 eV component. In this measurement, an elevation angle of the Mo/Si multi-layer mirror was upwardly shifted so that the reflected X-ray profile should not overlap with the incident X-rays. A position of the reflected profile moves depending on the mirror angles, and adjustment of the reflected X-ray axis can be done based on the relation between the profile position and the angle setting.

§5. Prospect of the X-ray Compton scattering experiment

We are going to demonstrate the production of a high-energy photon beam via Compton scattering of soft X-rays from electrons in the storage ring, for the first time. Based on the above studies, we are

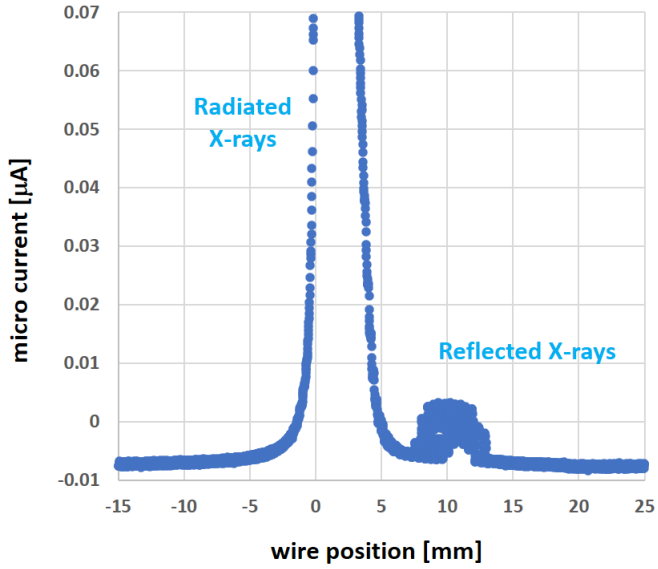

Fig.3. Vertical profiles of radiated and reflected X-rays, obtained by the wire scanner that measures a micro current with the shift of wire position.

producing a second multi-layer mirror by introducing a silicon substrate and a thermal contact sheet for better heat conductance to the water-cooled mirror holder. We expect an improvement of surface distortion, caused by heat load. We are adopting fluid polishing to achieve better surface roughness and accuracy. We aim for the surface roughness of 0.5 nm in RMS. After the polishing is completed, we will form Mo/Si multi-layers on the reflective surface and install the new mirror at BL07A to proceed with the demonstration experiment. Our development of a high-energy photon beam source will be helpful for next-generation researches of hadron photoproduction experiments.

References

[1] http://www.rcnp.osaka-u.ac.jp/ mura/kaitaku/

[2] S. Tanaka, S. Suzuki, T. Mishima and K. Kanda, J. Synchrotron Rad. **28** (2021) 618.

[3] M. Okabe, Master thesis (Tohoku University, 2020).

[4] N. Muramatsu et al., J. Particle Accelerator Society of Japan Vol.**16** No.3 (2019) 154.

Direct measurement of the η' mass inside a copper nucleus at the BGOegg Phase-II experiment

Norihito Muramatsu[1], Manabu Miyabe[1], Atsushi Tokiyasu[1], Yuji Matsumura[1], Hajime Shimizu[1], and Tomoaki Hotta[2]

[1]*Research Center for Electron Photon Science, Tohoku University, Sendai, Miyagi 982-0826, Japan*
[2]*Research Center for Nuclear Physics, Osaka University, Ibaraki, Osaka 567-0047, Japan*

§1. Introduction

The mass of a hadron composed of u, d, and s quarks cannot be described by a sum of their current-quark masses, generated by interactions with the Higgs field. For example, such a sum accounts for only about 1% of the nucleon mass. Thus, a dynamical mechanism of hadron-mass generation proposed by Nambu is widely believed in modern physics. In this mechanism, the quantum-mechanical vacuum changes its ground-state properties by the spontaneous breaking of chiral symmetry as the universe evolves from a high-temperature and high-density plasma of massless quarks. This phenomenon is called chiral phase transition, and its order parameter is a vacuum expectation value of quark condensates. Under the spontaneous breaking of chiral symmetry, a constituent quark mass is given to a quark through interactions with the quark condensates.

In recent years, the η' meson has attracted much attention for studying the origin of a hadron mass. The main component of η' is a singlet state in the flavor $SU(3)$ nonet of pseudoscalar mesons. Its mass (958 MeV/c^2) is extraordinarily heavier than the other octet members, corresponding to Nambu-Goldstone bosons. Historically, the η'-meson mass has been explained by the $U_A(1)$ quantum anomaly [1, 2]. However, it is also known that the η' and other mesons like π, σ, and η must degenerate when the chiral symmetry is restored [3]. This means that the mass generation in η' is closely related with both the $U_A(1)$ quantum anomaly and the spontaneous breaking of chiral symmetry. In addition, it has been theoretically found that the spontaneous breaking of chiral symmetry can be caused if the $U_A(1)$ quantum anomaly is strong enough [4].

Efforts to prove the mass-generation mechanism have been actively attempted in the field of hadron physics. Partial restoration of the chiral symmetry is expected to take place inside a nucleus, which has an ultra-high density of about 10^{14} g/cm^3, as a precursor phenomenon of the chiral phase transition. So far, the amount of η'-mass reduction at the normal nuclear density has been theoretically calculated in the frameworks of the Nambu-Jona-Lasinio (NJL) model [5], the linear sigma model [6], and the quark-meson coupling (QMC) model [7]. Unfortunately, the predicted reduction varies in the range from 40 to 150 MeV/c^2. From the experimental side, smaller amounts of the mass reduction, which do not exceed 50 MeV/c^2, have been indirectly suggested by the $\eta' N$ scattering length measured at COSY-11 [8] and the results of a nuclear transparency ratio and differential cross sections by the CBELSA/TAPS

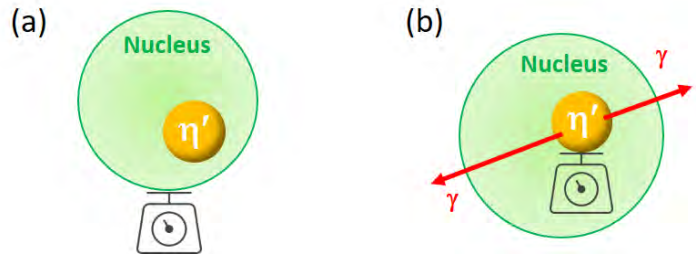

Fig.1. Two methods to observe the η' mass reduction inside a nucleus through (a) the η'-bound nuclei search and (b) the $\gamma\gamma$ invariant mass measurement.

Collaboration [9–13]. Recently, the η-PRiME/Super-FRS Collaboration searched for η' bound nuclei by a missing mass spectroscopy in the $^{12}C(p,d)$ reaction. They observed no signals over large backgrounds [14, 15], and claimed that a large mass reduction like the NJL calculation is unfavored.

The BGOegg experiment, running at SPring-8 LEPS2 beamline [16], has also searched for η'-mass reduction signals in a Carbon nucleus by two complementary methods. Details of the analysis methods and results in the Phase-I experiment are described in Ref. [17]. In one analysis, a missing mass spectroscopy was carried out to search for η' bound nuclei in the $^{12}C(\gamma,p)$ reaction [18]. No signals were observed although the signal sensitivity was raised up by the detection of a nuclear absorption signal via $\eta' N \to \eta N$ for the first time. The experimental upper limit of the production cross section for the η' bound nuclei was compared with a theoretical calculation using distorted wave impulse approximation (DWIA) [19], and this analysis concluded that a large mass reduction such as the optical potential of $V_0 = -100$ MeV is not favored.

In the second method to study the η' mass in Carbon nuclei, we focused on a lineshape analysis for the $\gamma\gamma$ invariant mass in the $\eta' \to \gamma\gamma$ decay [20]. If the mass reduction exists at the nuclear density, a component decaying inside a nucleus may be observed at the lower mass side of a quasi-free η' peak. In order to increase the fraction of $\gamma\gamma$ decays inside a nucleus, we selected η' mesons whose momentum was lower than 1 GeV/c. An excess of event entries over the sum of background functions was examined by fitting them without using a low mass range. In addition, we performed a χ^2 difference test to compare two fitting results in the cases of only using background functions and adding a signal function. As a result, a possible signal excess was indicated with the statistical significances of 3–4σ and a favored range of the mass reduction was estimated to be approximately 40–70 MeV/c^2. We are now performing further confirmation analyses using existing additional data that have a comparable statistics.

The search for the η'-bound nuclei corresponds to an indirect measurement of the η' mass because it measures the mass of a system containing an η' meson and a nucleus. (See Fig. 1(a).) In reality, the η'-bound state can be confirmed when the mass structures due to bound orbits are precisely observed. In contrast, the lineshape analysis for the the $\gamma\gamma$ invariant mass reconstructed by using the BGOegg calorimeter should be the direct measurement of an η' meson inside a nucleus, as shown in Fig. 1(b). In the measured mass spectrum, even small reduction by several tens of MeV is detectable through a spectral change at the lower tail of a quasi-free η' peak. The BGOegg experiment has an advantage in such an analysis thanks to the world's best energy resolution of the large solid-angle electromagnetic

calorimeter in the energy region below 1 GeV.

§2. Setup of the BGOegg Phase-II experiment

As described above, various experimental results indicate the η' optical potential or the η' mass reduction is not very large as -100 MeV. We apparently need to conduct a high-statistics experiment to confirm the BGOegg Phase-I result for the lineshape analysis of an η' mass spectrum. Therefore, we plan to concentrate on the experimental procedure to measure a $\gamma\gamma$ invariant mass distribution by the BGOegg calorimeter. This procedure is currently only a way to directly reveal the nature of the η' meson inside a nucleus. We set a goal so that an enough signal sensitivity can be achieved over the fluctuation of backgrounds. For this purpose, we upgrade the BGOegg experimental setup as follows:

1. A nuclear target will be replaced from a 20-mm thick carbon block to a copper plate. The radius of a copper nucleus is 1.8 times larger than that of a carbon nucleus, so that a rate of in-medium η'-meson decays is increased. In addition, the target thickness will be increased from 0.1 to 0.5 radiation lengths, corresponding to the copper-plate thickness of 7 mm. A weight per the unit area becomes 1.8 times heavier for the new copper target than that for the carbon target used in the Phase-I experiment. This allows us to collect high statistics data in the Phase-II experiment. Even though the target weight is increased, the actual thickness of the copper target is still thinner, resulting in less ambiguity of reaction vertices. Since the η' mass resolution is determined not only by the energy resolution of a calorimeter but also by the angular accuracy of reconstructed γ's, it will be improved to about 60% of the Phase-I resolution. A test experiment with one-week data taking by using a copper target shows an η' mass resolution of 13 MeV/c^2 in the $\gamma\gamma$ decay mode.
2. As recognized in the BGOegg Phase-I experiment, a majority of widely distributed backgrounds come from multiple π^0 photoproduction. It was not fully removed because some of final state γ's escaped from the acceptance hole of the BGOegg calorimeter, existing in the polar angles less than 24 degrees. Thus, we cover this forward region by another electromagnetic calorimeter, as described below. A plastic-scintillator wall is also under development for charge identification of forward particles, detected at the new calorimeter. These detector upgrade will reduce the multi-meson backgrounds by an order of magnitudes. In addition, we are considering to expand forward acceptance of the BGOegg calorimeter by adding new BGO crystals. A gap between the current BGOegg calorimeter and the new forward calorimeter will be removed by this expansion, resulting in a higher rejection power for multi-meson backgrounds.
3. An intensity of the photon beam available at the LEPS2 beamline will be increased by introducing pulsed lasers instead of conventional CW lasers. The pulsed laser newly developed by Spectronix Corp. can emit ultraviolet (or deep-ultraviolet) light at a timing synchronized with an electron bunch in the storage ring. All the available laser power is efficiently usable for the production of high energy photons via Compton scattering at the laser focus point. We intend to operate two pulsed lasers simultaneously for the purpose to double the photon beam intensity.

Following the above basic concepts of experimental upgrades, we plan to prepare a new setup of

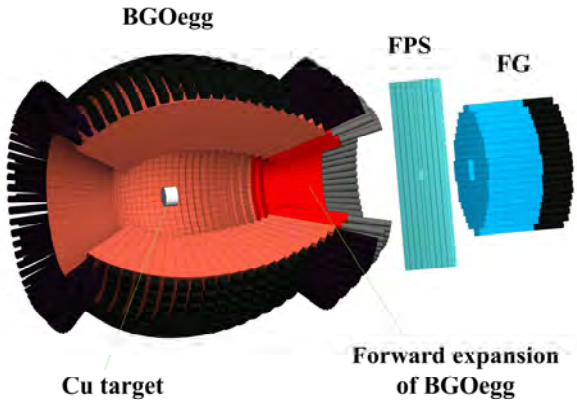

Fig.2. A planned detector setup in the BGOegg Phase-II experiment.

the BGOegg Phase-II experiment. At the LEPS2 beamline, a photon beam is produced by injecting laser light with the wavelength of 355 nm into the storage ring of 8-GeV electrons. The maximum energy of the photon beam reaches 2.4 GeV. Individual photon energy is measured by detecting a recoil electron at the tagger in the range above 1.3 GeV with an energy resolution of 12 MeV. The tagger also counts the reaction rate of Compton scattering to measure a photon beam intensity. Recently we have introduced a pulsed laser at the LEPS2 beamline [21]. A photon beam intensity of 1–3 $\times$ 10^6 s^{-1} is being available with injection of the pulsed laser depending on the output power, frequency, and timing structure. We will install another pulsed laser and aiming a total intensity of 3–6 $\times$ 10^6 s^{-1}.

We have constructed a large-acceptance electromagnetic calorimeter covering a polar angle range of 24 to 144 degrees. We assembled 1320 $Bi_4Ge_3O_{12}$ (BGO) crystals in an egg-shape ("BGOegg" calorimeter). Each crystal has a depth of 20 radiation lengths with an inner-side cross section of about 20 $\times$ 20 mm^2. There are no support materials between the crystals. The energy resolution for 1-GeV γ-rays is 1.3% [22]. The energy resolution and fine segmentation of the BGOegg calorimeter provide the world's best mass resolution for neutral mesons like π^0, η, η', etc. We have additionally installed a cylindrical drift chamber and hodoscopes into the inner volume of the BGOegg calorimeter so that charged and neutral particles can be distinguished from each other for hits in the BGOegg calorimeter.

Geometrical acceptance of the BGOegg calorimeter is missing in the foraward region below 24 degrees. We largely loose the acceptance to detect multi-meson photoproduction reactions whose final state includes many γ's. In the BGOegg Phase-II experiment, we are thus preparing another γ-ray detector used at forward angles ("Foward Gamma" or "FG"). Figure 2 shows a planned experimental setup, where the FG is placed on the most downstream. We already developed the FG in past experiments and the acceptance for neutral particles can be recovered by adopting this detector in addition to the BGOegg calorimeter. The FG consists of 252 $PbWO_4$ (PWO) crystals, whose individual size is 22 $\times$ 22 $\times$ 180 mm^3. After assembling the PWO crystals, the total width and height of the sensitive region both reach 418 mm at the upstream surface. In case that the FG is installed at 700 mm downstream from the target, it will cover 3–16 degrees at forward angles. We also install a wall of newly developed charged-particle identi-

fication counters (called "Forward Plastic Scintillators" or "FPS") in front of the FG. The FPS consists of two layers, where the direction of long plastic scintillators is perpendicular to each other. In each layer, 10 scintillators are arranged in a wall of 700×700 mm^2. Signals from the FPS are read out by MPPCs located at both sides of the individual scintillator.

There remains a gap for neutral-particle detection between the BGOegg calorimeter and the FG, corresponding to the polar angle range of 16–24 degrees. We plan to cover this region by adding a few layers of BGO crystals in the Phase-II experiment. If most of the solid angles are covered by electromagnetic calorimeters, we can explore wider physics possibilities other than the studies of η' mass in nuclei; For example, it becomes possible to investigate higher resonances coupling with multiple π^0 and η.

§3. Prospects of the Phase-II experiment

We are going to use a copper target instead of a carbon target. While the radius of a carbon nucleus is 2.7 fm, that of a copper nucleus increases to 4.8 fm. If η' mesons are produced inside a nucleus that has a larger radius, the probability of decays in the environment with a nuclear density becomes higher. Table 1 shows the estimated ratio of in-medium decays in the $\eta' \to \gamma\gamma$ channel under the assumption that its partial decay rate is unchanged in the nucleus and the outside vacuum. This ratio depends on the requirement to select low-momentum η' mesons. Here we simulated the η' production and decays inside a nucleus by taking into account the Woods-Saxon type density distribution and the density dependence of production and decay rates. Because data statistics become significantly high in the BGOegg Phase-II experiment, we can select the momentum region whose upper boundary is lower than that of the Phase-I experiment. In case of using a copper-nucleus target and selecting the η' momentum less than 600 MeV/c, the ratio of in-medium decays is about 5 times of that in the Phase-I experiment.

Installation of additional forward calorimeters is essential to enhance the statistical significance of η'-mass reduction signals by decreasing multi-meson backgrounds down to a low level. A good signal-to-noise ratio is a key to exclude possibilities of mistakenly recognizing the enhancement due to unknown systematic uncertainties as signals. For the case of combining the FG with the BGOegg calorimeter, we estimated a rejection factor against the $\gamma p \to \pi^0\pi^0 p \to 4\gamma p$ reaction, which should be dominant as a background source. This reaction was generated in the Monte-Calro simulation with a realistic experimental setup, and a set of event selection conditions used in the analysis of the Phase-I experiment were required to the generated sample. As shown in Fig. 3, the rejection factor is estimated to be 8.1 ± 0.5, corresponding to the background reduction by about one order of magnitude, in the region near the nominal η' mass. If we expand the forward acceptance of the BGOegg calorimeter by adding new BGO crystals and cover the gap to the FG, the rejection factor will increase up to 40.

Table 1. Estimated ratios of $\eta' \to \gamma\gamma$ decays before η' mesons go out of a nucleus. The estimation was performed depending on the sample selection condition of η' momenta.

Momentum selection	< 400 MeV/c	< 600 MeV/c	< 1000 MeV/c
C target ($r = 2.7$ fm)	0.7%	0.5%	0.2%
Cu target ($r = 4.8$ fm)	1.7%	1.0%	0.4%

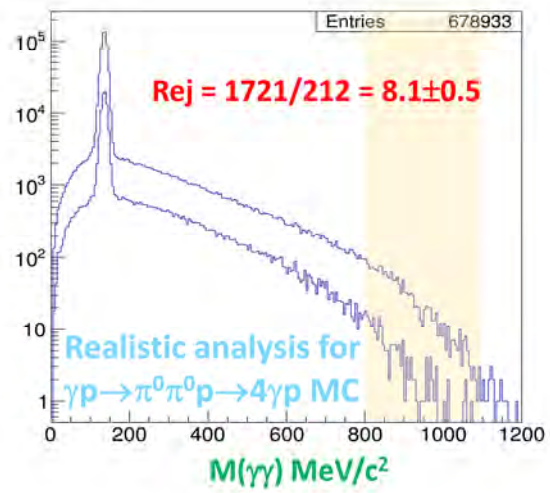

Fig.3. Invariant mass distributions of $\gamma\gamma$ pairs for a realistic Monte-Carlo simulation of the $\gamma p \to \pi^0\pi^0 p \to 4\gamma p$ reaction. Two cases with only the BGOegg calorimeter and both of the BGOegg and the FG are overlayed. A background rejection factor by the installation of FG was estimated in the shaded area.

In the direct measurement by the Phase-I experiment, the η'-mass reduction inside a carbon nucleus was indicated as a low mass component below the quasi-free η' photoproduction peak. However, its statistical significance was not high enough, and this indication must be confirmed by a new experimental setup that improves data statistics and a signal-to-noise ratio. In the BGOegg Phase-II experiment, we are planning to use a copper target with a thickness of 0.5 radiation lengths and a photon beam whose intensity exceeds 3×10^6 s^{-1}. As discussed above, the use of copper nuclei will increase the ratio of in-medium decays 5 times more than that of the Phase-I experiment in the $\gamma\gamma$ momentum region less than 600 MeV/c. At an initial stage of the Phase-II experiment, we will start data collection with the FG and FPS to reduce the multi-meson backgrounds by one order of magnitude. Figure 4 shows a $\gamma\gamma$ invariant mass distiribution, where the signal amount is evaluated by taking into account the estimated key numbers for the Phase-I result. The mean of signal distribution is assumed to be about 920 MeV/c^2 with the sigma of 24 MeV/c^2. In the case of Fig. 4, the statistical siginificance of signals reaches 28σ in two-month data taking. We also plan a subsequent stage experiment for a long term after completing the extension of the BGOegg calorimeter to achieve further background suppression.

References

[1] E. Witten, Nucl. Phys. B 156 (1979) 269.

[2] G. Veneziano, Nucl. Phys. B 159 (1979).

[3] S.H. Lee and T. Hatsuda, Phys. Rev. D 54 (1996).

[4] S. Kono, D. Jido, Y. Kuroda, and M. Harada, Prog. Theor. Exp. Phys. 2021-9 (2021) 093D02.

[5] H. Nagahiro. M. Takizawa, and S. Hirenzaki, Phys. Rev. C 74 (2006) 045203.

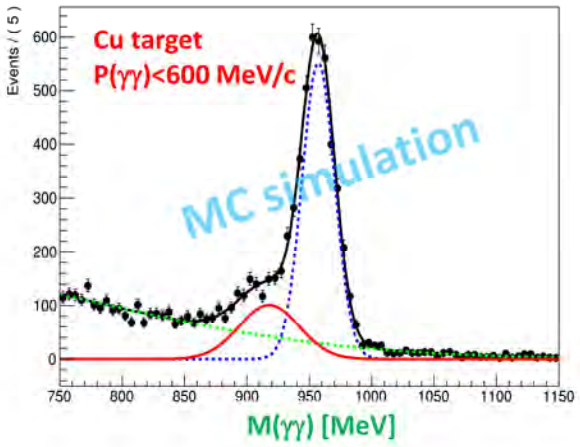

Fig.4. A $\gamma\gamma$ invariant mass spectrum expected in the BGOegg Phase-II experiment with the additional installation of the FG and FPS.

[6] S. Sakai and D. Jido, Phys. Rev. C 88 (2013) 064906.

[7] S.D. Bass and A.W. Thomas, Phys. Lett. B 634 (2006) 368.

[8] E. Czerwinski et al., Phys. Rev. Lett. 113 (2014) 062004.

[9] M. Nanova, V. Metag, A. Ramos, E. Oset, I. Jaegle, K. Makonyi, et al. (CBELSA/TAPS Collaboration), Phys. Lett. B 710 (2012) 600.

[10] M. Nanova, V. Metag, E.Ya. Paryev, et al. (CBELSA/TAPS Collaboration), Phys. Lett. B 727 (2013) 417.

[11] M. Nanova, S. Friedrich, V. Metag, E.Ya. Paryev, et al. (CBELSA/TAPS Collaboration), Phys. Rev. C 94 (2016) 025205.

[12] S. Friedrich, M. Nanova, V. Metag, et al. (CBELSA/TAPS Collaboration), Eur. Phys. J. A 52 (2016) 297.

[13] M. Nanova, S. Friedrich, V. Metag, E.Ya. Paryev, et al. (CBELSA/TAPS Collaboration), Eur. Phys. J. A 54 (2018) 182.

[14] Y.K. Tanaka, K. Itahashi, H. Fujioka, et al. (η-PRiME/Super-FRS Collaboration), Phys. Rev. Lett. 117 (2016) 202501.

[15] Y.K. Tanaka, K. Itahashi, H. Fujioka, et al. (η-PRiME/Super-FRS Collaboration), Phys. Rev. C 97 (2018) 015202.

[16] N. Muramatsu, M. Yosoi, T. Yorita, Y. Ohashi, et al., arXiv:2112.07832 (2021).

[17] N. Muramatsu, et al., ELPH Annual Report 2019 (2020) 59.

[18] N. Tomida, N. Muramatsu, M. Niiyama, et al. (BGOegg Collaboration), Phys. Rev. Lett. 124 (2020) 202501.

[19] H. Nagahiro, JPS Conf. Proc. 13 (2017) 010010.

[20] Y. Matsumura, Doctoral Thesis (Tohoku Univ.), 2021.

[21] H. Katsuragawa, RCNP Annual Report 2020, Osaka Univ. (2021) “Highlights” section.

[22] T. Ishikawa, et al., Nucl. Instrum. Methods A 837 (2016) 109.

(ELPH Experiment : #2500, #2501)

Study of Basic Performance of KOTO Upstream Charged Veto Detector Using ELPH Electron Beam

K. Hanai[1], H. Hiruma[2], H. Ikeda[2], T. Kato[1], K. Kotera[1*], H. Nanjo[1], T. Nunes[1], J. Ohashi[2], N. Shimizu[3], K. Shiomi[4], R. Shiraishi[1], Y. Tajima[2], K. Toho[2], and T. Yamanaka[1]

[1]*Department of Physics, Osaka University, Osaka, 560-0043*
[2]*Department of Physics, Yamagata University, Yamagata, 990-8560*
[3]*International Center for Hadron Astrophysics, Chiba University, Chiba, 263-8522*
[4]*Institute of Particle and Nuclear Studies, High Energy Accelerator Research Organization (KEK), Ibaraki 305-0801*

We developed two types of low-mass charged particle detectors to be placed in the beamline at the upstream end of the KOTO detector system. One was made by arranging 0.5×0.5 mm^2 scintillating fibers in a plane. The other used a 0.2 mm-thick scintillating film, for which scintillation light escaping from the large surfaces of the scintillator was collected. Both performed as expected.

§1. Introduction (KOTO upstream charged Veto detector)

The aim of the KOTO experiment [1, 2] is to study a rare neutral-kaon decay, $K_L \to \pi^0\nu\bar{\nu}$. Its branching fraction predicted by the Standard Model (SM) is small, 3×10^{-11}. This decay mode is a CP violating process and is sensitive to new physics beyond the SM, because some theoretical models predict higher branching fractions. The signature of the decay is two photons from the π^0 decay with no other observable particles.

In the latest published analysis with the data set taken in 2016, 2017, and 2018 at J-PARC, we found a new type of background events originating from charged kaons which were created in the second collimator in the beamline [3] as shown in Fig. 1. We developed a new low-mass charged veto detector to be placed in the beam at the most upstream end of the detector system. The new detector is called Upstream Charged Veto detector (UCV).

This report describes the performance of the UCV studied with the ELPH electron beam.

§2. UCV

We developed two types of UCVs. Figure 2 shows the UCV made of scintillating fibers arranged in a plane (UCV-fiber). The UCV-fiber was installed in the KOTO experiment in 2020 after the beam test at ELPH. Figure 3 shows a prototype of UCV made of a scintillating film (UCV-film).

*corresponding author: coterra@champ.hep.sci.osaka-u.ac.jp

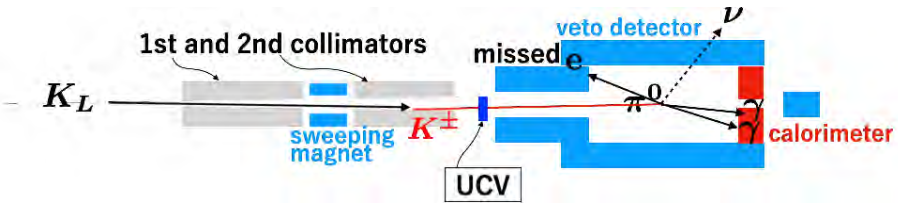

Fig.1. A schematic of a charged kaon generation in the KOTO detector. The UCV is located between the second collimator and the most upstream region of the series of detectors in the vacuum tank.

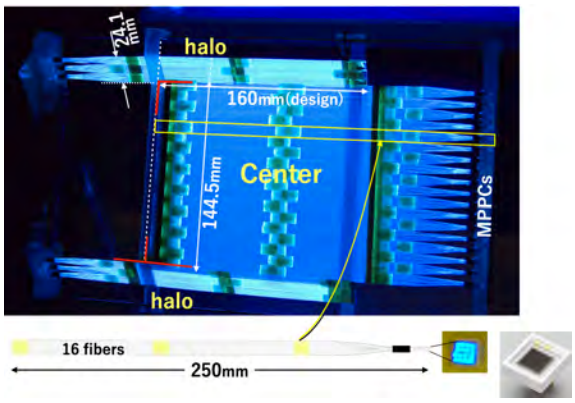

Fig.2. Top: photo of UCV-fiber exposed with black light. Bottom: schematic of a module made of 16 fibers, photo of light coming from 16 fibers, and an MPPC receiving the light.

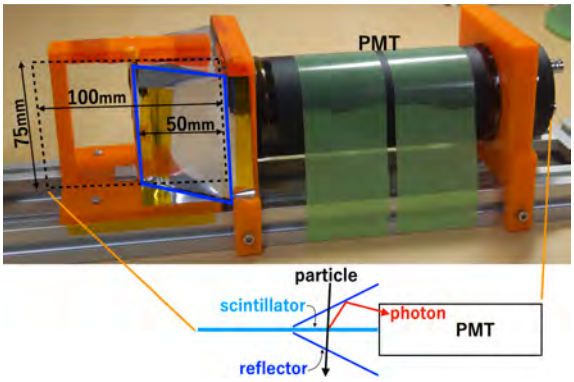

Fig.3. Top: photo of the prototype of UCV-film. Dashed lines show the shape of the scintillating film. Blue lines show the shape of the reflecting foil on the front side. Bottom: schematic showing the concept of UCV-film.

2.1 UCV-fiber

In UCV-fiber, sixteen 0.5×0.5 mm^2 scintillating fibers form a $250 \times 8.0 \times 0.5$ mm^3 scintillating strip as shown in Fig. 2 Bottom. Each strip is read out with a Multi-pixel photon counter (MPPC) [†]. Eighteen strips are used to form a 145×190 mm^2 center detection area, and two sets of three strips are used to cover two outside areas, called "halo regions". [‡] To reduce the inefficiency of detector due to gaps between scintillating fibers, the UCV-fiber plane was tilted against the beam axis as shown in Fig. 4. With the tilted angle between 0 – 45°, the size of center area is large enough to cover the KOTO beam area of 100×100 mm^2. We measured the inefficiency of UCV as a function of the tilted angle to decide the angle to be used for the KOTO experiment

2.2 UCV-film

The UCV-film was made of a 0.2 mm-thick plastic scintillating film. The scintillator needs to be thin to reduce interactions of photons, neutrons, and neutral kaons with it, while still maintaining the efficiency to detect the charged kaons. However, making a scintillator thinner reduces the number of scintillation photons and increases the number of reflections on the surfaces making the attenuation length short. To increase the photon detection efficiency, we developed a new method to collect scintillation photons escaping from the thin scintillator with mirrors and PMTs. Figure 3 bottom shows a

[†] https://www.hamamatsu.com/eu/en/product/type/S13360-3075CS/index.html

[‡] Scattering of beam in the collimators makes a rare particle population region called "halo".

schematic of such a system. The mirrors were made of reflecting foils.

In this experiment we measured the photo-electron yield and the efficiency for the charged particles with the prototype. Two types of scintillators were compared. One has smooth surfaces and the other has rough surfaces. The rough surface was expected to increase the number of photons escaping from the scintillator.

§3. Experiment

Figure 4 shows the experimental setup in the GeV-γ experimental hall at ELPH. The UCV-fiber sat between a 60×50 mm^2 upstream trigger counter and 60×40 mm^2 downstream trigger counter. Two additional tagging counters were placed just upstream and downstream of the UCV-fiber to finely determine electron positions.

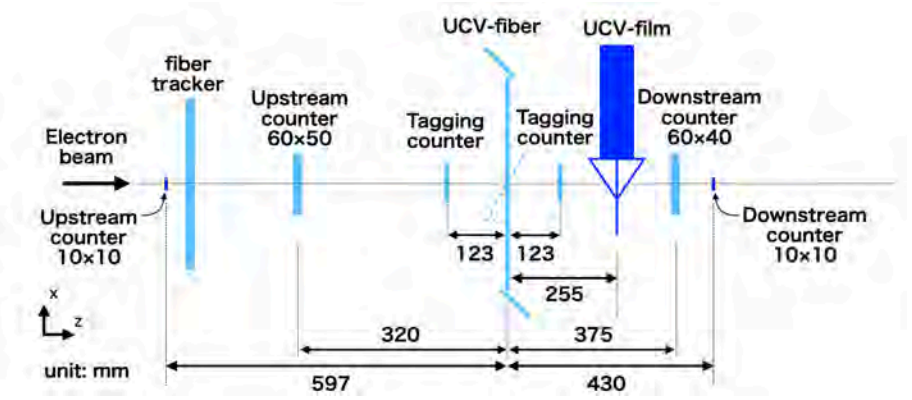

Fig.4. A schematic of the experimental setup in the GeV-γ experimental hall at ELPH: x-z view in the right hand coordinate system with the $+z$ direction defined as the downstream direction of the beam, and $+y$ direction defined as vertically up. The UCV-fiber was rotatable in x-z plane. Note that the strip direction of UCV-fiber was vertical in this setup, although it is horizontal in the KOTO detector.

The UCV-film sat upstream of the downstream 60×40 mm^2 counter. Two 10×10 mm^2 counters sat as shown in Fig. 4 to select the beam passing through the scintillator of the UCV-film. The single photon response of each channel of UCV-fiber was measured with a peak value of the distribution of ADC counts of the single-photon peak induced by an LED. The "photon yield" of each channel was defined by the peak value of ADC distribution of the beam events normalized by the single photon response. We used the 584 MeV/c electron beam to measure those. Both UCV detectors were moved to change the beam-incident position by a moving-stage system.

§4. Performance of UCV

4.1 UCV-fiber

Two main tests were done to see the performance of the UCV-fiber. The first test was an angle scan. This tested the efficiency and light yield at different tilted angles to select the optimal angle before installing it at J-PARC. The second test was a position scan. This was to confirm that the efficiency is uniform across the active area. The detection efficiency with an energy threshold was determined

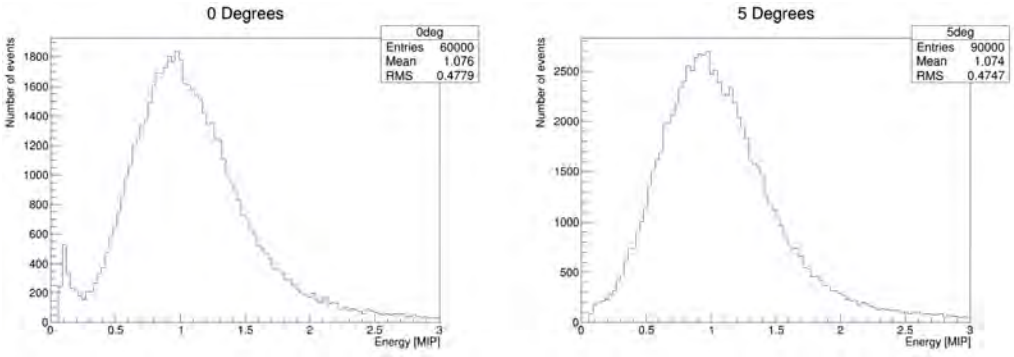

Fig.5. Deposited energy distribution with UCV-fiber at 0° (a) and 5° (b).

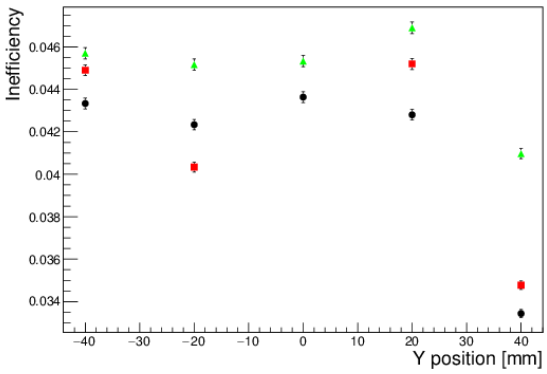

Fig.6. The inefficiency at different y positions of the UCV-fiber at x positions of -43 mm (black), 0 mm (red), and 43 mm (green).

as a ratio of events above the threshold to the total number of events selected with trigger counters. The threshold and deposited energy were measured in the units of the deposited energy of a minimum ionizing particle.

For the angle scan, the UCV-fiber was rotated to ten different angles, varying between 0° and 45° at 5 degree increments. The deposited energy distribution was calculated for each angle, as shown for 0° and 5° in Fig. 5. The peak in the distribution near zero corresponds to the particles that pass through the detector without depositing energy, such as through the cladding of the fibers. The peak height reduces as the angle increases. This follows the expectation that the majority of the effect results from the cladding of the fiber. The number of events below 0.25 MIP at 0° corresponds to (3.98±0.08)% of the total. This is consistent with the gaps due to the cladding (4% of the UCV). With the results of angle dependance of this study and simulation of real performance in the KOTO detector, we decided to set the tilted angle to 25° at J-PARC [4].

For the position scan, the x and y positions were chosen so that every point in the center region was covered within 1σ of the beam width. The variance in inefficiency among all locations was less than 1% as shown in Fig. 6.

4.2 UCV-film

In the analysis of the UCV-film, we required four coincident hits in four trigger counters including 10×10 mm^2 additional trigger counters shown in Fig 4. Figure 7 (a) shows a typical pulse of UCV-film measured with a 500-MHz waveform digitizer. The pulse width is short enough and there is no large overshoot after the pulse. Figure 7 (b) shows a distribution of peak height of pulse by the electron beam. The peak height was normalized with the peak height of a single photo-electron (p.e.). The distribution of electron events has a peak at 12.0 p.e. (12.6 p.e.) for smooth (rough) surface. The inefficiency is 10^{-2} with the 5 p.e. threshold.

Figure 7 (c) shows the inefficiency as a function of threshold for different scintillator surfaces and beam positions. There is no large difference between the smooth-surface and rough-surface scintillators. Slightly large inefficiency was observed in the case of the upper beam position compared to that of the center.

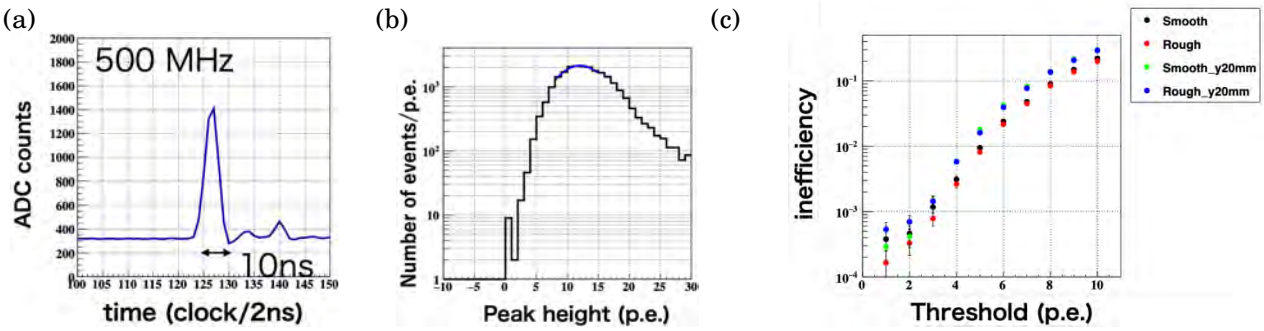

Fig.7. (a) A typical pulse of scintillation in the UCV-film. (b) Distribution of peak height of events in the case of using smooth scintillator and a beam position 25 mm from the PMT. (c) Detection inefficiency of the UCV-film is shown as a function of the threshold. Colors of dots distinguish the conditions of the scintillator surfaces and the beam height (y).

§5. Summary

We developed two types of low-mass in-beam charged particle detectors to veto charged kaons at the J-PARC KOTO experiment. The UCV-fiber was installed in the KOTO detector in December 2020 with the tilted angle of 25° based on the results of this study. The UCV-fiber has performed as expected as a real detector.

The concept of the UCV-film was confirmed that the 0.2 mm-thick scintillating film has a sufficient photon yield of 12 p.e. by collecting photons escaping from the scintillating film. We are currently developing a UCV-film type detector to be installed in the KOTO detector in 2022.

References

[1] J. Comfort *et al.*: Proposal for $K_L \to \pi^0\nu\bar{\nu}$ experiment at J-parc, 2006, https://j-parc.jp/researcher/Hadron/en/pac_0606/pdf/p14-Yamanaka.pdf.

[2] T. Yamanaka, Prog. Theor. Exp. Phys. 2012, 02B006.

[3] J. K. Ahn *et al.*: Phys. Rev. Lett. **122** (2019) 021802.

[4] T. C. Nunes: MS thesis. Osaka University, Sept. 2021.

(ELPH Experiment : #2959)

RI Production for the synthesis of Promethium Endohedral Metallofullerenes by Photon Activation Method III

K. Akiyama[1], T. Suwa[1], H. Sugiyama[1], S. Kubuki[1], and H. Kikunaga[2]

[1]*Department of Chemistry, Tokyo Metropolitan University, Hachioji, 192.0397*
[2]*Research Center for Electron Photon Science, Tohoku University, Sendai, 982-0826*

In this paprer, we reported the results of the ion pair chromatography for the analysis of $\mathbf{M_2@C_{80}}$ fullerenes containing **Pm** recovered under anaerobic conditions. The $\mathbf{La_2@C_{80}}$ employed as a simulated Pm dimetallofullerene species was found in the HPLC elution peak of peak number 3. This result suggests that the observation of the radioactivity of **Pm** at this peak is provide the proof of the stabilization for $\mathbf{PmM@C_{80}}$ type dimetallofullerene in the atmosphere by the chemical reduction.

§1. Introduction

Endohedral metallofullerenes (EMFs) are known as a clathrate compound and are attracting interest of the expectation for the potential application brought from their unique physical and chemical properties. The large number of studies about the EMFs have been reported, so far. Especially for the EMFs of lanthanide, it has been studied for a variety of encapsulated elements from the dawn of metallofullerene research. However, only metallofullerene of promethium (**Pm**) had been missing for a long time [1]. It is well known that **Pm** is one of the artificial elements belonging to lanthanide elements and do not have any naturally occurred stable isotope. The chemical property of **Pm** is considered to be almost same as those of other neighboring lanthanides, actually most stable oxidation state in water is +3 similar to neighboring element of Nd. In general, **Pm** is produced from processing nuclear fuel and neutron irradiation of **Nd** in High Flux Isotope Reactor. However, produced **Pm**, such as ^{147}**Pm**, by these methods is not suitable for the metallofullerene research because of their small gamma-ray emission rate and their long half life.

Recently, we reported the production of **Pm** EMFs using ^{143}**Pm** produced by photon activation of natural samarium and also reported that their properties such as oxidation state of **Pm** in fullerene cage and that the major species of Pm metallofullerenes were found to be $\mathbf{Pm@C_{82}}$ [2]. On the other hand, the chemical properties of the minor **Pm** metallofullerenes species, such as $\mathbf{M_2@C_{80}}$, were still unknown.

It is well known that the one of the most famous minor EMF species is $\mathbf{M_2@C_{80}}$ and that this EMF species is second major among those encapsulating light lanthanide elements [1]. However, it has been found that the chemical stability of this EMF species with neutral charge is decreased with increasing of atomic number while that for the anion species is increased [3]. Although it is impossible to discuss directly about the stability of $\mathbf{M_2@C_{80}}$ with homogeneously encapsulating two promethium atoms due to the trace amount of **Pm**, we could discuss about that of $\mathbf{M_2@C_{80}}$ with heterogeneously encapsulating Pm

and another lanthanide atom added as a carrier. In the previous report, the results of HPLC analysis of Pm EMFs produced by conventional method and the quantitative results extracted by newly developed anaerobic fullerene recovery system. In this report, we confirmed the elution behavior of chemically reduced metallofullerenes in ion pair chromatography for the analysis of $\mathbf{M_2@C_{80}}$ fullerenes containing **Pm** recovered under anaerobic conditions.

§2. Experimental

2.1 Synthesis and Extraction of Endohedral Metallofullerenes under Reduced Atmosphere

EtOH solution containing **La** with nitrate form was dropped on a porous carbon rod with 10 **mm** diameters and 60 **mm** length to be a **La**/**C** ratio with 1/50 and then dried. This porous carbon rod was placed in an electric tubular furnace and sintered at 700 ^{o}**C** under $\mathbf{N_2}$ gas flow. After the sintering, this rod was set into the fullerene generator as an anode for the arc discharge. The **Pm** EMFs were produced by the arc discharge method [2] with DC 100 **A** under 60 **kPa** of **He** atmosphere. The soot produced by above mentioned method dissolved to $\mathbf{CS_2}$ were recovered from the fullerene generator by washing the inner wall of this generator. These recovered $\mathbf{CS_2}$ solution were introduced into a glass vessel previously reported [4]. The $\mathbf{CS_2}$ in the vessel is dried in vacuo and then $\mathbf{N_2}$ gas was introduced into the vessel for replacement to $\mathbf{N_2}$ atmosphere. About 280 **mL** of tetraethylamine/acetone (1 : 3) mixed solution (here after TEA/Acetone) was injected into the vessel from branch sealed with a septum by use of a syringe. This TEA/Acetone solution was refluxed for 8 hours to extract chemically reduced anaerobic metallofullerene species. After the reflux, this solution was filtered to remove insoluble substances such as amorphous carbon. This filtrate with small amount of tetrabuthylammonium hexafluorophosphate ($TBAPF_6$) for keeping reduced state was evaporated to dryness and dissolved to 2.0 **mL** of 20 **mM** $TBAPF_6$/Acetone solution. The gamma ray emitted from these solutions were measured by a **Ge** detector for the quantitative determination.

2.2 Analysis by Ion Pair Chromatography Method

The $TBAPF_6$ solution of reduced metallofullerenes was loaded into a Buckyprep column (size: 10 **mm**ϕ $\times$ 250 **mm**) with 20 **mM** $TBAPF_6$ /Acetone solution as an eluent in order to confirm the elution components in ion pair chromatography. Each elution peak component was identified by MALDI-TOF/MS.

§3. Results and Discussion

3.1 Identification of Eluting Component for Ion Pair Chromatography

Figure 1 shows a HPLC chart of ion pair chromatography for **La** metallofullerenes. The HPLC elution peaks observed in this chromatogram are numbered 1 to 7. The observed m/z signals and identified EMF species for each elution peak are listed in the table 1. Mono-metallofullerene species, such as $\mathbf{La@C_{82}}$ and $\mathbf{La@C_{80}}$, have been detected for the peak numbers 1, 5, 6 and 7 by MALDI-TOF/MS measurement. Especially for $\mathbf{La@C_{82}}$ species, it is found that this molecule was observed in some elu-

tion peaks such as peak numbers 1, 4, 5, and 7. This result suggested that multiple **La@C**$_{82}$ structural isomer species, which are unstable in the atmosphere, are eluted stably by forming reduced compounds. On the other hand, the targeted **La**$_2$**@C**$_{80}$ fullerene was only observed at peak numbers 3 and 4. The component of the elution peak number 3 (shaded in orange) is found to be **La**$_2$**@C**$_{80}$, whereas the main component of the elution peak number 4 is mono-metallofullerene, and **La**$_2$**@C**$_{80}$ observed as one of the components is expected to be a part of the peak number 3. It is well known that the eluting position of the metallofullerene largely depends on the number of the charge transferred electrons from the encapsulated metal atom and the structure of the fullerene cage [1]. The number of the charge transferred electrons from the encapsulated **Pm** atom to the fullerene cage is expected to be 3 electrons from the results for the number of the charge transferred electrons of **Pm** mono-metallofullerene species [5]. Accordingly, the eluting position of **M**$_2$**@C**$_{80}$ fullerene encapsulating **Pm** with the same fullerene cage and the number of the charge transferred electron as **La**$_2$**@C**$_{80}$ is expected to be almost same as that of **La**$_2$**@C**$_{80}$. If the radioactivity of **Pm** is observed at the peak number 3, it is suggested that **PmM@C**$_{80}$ type dimetallofullerene could be stabilized in the atmosphere by the chemical reduction.

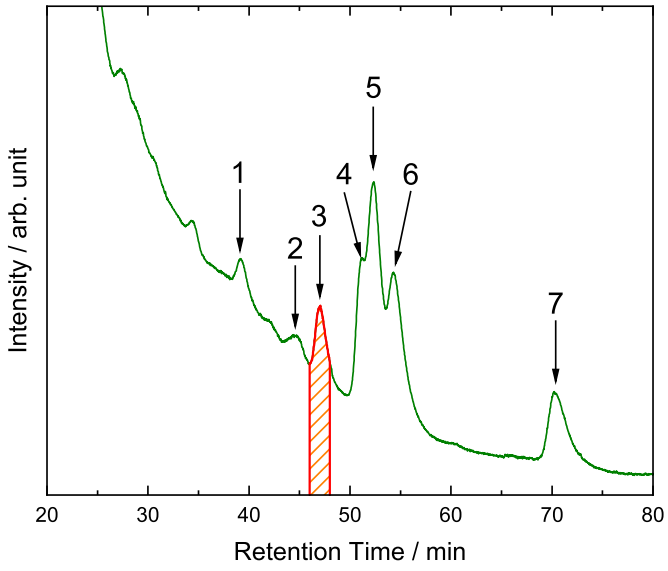

Fig.1. Ion pair chromatogram of chemically reduced La metallofullerenes

Acknowledgment

We deeply thank to the facility staffs of research center for electron photon science at Tohoku University for supplying the high-quality electron beam. And also we thank to Dr. Kyo Tsukada and Dr. Yuki Honda for helping us in the sample irradiation.

Table 1. Identified EMF species in each elution peak

Peak No.	Observed m/z	Identified EMF
1	1126	$\mathbf{LaC_{82}}$
2	–	–
3	1239	$\mathbf{La_2C_{80}}$
4	1052	$\mathbf{LaC_{76}}$
	1076	$\mathbf{LaC_{78}}$
	1100	$\mathbf{LaC_{80}}$
	1124	$\mathbf{LaC_{82}}$
	1239	$\mathbf{La_2C_{80}}$
5	1124	$\mathbf{LaC_{82}}$
6	1100	$\mathbf{LaC_{80}}$
7	1124	$\mathbf{LaC_{82}}$

References

[1] H. Shinohara: Rep. Prog. Phys. **63** (2000) 843.

[2] K. Akiyama *et al.*: ELPH Annual Rep. (2014) 135.

[3] A. Velloth *et al.*: J. Phys. Chem. C **121** (2017) 18169.

[4] K. Akiyama *et al.*: ELPH Annual Rep. (2019) 17.

[5] K. Akiyama *et al.*: ELPH Annual Rep. (2016) 72.

(ELPH Experiment : #2844, #2882, #2894, #2924)

Current status of the FOREST/BLC experiments at ELPH

T. Ishikawa[1], K. Aoki[2], H. Fujioka[3], Y. Honda[1], T. Hotta[4], K. Itahashi[5], H. Kanda[4], H. Kawai[6], K. Maeda[7], Y. Matsumura[1], M. Miyabe[1], S. Miyata[8], N. Muramatsu[1], H. Ohnishi[1], K. Ozawa[2], Y. Sada[1], H. Shimizu[1], M. Tabata[6], A.O. Tokiyasu[1], and Y. Tsuchikawa[9]

[1]*Research Center for Electron Photon Science (ELPH), Tohoku University, Sendai 982-0826, Japan*
[2]*Institute of Particle and Nuclear Studies, High Energy Accelerator Research Organization (KEK), Tsukuba 305-0801, Japan*
[3]*Department of Physics, Tokyo Institute of Technology, Tokyo 152-8551, Japan*
[4]*Research Center for Nuclear Physics (RCNP), Osaka University, Ibaraki 567-0047, Japan*
[5]*Nishina Center for Accelerator-Based Science, RIKEN, Wako 351-0198, Japan*
[6]*Department of Physics, Chiba University, Chiba 263-8522, Japan*
[7]*Department of Physics, Tohoku University, Sendai 980-8578, Japan*
[8]*Department of Physics, University of Tokyo, Tokyo 113-0033, Japan*
[9]*J-PARC Center, Japan Atomic Energy Agency (JAEA), Tokai 319-1195, Japan*

The FOREST/BLC experiments are conducted to determine low-energy S-wave ηn scattering parameters using the $\gamma d \to p\eta n$ reaction. The photon beam with energies around 940 MeV can give the recoilless condition of produced η mesons by detecting the protons at 0°. The effects of the final-state ηn interaction must be enhanced owing to the small relative momentum between the η meson and the residual neutron in this kinematics. In this year, the physics data were collected from April 9 to May 21 in 2020. In this report, a brief summary of the current status of the FOREST/BLC experiment and collected data are described.

§1. Introduction

The nucleon resonance $N(1535)S_{11}$ (N^*) is an interesting object, which can be an S-wave ηN molecule-like state and/or the chiral partner of the nucleon N. Recently, the internal structure of a hadron has been intensively discussed in terms of the compositeness X, which is an overlap with the two-body scattering state [1]. The X can be given by the two-body low-energy scattering parameters for the S-wave bound states and resonances in the threshold energy region [2]. The value of $X_{\eta N} = 0.04 + i0.37$ fm obtained from the current knowledge of the ηN-scattering amplitude suggests a three-quark state [3]. However, ηN scattering is not well known yet due to the difficulties in realizing scattering experiments because of the neutral and unstable nature of η (in general, it is difficult to obtain the low-energy scattering parameters between a neutral meson and nucleon [4]). The reliability of the deduced $X_{\eta N}$ and corresponding structure of N^* remains questionable.

The $a_{\eta N}$ values have been extracted by many theoretical analyses from the differential and total cross sections for the $\pi N \to \pi N$, $\pi N \to \eta N$, $\gamma N \to \pi N$, and $\gamma N \to \eta N$ reactions. Currently, the estimated $a_{\eta N}$ values are highly model dependent. While the values of Im$[a_{\eta N}]$ are confined into a narrow range from 0.2 to 0.3 fm, and those of Re$[a_{\eta N}]$ are scattered in a wide range from 0.2 to 1.1 fm [5]. This uncertainty comes from the fact that the existing experimental data used for extracting $a_{\eta N}$ do not enhance the effect of the ηN-scattering ($\eta N \to \eta N$) amplitude. We propose the $\gamma d \to \eta pn$ reaction to determine $a_{\eta N}$ at a certain kinematics, which enhances the ηN scattering effect.

The incident photon bombards the quasi-free proton in the deuteron and produces a virtual η meson with a very low momentum. Events are selected in which the incident energy is approximately 0.94 GeV and the proton is detected at 0°. The kinematics for these events satisfies the recoilless condition of the produced η mesons. Thus, low-energy ηn scattering is expected to take place in this condition, where the pn and ηp rescattering effects are suppressed owing to their large relative momenta ($\sim$ 0.94 GeV). The sensitivity to the Re$[a_{\eta n}]$ and Re$[r_{\eta n}]$ values are investigated and summarized in Ref. [6] by using a model based on a dynamical coupled-channel meson-baryon scattering analysis [7, 8].

§2. Experimental setup

The $\gamma d \to p\eta n$ reaction is measured at the Research Center for Electron Photon Science (ELPH), Tohoku University, Japan [9] with the FOREST electromagnetic calorimeter system [10] together with an additional forward charged-particle spectrometer called BLC [11]. The incident photon energy ranges from 0.82 to 1.26 GeV [13] for the circulating energy of 1.32 GeV in the electron synchrotron called the booster storage (BST) ring [14]. The details of the FOREST detector including the liquid deuterium target are described elsewhere [12]. The forward scattered proton is momentum-analyzed with the BLC spectrometer behind FOREST. The trajectory of a charged particle is measured with 2 planar drift chambers (DCs), and the time of flight is measured with 14 plastic scintillator (PS) hodoscopes (PSH+). An additional e/π separation is made using 10 SF5 lead-glass Cherenkov counters (LGCs). The experimental setup has been fixed since November in 2017. In this year, the physics data were collected in a period: April 9 to May 21 (2020A) in 2020.

The BLC magnet was excited every time at normal operation in this fiscal year with a coil current of 1400 A. The magnetic flux B_y at the center was monitored with a nuclear magnetic resonance (NMR) probe during the experiments, and B_y = 716.0 mT was adjusted by changing the coil current. Fig. 1 shows the magnetic flux B_y at the center for the 2020A period.

§3. Collected data

The physics data with the deuterium and hydrogen targets were collected in the 2020A period. At the starting-up stage in the 2020A period, we found that an anode wire corresponding to `Fw140` broke and high voltage could not be supplied to DC2. The beamtime started after repairing works of DC2 were completed, and noise reduction works of DCs finished. The BST ring was operated with a circulating energy of 1.32 GeV, a current of approximately 20 mA. The data collections were basically stable during

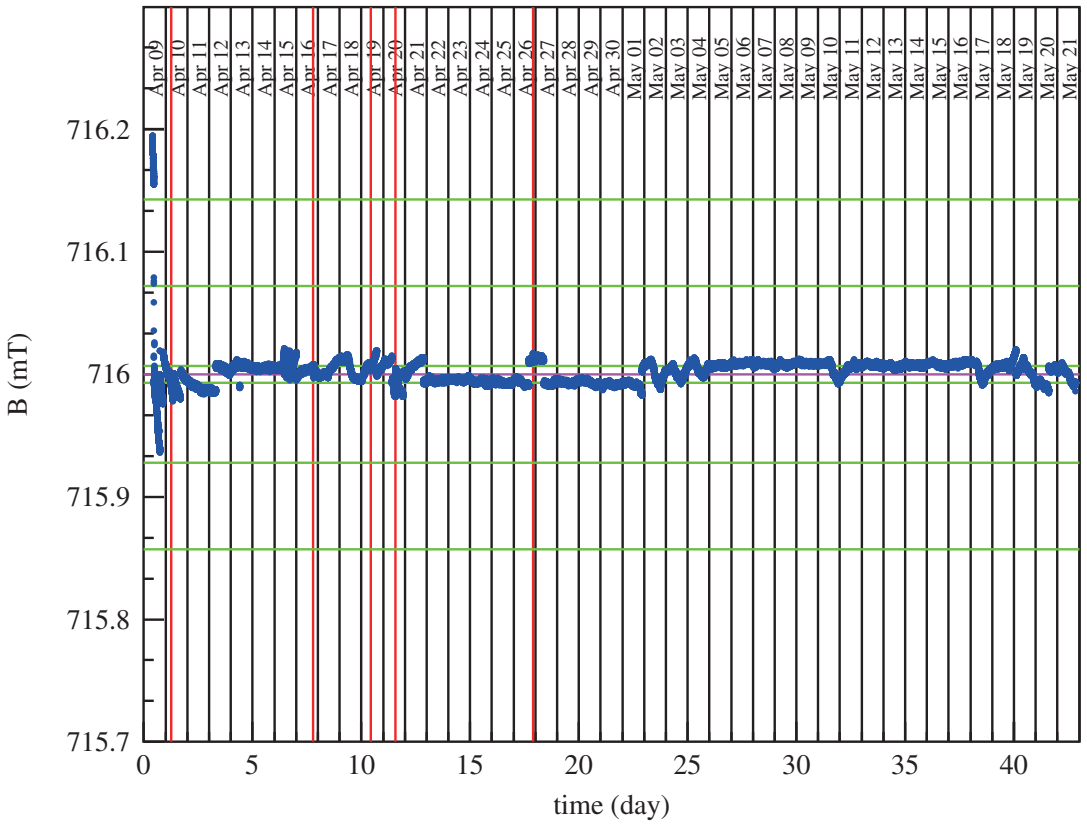

Fig.1. Long-term variation of the magnetic flux at the BLC center measured with NMR in 2020A. The horizontal axis represents the number of days from 0:00am on April 09 in 2020, and the vertical shows the magnetic flux in mT. the red vertical lines correspond to the start timings of collecting the hydrogen, empty, and deuterium targets. The horizontal green lines show the ±0.001%、±0.01%、±0.02% variation from the set value of 716.00 mT.

the period. DC power supply modules became out of order for the septum magnet on Apr 16, which was recovered on the next day. The controlling system for the modulator of the injector became out of order on Apr 19. The high-voltage supply system, CAEN SY1527, became out of order frequently after May 08. The switching hub became out of order and DAQ system halted on May 16. The beamtime terminated on May 21 owing to the abnormal stop of pure-water production equipment. Owing to the COVID-19 spread, we continued the experiment with a minimum number of shift takers. during the beamtime. Table 1 summarizes the number of spills and events of the collected data in this fiscal year (2020). The statistics for the hydrogen and deuterium data were twice and thrice higher than that for the 2009D period, respectively. The data analysis is on-going to perform the precise energy and timing calibrations of the STB-Tagger II, FOREST, and BLC detectors. The preliminary results are show in Ref. [15–18].

Acknowledgments

The authors express gratitude to the ELPH accelerator staff for stable operation of the accelerators for the FOREST/BLC experiment. They thank Dr. Kyo Tsukada for repairing DC2. They also acknowledge Mr. Ken'ichi Nanbu, and Mr. Ikuro Nagasawa for their technical assistance. This work was

Table 1. Numbers of spills and events collected in this fiscal year (2020). The circulating electron energy of the BST ring was 1.3 GeV. The targets used were liquid hydrogen, deuterium, and empty.

period	hydrogen		deuterium		empty	
	#spills	#events	#spills	#events	#spills	#events
2020A	49.30 k	921.13 M	287.47 k	2,719.53 M	11.18 k	137.56 M

supported in part by the Japan Society for the Promotion of Science (JSPS) through Grants-in-Aid for Scientific Research (B) No. 19H01902, and for Scientific Research on Innovative Areas Nos. 19H05141, 19H05181, and 21H00114.

References

[1] S. Weinberg: Phys. Rev. **137** (1965) B672.

[2] T. Hyodo: Phys. Rev. Lett. **111** (2013) 132002.

[3] T. Sekihara, T. Arai, J. Yamagata-Sekihara, S. Yasui: Phys. Rev. C **93** (2016) 035204.

[4] T. Ishikawa *et al.*: Phys. Rev. C **101** (2020) 052201 (R).

[5] Q. Haider, L.C. Liu: Int. J. Mod. Phys. E **24**, 1530009 (2015); and references therein.

[6] S.X. Nakamura, H. Kamano, T. Ishikawa: Phys. Rev. C **96** (2017) 042201 (R).

[7] A. Matsuyama, T. Sato, T.-S.H. Lee: Phys. Rep. **439** (2007) 193.

[8] H. Kamano *et al.*: Phys. Rev. C **88** (2013) 035209.

[9] H. Hama: AAPPS Bulletin **30** (2020) 41.

[10] T. Ishikawa *et al.*: Phys. Lett. B **772** (2017) 398;
T. Ishikawa *et al.*: Phys. Lett. B **789** (2019) 413;
T. Ishikawa *et al.*: PoS (Hadron2013) 095;
Y. Tsuchikawa *et al.*: JPS Conf. Proc. **17** (2017) 062007;
T. Ishikawa *et al.*: PoS (INPC2016) 267.

[11] T. Ishikawa *et al.*: Acta. Phys. Polon. B **48** (2017) 1801;
T. Ishikawa *et al.*: JPS Conf. Proc. **10** (2016) 031001;
T. Ishikawa *et al.*: JPS Conf. Proc. **13** (2017) 020031;

[12] T. Ishikawa *et al.*: Nucl. Instrum. Meth. A **832** (2016) 108.

[13] T. Ishikawa *et al.*: Nucl. Instrum. Meth. A **622** (2010) 1;
T. Ishikawa *et al.*: Nucl. Instrum. Meth. A **811** (2016) 124;
Y. Matsumura *et al.*: Nucl. Instrum. Meth. A **902** (2018) 103;
Y. Obara *et al.*: Nucl. Instrum. Meth. A **932** (2019) 108.

[14] F. Hinode *et al.*: J. Phys. Conf. Ser. **425** (2013) 072011.

[15] T. Ishikawa *et al.*: JPS Conf. Proc. **13**, 020031 (2016).

[16] T. Ishikawa *et al.*: Acta Phys. Polon. B **48**, 1801 (2017).

[17] T. Ishikawa *et al.*: Acta Phys. Polon. B **51**, 27 (2019).

[18] S. Miyata *et al.*: Proc. of Int. Conf. on Few-Body Problems in Physics, FB22 2018, Recent Progress in Few-Body Physics **238**, 705 (2020).

(ELPH Experiment : #2965)

Testing a prototype plastic scintillator hodoscope for the J-PARC E50 experiment

T. Ishikawa[1], M. Miyabe[1], H. Noumi[2,3], H. Ohnishi[1], Y. Sada[1], K. Shirotori[2], A.O. Tokiyasu[1], and C. Yoshida[1]

[1]*Research Center for Electron Photon Science (ELPH), Tohoku University, Sendai 982-0826, Japan*

[2] *Research Center for Nuclear Physics (RCNP), Osaka University, Ibaraki 567-0047, Japan*

[3]*Institute of Particle and Nuclear Studies, High Energy Accelerator Research Organization (KEK), Tsukuba 305-0801, Japan*

§1. Introduction

We plan to conduct several physics programs by using secondary particles [1–5] produced from the primary proton beam at the high-momentum beamline at the Japan Proton Accelerator Research Complex (J-PARC). Among these physics programs, the E50 experiment [1] for investigating the two-quark (diquark) correlation plays a role as a flagship. The diquark correlation has become an important ingredient to study highly excited hadrons as well as high-dense quark matter.

We plan to construct a large-acceptance general-purpose magnetic spectrometer for the E50 and other experiments (the E50 spectrometer) at the high-momentum secondary (π20) beamline. The π20 beamline provides unseparated secondary particles (positively charged π^+, K^+, and p particles, or negatively charged π^-, K^-, and $\overline{p}$ particles) with momenta up to 20 GeV/c with a momentum resolution of $\delta P/P \simeq 0.1\%$ using a dispersion-matching technique. The spectrometer consists of the large FM dipole magnet, tracking detectors [6], time-of-flight (TOF) detectors [7–9], and particle-identification detectors [10] together with a streaming data acquisition (DAQ) system [11]. We plan to use two kinds of TOF detectors in the E50 spectrometer. The first one is a restive plate chamber (RPC), which has a high time resolution $\approx$ 0.06 ns, and high magnetic-field tolerance. However, the rate tolerance is not so high, and a singles rate of RPC must be lower than 1 kHz/cm^2. An ordinary plastic-scintillator (PS) hodoscope (PSH) can be used under a high rate environment $\approx\sim$ 10 MHz/channel. The magnetic field tolerance of PSH highly depends on its photosensor. We consider that the prototype for the forward TOF detector is made up of a PS slat, Saint Gobain BC420, and a metal-packaged photomultiplier tube (PMT) is connected on each edge of the PS. In this report, shown is the time response of the prototype which has been tested using a 0.74-GeV/c positron beam [12] at the Research Center for Electron Photon Science (ELPH), Tohoku University [13].

§2. Plastic scintillators and photomultiplier tubes tested

We have tested three PS slats with a length of 1.8 m:

1. BC420 with a cross section of 30×40 mm^2,
2. BC400 with a cross section of 30×40 mm^2, and
3. BC420 with a cross section of 30×70 mm^2.

BC400 is one of the widely used PSs, and compatible with NE102, and BC420 is suitable for an ultra-fast timing measurement with a large cross section > 100 mm^2. Different sides of each cross section enable us to get information on different penetration lengths or different deposit energies of the minimum-ionizing particle (MIP).

We plan to use a single-anode metal-packaged PMT, Hamamatsu H11934. Since the cross section of this PMT is 30×30 mm^2, a close packing arrangement can be achieved for a PS slat with a cross section of 30×40 mm^2. We have tested two type of H11934: ultra-bialkali (UBA) photocathode type and super-bialkali (SBA) photocathode type. The quantum efficiencies (QEs) of UBA (H11934-200-020) and SBA (H11934-100-020) are 43% and 35%, respectively. We have also tested an ordinary 2-inch PMT, Hamamatsu H6410, which has a QE of $\approx 24\%$.

§3. Beam test

The performance study of a prototype hodoscope was carried out at the positron beamline for testing detectors at ELPH. Momentum-analyzed positrons, generated as tertiary particles from the secondary bremsstrahlung photons [14–17] from the primary circulating electrons in a synchrotron [18–20], were used as an incident beam at an momentum of 0.74 GeV/c. Two scintillating fibers with a cross section of 3×3 mm^2 were used to determine the incident position of the positrons and to generate the trigger for the data acquisition. At the most downstream. a PS block with a geometry of $30 \times 30 \times 20$ mm^3 (both sides are connected with H6410 PMTs) was placed for providing the reference timing. We used a CAMAC-based DAQ system in this beam test.

§4. Analysis

The analysis procedure was made in the following way:

1. calibration of TDC modules,
2. pulse-height time-walk (PHTW) correction for the reference counter,
3. PHTW correction for a PS slat to be tested.

Calibration of the TDC modules used were made by inserting additional 5–40-ns delays to the trigger signal. In the PHTW correction for the reference counter, we have used the events in which a positron is incident near a PMT window of a PS slat to tested and the energy deposited is higher than that expected for MIP. In the PHTW correction for a PS slat to be tested, all the coefficients of a PHTW function is common to different incident positions except for the time shift parameter depending on them.

§5. Results

The time difference distribution has a width of ≈ 0.10 ns for signals from the two PMTs connected to the reference counter suggesting a time resolution of the reference detector is ≈ 0.05 ns. BC420

with UBA for 30 mm penetration provides a time resolution of 0.06 ns in a two-edge time measurement. BC420 provides a better time resolution than BC400. UBA (SBA) provides a better time resolution than H6410. No differences of the time resolutions are observed between UBA and SBA. No differences of the time resolutions are observed between different gains.

§6. Summary

We have tested a prototype forward PSH for the E50 spectrometer using the 0.74-GeV/c positrons. We have found a BC420 slat with UBA PMTs for 30 mm penetration provides a time resolution of 0.06 ns in a two-edge time measurement. Quite high time resolutions have been obtained for the prototype. The details will be described in a forthcoming paper.

Acknowledgments

This work was supported in part by JSPS KAKENHI Grant Numbers: 19H01902, 19H05141, 19H05181, and 21H00114.

References

[1] H. Noumi *et al.*: "Charmed Baryon Spectroscopy via the (π, D^{*-}) reaction," J-PARC E50 Proposal (2012).

[2] T. Ishikawa *et al.*: "Search for an $I = 3$ dibaryon resonance," J-PARC E79 Proposal (2021).

[3] M. Naruki and K. Shirotori: "Ξ Baryon Spectroscopy with High-momentum Secondary Beam," J-PARC Letter of Intent (2014).

[4] W.C. Chang *et al.*: "Studying Generalized Parton Distributions with Exclusive Drell-Yan process at J- PARC," J-PARC Letter of Intent (2019).

[5] R. Honda *et al.*: "Measurement of the cross section of the Λp scattering," J-PARC Letter of Intent (2020).

[6] T. Aramaki *et al.*: ELPH Annual Report 2018, Tohoku University, 2019, p. 44.

[7] N. Tomida *et al.*: J. Instrum. **11**, C11037 (2016).

[8] K. Shirotori *et al.*: ELPH Annual Report 2017, Tohoku University, 2018, p. 55.

[9] T. Akaishi *et al.*: ELPH Annual Report 2018, Tohoku University, 2019, p. 58.

[10] T. Yamaga *et al.*: Nucl. Instrum. Meth. A **766**, 36 (2014).

[11] R. Honda *et al.*: Prog. Theor. Exp. Phys. **2021**, 123H01 (2021).

[12] T. Ishikawa *et al.*: Nucl. Instrum. Meth. A **694**, 348 (2012).

[13] H. Hama: AAPPS Bulletin 30 (2020) 41.

[14] T. Ishikawa *et al.*: Nucl. Instrum. Meth. A **622**, 1 (2010).

[15] T. Ishikawa *et al.*: Nucl. Instrum. Meth. A **811**, 124 (2016).

[16] Y. Matsumura *et al.*: Nucl. Instrum. Meth. A **902**, 103 (2018).

[17] Y. Obara *et al.*: Nucl. Instrum. Meth. A **922**, 108 (2019).

[18] F. Hinode *et al.*: Proc. of the 21st IEEE Particle Accelerator Conference (PAC), 2005, p. 2458.

[19] F. Hinode *et al.*: J. Phys.: Conf. Ser. 425 (2013) 072011.

[20] F. Hinode *et al.*: Proc. of the 7th International Particle Accelerator Conference (IPAC2016), 2016, p. 701.

(ELPH Experiment : #2623, #2640, #2655, #2694, #2710)

Coherent photoproduction of the neutral pion and eta meson on the deuteron (II)

T. Ishikawa[1], H. Fujimura[1*], H. Fukasawa[1], R. Hashimoto[1†], Q. He[1‡], Y. Honda[1], T. Iwata[2], S. Kaida[1], J. Kasagi[1], A. Kawano[4], S. Kuwasaki[1], K. Maeda[3], S. Masumoto[5], M. Miyabe[1], F. Miyahara[1§], K. Mochizuki[1], N. Muramatsu[1], A. Nakamura[1], K. Nawa[1], S. Ogushi[1], Y. Okada[1], K. Okamura[1], Y. Onodera[1], K. Ozawa[6], Y. Sakamoto[4], M. Sato[1], H. Shimizu[1], H. Sugai[1¶], K. Suzuki[1‖], Y. Tajima[2], S. Takahashi[1], Y. Taniguchi[1], Y. Tsuchikawa[1**], H. Yamazaki[1††], R. Yamazaki[1], and H.Y. Yoshida[2]

[1]*Research Center for Electron Photon Science (ELPH), Tohoku University, Sendai 982-0826, Japan*
[2]*Department of Physics, Yamagata University, Yamagata 990-8560, Japan*
[3]*Department of Physics, Tohoku University, Sendai 980-8578, Japan*
[4]*Department of Information Science, Tohoku Gakuin University, Sendai 981-3193, Japan*
[5]*Department of Physics, University of Tokyo, Tokyo 113-0033, Japan*
[6]*Institute of Particle and Nuclear Studies, High Energy Accelerator Research Organization (KEK), Tsukuba 305-0801, Japan*

We have experimentally studied coherent simultaneous photoproduction of the neutral pion and eta meson on the deuteron ($\gamma d \to \pi^0 \eta d$), and found a resonance-like structure in the ηd channel near the threshold. This resonance behavior would be a predicted isoscalar 1^- ηNN bound state or an ηd virtual state owing to strong ηd attraction. Details are described in a published paper [T. Ishikawa *et al.*, Phys. Rev. C **104**, L052201 (2021)].

*Present address: Department of Physics, Wakayama Medical University, Wakayama 641-8509, Japan
†Present address: Institute of Materials Structure Science (IMSS), High Energy Accelerator Research Organization (KEK), Tsukuba 305-0801, Japan
‡Present address: Department of Nuclear Science and Engineering, Nanjing University of Aeronautics and Astronautics (NUAA), Nanjing 210016, China
§Present address: Accelerator Laboratory, High Energy Accelerator Research Organization (KEK), Tsukuba 305-0801, Japan
¶Present address: Gunma University Initiative for Advanced Research (GIAR), Maebashi 371-8511, Japan
‖Present address: The Wakasa Wan Energy Research Center, Tsuruga 914-0192, Japan
**Present address: J-PARC Center, Japan Atomic Energy Agency (JAEA), Tokai 319-1195, Japan
††Present address: Radiation Science Center, High Energy Accelerator Research Organization (KEK), Tokai 319-1195, Japan

§1. Introduction

Haider and Liu predicted an exotic η-mesic nucleus five decades ago [1], in which an η meson is bound to a nucleus by the strong force alone. We have extensively searched for η-mesic nuclei to investigate the in-medium properties of the η meson [2–4] and/or the nucleon resonance $N(1535)S_{11}$ (N^*) [5–8]. The N^*, which strongly couples to ηN, is of particular interest since it is speculated to be the chiral partner of N. The N and N^* would degenerate in mass in a dense nuclear environment owing to partial restoration of chiral symmetry.

We are interested in the ηd bound state predicted by Ueda [9, 10], which is a candidate of the lightest η-mesic nucleus if it exists. Since ηd is mixed to NN^*, studying the ηd bound state also reveals the NN^* interaction. For finding the ηd bound state, we utilize coherent double neutral meson photoproduction on the deuteron, which is a good probe for studying a neutral meson and nucleus system since a sequential process is likely to take place [11, 12].

§2. Experiment

We measured the total and differential cross sections for coherent $\pi^0\eta$ photoproduction on the deuteron ($\gamma d \to \pi^0\eta d$) at incident energies ranging from 0.75 to 1.15 GeV. We used bremsstrahlung photon beams [13] produced from the 1.20-GeV circulating electrons in a synchrotron known as the STretcher Booster (STB) ring [14] at the Research Center for Electron Photon Science, Tohoku University [15]. The energy of a produced photon was determined by detecting the corresponding post-bremsstrahlung electron by a counter locate inside the BM5 magnet, STB-Tagger II [13]. The target used was liquid deuterium with a thickness of approximately 46 mm [16]. All the final-state particles in $\gamma d \to \pi^0\eta d$ were detected with the FOREST detector [17].

§3. Results

The total cross section as a function of the incident photon energy shows a rapid increasing behavior near the threshold, which is well-reproduced by the existing theoretical calculations including the final-state interactions [18, 19]. We also obtained the differential cross sections: $d\sigma/d\Omega_d$, $d\sigma/dM_{\eta d}$, and $d\sigma/dM_{\pi d}$. The $d\sigma/d\Omega_d$ shows a rather uniform distribution, suggesting a sequential process takes place in $\gamma d \to \pi^0\eta d$. The $d\sigma/dM_{\eta d}$ shows an enhancement near the ηd threshold. This enhancement is broader with increase of the incident photon energy. The $d\sigma/dM_{\pi d}$ also shows an enhancement in the high-mass region, which corresponds to the well known isovector πd resonance $\mathcal{D}_{12}$ with a mass of ≈ 2.14 GeV and a width of ≈ 0.09 GeV [11, 12, 20–28]. The appearance of this resonance is found to be the origin of the broadening of the threshold enhancement in the ηd channel.

Only the S-wave ηd system with $I = 0$ and $J^P = 1^-$ ($\mathcal{D}_{01}$) forms a peak close to the threshold in $d\sigma/dM_{\eta d}$. We decomposed the $d\sigma/dM_{\eta d}$ and $d\sigma/dM_{\pi d}$ distributions into the $\pi^0\mathcal{D}_{01}$ and $\eta\mathcal{D}_{12}$ contributions. The mass and width of $\mathcal{D}_{01}$ were found to be $2.427^{+0.013}_{-0.006}$ GeV and $\Gamma = \left(0.029^{+0.006}_{-0.029}\right)$ GeV + $\left(0.00^{+0.41}_{-0.00}\right) pc$ in a Flatt'e parameterization [29, 30], where p_η denotes the η momentum in the ηd-CM frame. The $\mathcal{D}_{01}$ would be the predicted ηd bound state [9, 10], or an ηd virtual state [31–33]. originating

from strong ηd attraction.

§4. Summary

We have measured the total and differential cross sections of $\gamma d \to \pi^0 \eta d$ at incident energies ranging from 0.75 to 1.15 GeV. We have found a resonance-like structure in the ηd channel near the threshold. This resonance behavior would be a predicted isoscalar 1^- ηNN bound state or an ηd virtual state owing to strong ηd attraction. Detailed analyses and discussions are described in Ref. [34].

Acknowledgments

This work was supported in part by JSPS KAKENHI Grant Numbers: 19002003, 17340063, 24244022, 26400287, 16H02188, 19H01902, 19H05141, 19H05181, and 21H00114.

References

[1] Q. Haider, and L.C. Liu: Phys. Lett. B **172**, 257 (1986).
[2] S.D. Bass, and A.W. Thomas: Phys. Lett. B **634**, 368 (2006).
[3] S. Hirenzaki, and H. Nagahiro: Acta Phys. Polon. B **45**, 619 (2014).
[4] S.D. Bass, and P. Moskal: Rev. Mod. Phys. **91**, 015003 (2019).
[5] D. Jido, H. Nagahiro, and S. Hirenzaki: Phys. Rev. C **66**, 045202 (2002).
[6] H. Nagahiro, D. Jido, and S. Hirenzaki: Phys. Rev. C **68**, 035205 (2003).
[7] H. Nagahiro, D. Jido, and S. Hirenzaki: Nucl. Phys. A **761**, 92 (2005).
[8] D. Jido, E.E. Kolomeitsev, H. Nagahiro, and S. Hirenzaki: Nucl. Phys. A **811**, 158 (2008).
[9] T. Ueda: Phys. Rev. Lett. **66**, 297 (1991).
[10] T. Ueda: Phys. Lett. B **291**, 228 (1992).
[11] T. Ishikawa *et al.*: Phys. Lett. B **772**, 398 (2017).
[12] T. Ishikawa *et al.*: Phys. Lett. B **789**, 413 (2019).
[13] T. Ishikawa *et al.*: Nucl. Instrum. Meth. A **622**, 1 (2010).
[14] F. Hinode *et al.*: in Proceedings of 21st IEEE Particle Accelerator Conference (PAC) (IEEE, Piscataway, 2005), pp. 2458–2460.
[15] H. Hama: AAPPS Bulletin **30**, 41 (2020).
[16] H. Yamazaki *et al.*: ELPH Annual report **2011–2013**, Tohoku University, 2014, p. 126.
[17] T. Ishikawa *et al.*: Nucl. Instrum. Meth. A **832**, 108 (2016).
[18] M. Egorov, and A. Fix: Phys. Rev. C **88**, 054611 (2013).
[19] M. Egorov: Phys. Rev. C **101**, 065205 (2020).
[20] B.S. Neganov and L.B. Parfenov, J. Exp. Theor. Phys. **7**, 528 (1958).
[21] R.A. Arndt, I.I. Strakovsky, and R.L. Workman: Phys. Rev. C **50**, 1796 (1994).
[22] R.A. Arndt, I.I. Strakovsky, R.L. Workman, and D.V. Bugg: Phys. Rev. C **48**, 1926 (1993).
[23] C.H. Oh, R.A. Arndt, I.I. Strakovsky, and R.L. Workman: Phys. Rev. C **56**, 635 (1997).

[24] N. Hoshizaki: Phys. Rev. C **45**, R1424 (1992).

[25] N. Hoshizaki: Prog. Theor. Phys. **89**, 251 (1992).

[26] N. Hoshizaki: Prog. Theor. Phys. **89**, 563 (1992).

[27] N. Hoshizaki, Prog. Theor. Phys. **89**, 569 (1992).

[28] M.N. Platonova and V.I. Kukulin: Phys. Rev. C **94**, 054039 (2016).

[29] S.M. Flatté: Phys. Lett. B **63**, 224 (1976).

[30] Yu. S. Kalashnikova, and A.V. Nefedirev: Phys. Rev. D **80**, 074004 (2009).

[31] S. Wycech and A.M. Green, Phys. Rev. C **64**, 045206 (2001).

[32] A. Fix and H. Arenhövel, Eur. Phys. J. A **9**, 119 (2000).

[33] H. Garcilazo, Phys. Rev. C **67**, 067001 (2003).

[34] T. Ishikawa *et al.*, Phys. Rev. C **104**, L052201 (2021).

(ELPH Experiment : #2973)

First commissioning of the ULQ2 experiment at ELPH

Y. Honda[1], C. Legris[1], T. Goke[1], H. Kikunaga[1], Y. Maeda[2], S. Miura[1], M. Miyabe[1], T. Muto[1], K. Nanbu[1], T. Suda[1], K. Takahashi[1], D. Taki[1], T. Tamae[1], A. O. Tokiyasu[1], K. Tsukada[3], H. Wauke[1], and Z. Hang[2]

[1]*Research Center for Electron Photon Science (ELPH), Tohoku University, Sendai, 982-0826, Japan*
[2]*Faculty of Engineering, University of Miyazaki, Miyazaki, 889-2192, Japan*
[3]*Institute for Chemical Research, Kyoto University, Uji, 611-0011, Japan*

The ULQ2 experiment is aiming to determine the proton charge radius with low-energy electron scattering. In FY2020, first beam for the ULQ2 beam line was provided and performance of the spectrometer was studied. The results confirmed that the optical properties of the spectrometer are in good agreement with the design, and the spectrometer has an enough momentum resolution to accomplish the ULQ2 experiment.

§1. Introduction

Proton charge radius has a serious inconsistency since 2010. The CODATA2010 [1] summarized the proton charge radius as 0.8775(51) fm from electron scattering and hydrogen spectroscopy experiments. However, a 4%(7σ) smaller radius of 0.84184(67) fm was reported in 2010 from a muonic hydrogen spectroscopy experiment [2]. That is called proton radius puzzle. After the 2010, the radius has been newly measured with hydrogen spectroscopy and electron scattering, but the results are divided into around 0.84 and 0.88 fm [3–6]. There are no consensus about the inconsistency and the puzzle is getting more confused.

ULQ2 (Ultra Low Q^2) experiment at ELPH is aiming at determining the proton radius with the electron scattering. The features of the ULQ2 experiment are as follows : absolute cross section measurement with high accuracy of 10^{-3}, measurement at low momentum transfer region of $0.0003 \leq Q^2 \leq 0.008$ (GeV/c)^2 with beam energies of 10 - 60 MeV, and experimental separation of charge and magnetic form factor (Rosenbluth separation). In this report, we report about first commissioning of the ULQ2 experiment.

§2. Commissioning

2.1 Setup

Picture of the ULQ2 beam line and first spectromter are shown in the figure 2(top). The beam line got an allowance to provide the beam on September 7th, 2020, and produced first beam on September 11st, 2020. After several study, typical value of the size and momentum spread of the 50 MeV beam

were 0.6 mm on the target and 0.6×10^{-3}. These values are significantly better than the target values of 1 mm and 1×10^{-3}, respectively.

Focal plane detector of the spectrometer and lead block shield are shown in the figure 2(bottom). Two single-sided sillicon strip detector (SSSD) are adoupted as the focal plane detector. The SSSD, named g-2 test module2, have been developed for the J-PARC muon g − 2/EDM experiment [7]. In the ULQ2 experiment, the SSSD are used in layers, with the first layer (bottom) measureing the momentum and second layer (top) measuring the scattering angle from the hit position. At first, no shield were placed, but the elastic scattering peaks could not be observed due to the enormous background, then the shielding was gradually strengthened. Finnaly, as shown in the figure, all directions were shielded with 50-100 mm lead block (the front shield was removed for taking photo).

Fig.1. Picture of the ULQ2 beam line and spectrometer (top) and focal plane detector and lead shield at the top of the spectrometer (bottom).

2.2 Result

Figure 2 shows momentum spectrum of the scattered electrons from CH2 target. Beam energy, current and angle of the spectromter are 50 MeV, 19 nC/pulse and 90°, respectively. e+C elastic scattering peak is clearly observed around $p = 50$ MeV/c, and e+H elastic scattering peak is also observed around $p = 47.5$ MeV/c. Th spectrum of the figure 2 is obtained by subtracting background (magnetic field of the spectromter was off) from foreground. Before the subtraction, there was a large background of about 2000 counts/bin overall. That is about 10 times larger than the e+H peak height. The background must be reduced by adding more shield, studying background source and so on.

Momentum resolution was estimated as $5.6(2) \times 10^{-4}$ from the elastic peak width. It is in good agreement with the simulated one of 5.1×10^{-4}. It has an enough power to distinguish the e+H and e+C peak at minimum momentum transfer where the momentum difference of these peak is 7.4×10^{-3}.

Momentum dispersion $(x|\delta)$ (relationship between beam momentum and x hit position on the detector) and $(x|x)$ (relationship between beam x position on the target and x hit position on the detector) were measured. The $(x|\delta)$ was measured by varying the magnetic field of the spectromter instead of changing the beam momentum. Increasing the magnetic field is equivalent to reducting the beam momentum, and vice versa. We obtained $(x|\delta) = 855.7(1.1)$ mm and $(x|x) = -0.514(9)$, these are consistent with the simulated values of 854.9 mm and -0.530.

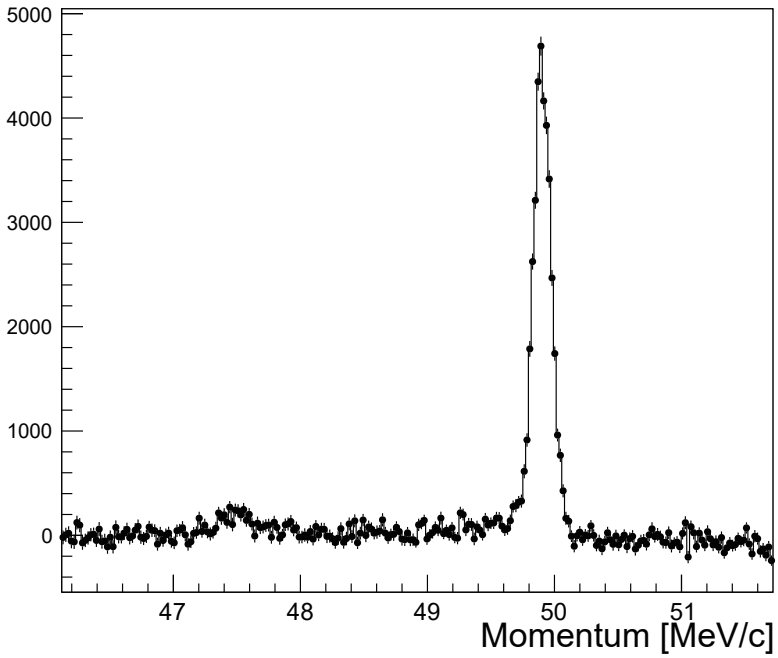

Fig.2. Momentum spectrum of scattered electron from the CH2 taget. Beam energy, beam current and scattering angle are 50 MeV, 19 nC/pulse and 90°. e+C elastic scattering peak is clearly observed around $p = 50$ MeV/c, and e+H elastic scattering peak is also observed around $p = 47.5$ MeV/c.

§3. Prospect

In this commissioning, we confirmed that optical properties $(x|\delta)$ and $(x|x)$ are in good agreement with the design and the spectrometer has an enough momentum resolution. On the other hand, we failed to measure optical properties such as $(y|\theta)$ and $(y|\theta\delta)$ due to the large background. These are important parameter related to scattering angle, and must be remeasured after background reduction. In addtion, we observed serious electric noise synchronizing with the beam. Due to the noise, we had to choose the data carefully by timing to remove the noise. Elimination of electrical noise is an urgent priority, and a noise study will be conducted in the spring 2021. Second spectrometer for luminosity monitor will be constructed in summar 2021, and commissioning of the twin spectrometer will be conducted in winter 2021. After the commissionings, we will start physics run from FY2022.

References

[1] P. J. Mohr, B. N. Taylor, and D. B. Newell, Rev. Mod. Phys., vol. 84, no. 4, pp. 1527–1605, Nov. 2012.

[2] R. Pohl et al., Nature, vol. 466, no. 7303, pp. 213–216, 2010.

[3] A. Grinin et al., Science (80-.)., vol. 370, no. November 3, pp. 1061–1066, 2020.

[4] W. Xiong et al., Nature, vol. 575, no. June, pp. 147–151, 2019.

[5] H. Fleurbaey et al., Phys. Rev. Lett., vol. 183001, pp. 1–5, 2018.

[6] N. Kolachevsky et al., AIP Conf. Proc., vol. 1936, 2018.

[7] T. Aoyagi et al 2020 JINST 15 P04027

(ELPH Experiment : #2947)

Production of Sc-46 and Sc-47 tracers by photonuclear reactions

Hidetoshi KIKUNAGA[1]

[1]*Research Center for Electron Photon Science, Tohoku University, Sendai, 982-0826*

Scandium-46 and Scandium-47 are nuclides useful or expected to be useful in various fields such as radiotherapy and basic research. It is important to produce these nuclides separately depending on the application. In this work, the radioactivity ratios of ^{46}Sc and ^{47}Sc produced by photonuclear reactions from ^{nat}Ti and ^{48}Ti targets have been determined. $^{nat}TiO_2$ and $^{48}TiO_2$ were enclosed in a quartz tube for bremsstrahlung radiation. The irradiations were performed using the electron linear accelerator at Tohoku University. The accelerator was operated at an electron energy of 20-50 MeV. The TiO_2 targets were placed in close contact with the back of a Ta converter and cooled with running tap water during the 10-30 min irradiation. After irradiation, the targets were examined by gamma spectrometry using a high-purity Ge semiconductor detector.

§1. Introduction

The scandium isotope with mass number 47 (^{47}Sc) has a suitable half-life ($T_{1/2}$: 3.35 d), a relatively low maximum energy of β-rays (E_β = 440 keV (68%) and 600 keV (32%)), and a γ-ray emission characteristic suitable for SPECT imaging (E_γ = 159 keV (68%)), so it is expected to be used in nuclear theranostics. Because ^{46}Sc has a long half-life ($T_{1/2}$: 84 d) and a simple γ-ray emission characteristic (E_γ = 889 keV(99.98%), 1121 keV(99.99%)) to which the sum peak method can be applied, it is used for standard sources, basic research, education, etc.

Depending on the application, it is important to be able to produce these nuclides selectively. In particular, when producing ^{47}Sc for nuclear medicine purposes, it is better to have as little ^{46}Sc as possible. ^{47}Sc can be produced using various methods such as neutron irradiation and proton irradiation [1]. One of the reaction pathways with the fewest impurities is the production method that goes via ^{47}Ca ($T_{1/2}$: 4.5 d, the parent nuclide of ^{47}Sc). However, this route requires expensive targets such as ^{48}Ca(γ,n)^{47}Ca and ^{46}Ca(n,γ)^{47}Ca. In this study, we report on the production of^{47}Sc and ^{46}Sc tracers using relatively inexpensive ^{nat}Ti and ^{48}Ti.

§2. Experimental

Approximately 1 g of $^{nat}TiO_2$ was formed into a cylindrical shape with a diameter of 10 mm and sealed in a quartz tube, which was used as the ^{nat}Ti irradiation sample. Approximately 10 mg of $^{48}TiO_2$

with an enrichment of 99.6% was sealed in a quartz tube and used as the ^{48}Ti irradiation sample. The electron beam accelerated to 20-50 MeV by the high-intensity electron LINAC at the Research Center for Electron Photon Science, Tohoku University, and was converted to bremsstrahlung by a water-cooled converter using 3 mm thick Ta. Each sample was irradiated for 10-30 min with water cooling. The irradiated targets were subjected to γspectrometry with a high-purity Ge semiconductor detector.

§3. Results

From the ^{46}Sc/^{47}Sc radioactivity ratios at the end of irradiation obtained in the ^{nat}Ti experiment, it found observed that the ^{46}Sc/^{47}Sc radioactivity ratio is minimized near the threshold of the ^{46}Ti(γ,pn)^{46}Sc reaction, and the ^{46}Sc radioactivity becomes less than 1% of the ^{47}Sc. On the other hand, when enriched ^{48}Ti is used, the ^{46}Sc content increases with increasing energy due to the ^{48}Ti(γ,pn) reaction. These data can be used as a reference for producing ^{47}Sc that contains as little ^{46}Sc as possible, for example for nuclear medicine applications.

References

[1] D.A. Rotsch *et al.*, Appl. Radiat. Isot. 131 (2018) 77 and refs. therein.

II. Status Report

Status of Accelerator Facilities in FY2020

F. Hinode, K. Kanomata, S. Kashiwagi, S. Miura, T. Muto, I. Nagasawa,
K. Nanbu, K. Shibata, K. Takahashi, and H. Hama

Accelerator group in ELPH, Tohoku University, Sendai, 982-0826

The total operation time of the electron accelerator complex of the high-intensity 60 MeV linac, 90 MeV injector linac, and 1.3 GeV BST (booster storage ring) in FY2020 exceeded 2000 h, including the operation of the test accelerator t-ACTS. At the beginning of FY2020, the machine time for external users was cancelled owing to the emergency declaration of COVID-19, and operation for internal users was conducted. Thereafter, under the regulation according to the BCP level by the university headquarters, the operation for user machine time was continued by the minimum number of operating personnel necessary, with due consideration given to infection prevention. In past years, operation during the summer season, when the cooling system is subjected to heavy loads, has been avoided. This year, however, the operation period was postponed due to vacuum trouble caused by a high-intensity linac; therefore, the operation was scheduled for all weekdays in July.

§1. High intensity linac

Electron beams from the high-intensity linac were supplied in the energy range of 10-60 MeV, depending on the requirements of the individual machine users. In FY 2018, the maximum beam output of the high-intensity linac increased from 6 kW to 9 kW by upgrading the thermionic electron gun and beam irradiation system. In addition to the aging of linac components, the increase in beam output has caused problems such as malfunctions and failures of control equipment due to high radiation doses and vacuum leaks due to high-intensity beams. Therefore, we are steadily proceeding with the replacement of aging equipment and radiation countermeasures, beginning with those that can be addressed. The vacuum leak that occurred at the titanium window for beam extraction was thought to be caused by water contamination in the helium cooling line. Therefore, a dew point meter was installed to monitor the water content in the helium line for window cooling. In addition, the flow switch of the cooling system was doubled to ensure that the interlock functioned, even in a high-radiation environment. Furthermore, the beam size was monitored using a beam screen with a hole to prevent local overloading of the heat load on the titanium window.

With the installation of a new beamline for the electron scattering experiments (ULQ2) in Exp. Hall #1, the operation mode was added to the high-intensity linac. Beam tuning, which started after the radiation modification application was approved in September, is progressing well, and user testing of the detector system is now underway.

§2. Injector linac

The operation of injector linac was performed without any significant troubles. However, the discharge phenomenon that frequently occurs in thermionic RF gun is on the increase, and the cathode is replaced approximately once a year as a countermeasure. Modifications to the RF waveguide circuit to suppress the discharge are currently being considered.

§3. BST ring

1.3 GeV BST ring has well operated to generate high energy gamma rays via bremsstrahlung from internal target wire inserted to the electron beam orbit. Despite the controlled situation under the COVID-19 emergency declaration, the BST ring exceeded 1,240 h of operation in FY2020.

§4. Reducing power consumption by inverter driving of primary cooling water pump

Until now, the pump in the cooling tower system has always operated at a rated capacity, even when the accelerator is in standby mode, resulting in wasteful standby power consumption. Therefore, an inverter circuit was introduced to control the pump speed, and the pump was operated at a capacity appropriate for the heat load, thereby reducing power consumption. The photographs below show the newly installed pump and the inverter circuit. With this improvement, power consumption was significantly reduced to approximately 20% of the rated operation.

Fig.1. (left) newly installed pump, (right) inverter circuit

User Support Office Report in FY2020

M. Miyabe[1] and The user support office[1]

[1]*Research Center for Electron Photon Science, Tohoku University, Sendai, 982-0826, Japan*

The User Support Office coordinate across the users and our facility for management of the beamtime. In 2020 financial year, we had provided the electron, photon and positron beam. Under the influence of the new coronavirus infection, we could not provide the beam as planned at the beginning of the fiscal year. After June, we carried out the planned schedule of beamtime. We had a few small troubles at 70 MeV linac, but no other big problems occurred. [1, 2].

§1. Introduction

ELPH has three accelerators for Joint Usage/Research. Our facility could provide several beams with following three beam lines,

- 70 MeV electron linear accelerator (linac) at the first irradiation lab (For Radiochemistry, **BEAM LINE I**)
- Tagged photon beam from 1.3 GeV electron synchrotron called BST ring with 90 MeV injector at the second irradiation lab (For Hadron Physics, **BEAM LINE II, Photon beamline I**)
- Tagged photon beam at the GeV-γ irradiation room (For Hadron Physics, **BEAM LINE III, Photon beamline II**)

In addition, positron/electron beam line for testing detectors is located at the GeV-γ irradiation room. The 70 MeV electron linear accelerator was utilized for the Radiochemistry experiments by photonuclear reactions. It could produce radio active source with its high intensity. Both tagged photon beam line was used for Hadron physics experiments. NKS2 and FOREST/BLC experiment have bean held in recent years.

§2. Beamtime operated

The total radiation time was 431 hours for the RI linac operation and 1243 hours for the BST operation, and it was 1673 hours in total. Table 1 summarizes the radiation times, and user beam times in fiscal.

Many experiments for testing detectors were made by positron beam line. Positron beam was produced by bremsstrahlung photon beams from the synchrotron. Total 21 shifts experiments are performed using this positron beam in this financial year.

A Next generation FOREST experiments (FOREST/BLC) was started by GeV-γ group in ELPH. New bending magnet was installed on the downstream of FOREST detectors and it covers the most

forward angle. These new experimental setup enable the zero degree proton detection for the $\gamma d \to p\eta n$ reaction at $E_\gamma \sim 0.9$ GeV. This reaction gives the zero relative momentum between the η and n. This situation will enable to determine the ηn scattering length. In this financial year, physical data was taken with hydrogen and deuteron target. Total 90 shifts of FOREST/BLC experiment(#2924) were carried out.

One experiment was carried out for the undergraduate students. This experiment (#2942: H. Ohnishi, ELPH, Tohoku University) is for the education of the undergraduate students in ELPH [3].

Table 1. Radiation times, and user beamtimes in financial year 2020. They are given by the sum of the times that the beam is coming to the beamline, and that the beam is provided to the users.

Month	RI Linuac radiation (h)	BST Ring radiation (h)
April	14	518
May	0	495
Jun	48	0
July	53	53
August	0	0
September	59	0
October	63	25
November	55	35
December	30	0
January	34	0
February	37	53
March	38	64
Sum	431	1243

§3. ELPH workshops and ELPH seminars

In this fiscal year, ELPH supported four ELPH workshops. the first one is ”SNP school 2020 [4]” (C026: S. N. Nakamura, Tohoku University). The second one is Radiochemistry workshop ”2020 重元素核化学ワークショップ” (C027: H. Haba, Riken). The third one is nuclear physics workshop ”電子散乱による不安定核研究の進展と展望” (C028: K. Tsukada, Kyoto University). The fourth one is hadron physics workshop ”様々なフレーバー領域で探るクォーク・ハドロン多体系の分光と構造” (C029: T. Sekihara, Kyoto Prefectural University). Additionally, 14 ELPH seminars were held in this fiscal year. Seminars title and talker are listed below.

- 依田 哲彦, 大阪大学核物理研究センター, ”RCNP 加速器制御系更新と EPICS の部分的導入”
- 川畑 貴裕, 大阪大学, ”原子核におけるクラスター相関と宇宙における元素合成過程”
- Magdalena Skurzok, Istituto Nazionale di Fisica Nucleare, Italy, ”Search for eta-mesic nuclei with WASA-at-COSY facility（オンライン）”
- 菅野 智則, 東北大学 埋蔵文化財調査室, ”青葉山丘陵南辺部の遺跡群 －芦ノ口遺跡とその周辺－”
- 坂上 和之, 東京大学工学系研究科光量子科学研究センター, ”加速器研究におけるレーザーシステム開発（光陰極とレーザーコンプトンを中心に）”
- ”セキュリティ講習会（学内限定、オンライン）”

- 塚田 暁, 東北大学電子光理学研究センター, ”SCRIT 法を用いた電子・不安定核散乱実験の現状と展望（オンライン）”
- 前田 幸重, 宮崎大学工学教育研究部工学基礎教育センター, ”少数核子系散乱実験による核力の三体力効果の研究”
- 羽島 良一, 量子科学技術研究開発機構, ”レーザー・コンプトン散乱ガンマ線、基礎と応用の間で”
- 黒田 直史, 東京大学大学院総合文化研究科広域科学専攻 相関基礎科学系, ”反水素原子ビーム分光による基礎物理研究”
- M. Cargnelutti, Instrumentation technologie Slovenia, ”An overview of beam diagnostics and read-out electronics for particle accelerators”
- Vladimir Dubinko, National Science Centre Kharkov Institute of Physics & Technology, ”Nuclear Fusion of Hydrogen Isotopes Induced by the Localized Anharmonic Vibrations”
- Tadeusz LESIAK, Institute of Nuclear Physics of the Polish Academy of Sciences, ”QCD aspects at future e+e- colliders at the energy frontier”
- Tomasz SKWARNICKI, College of Arts and Sciences at Syracuse University, ”Exotic Baryons”

References

[1] Beam time schedule 2020A < https://www.lns.tohoku.ac.jp/archives/3846/ >

[2] Beam time schedule 2020B < https://www.lns.tohoku.ac.jp/archives/4172/ >

[3] Approved proposvals < https://www.lns.tohoku.ac.jp/users/saitaku/ >

[4] SNP School 2020 < https://lambda.phys.tohoku.ac.jp/snpsc2020/ >

Radiation Safety Report 2020

Radiatn Safety Office

放射線安全管理室より 2020 年度（令和 2 年 4 月～令和 3 年 3 月）の報告を以下の通り行う。

§1. 許認可申請

令和 2 年 5 月 12 日　　承認使用に係る変更承認申請書の提出
令和元年 9 月 7 日　　変更の承認

§2. 個人管理

2.1 放射線業務従事者登録

175人（ 東北大 75人　学外 88人　研究者以外 12人）

2.2 個人被ばく管理

1年間の個人被ばく線量　　5 mSv 以下　175人

2.3 教育訓練

定期 再教育（Web 講習）令和2 年6 月11 日～ 30 日 77 人
不定期 登録前講習（新規教育） 36回 78 人
登録前講習（Web 講習） 10 回 25 人
区域教育のみ 6回 16 人

§3. 自主点検

自主点検 年2回実施 令和2年9月20日、令和3年3月9日

§4. 放射性同位元素製造記録

2020 年度に本加速器施設で製造され，共同研究に使用された放射性同位元素は次のとおり。

核種	数量（kBq）
Ac-225	2
Ag-105	4,000
As-74	100
Au-196	4,600

核種	数量（kBq）
K-42	80,502.38
K-43	249,796.62
Mn-54	1,005
Na-22	865

Ba-133m	4	Ni-57	2,700
Ba-135m	450	Pd-103	20
C-11	1,000	Pm-143	200
Cd-115	80,000	Pt-195m	40
Ce-141	5	Ra-225	201
Co-57	12	Sc-46	11,100
Cr-48	4,000	Sc-47	280,000
Cs-132	400	Sr-85	100
Cs-136	5,020	Tl-202	900,000
Cu-61	10	V-48	7,010
Ga-68	50	Y-88	100
Hg-203	900		

全 31 核種　計 1,634,192.52 kBq

§5. その他

菊永、武藤、石川が主任者定期講習を受講した。

III. List of Publication

List of Publication (論文リスト) (2020)

Papers Published in Refereed Journals

ELPH, Towards Scientific Research Core Based on Electron Accelerators

Hiroyuki Hama

Association of Asia Pacific Physical Societies (AAPPS) Bulletin, Vol. 30 No. 2, p.p. 41-45, (2020).

Toward Superconducting Electron Accelerators for Various Applications

Hiroyuki Hama and Sadao Miura

Phys. Status Solidi, A 2021, 218, 2000294 (2020).

Demonstration of variable polarized coherent terahertz source,

Shigeru Kashiwagi, Hirotoshi Saito, Fujio Hinode, Yuto Ishizuki, Ken Kanomata, Sadao Miura, Nozomu Morita, Toshiya Muto, Ikurou Nagasawa, Ken-ichi Nanbu, Koutaro Shibata, Ken Takahashi, Kento Terada, Hiroki Yamada, Hiroyuki Hama Heishun Zen, Akinori Irizawa, Infrared Physics & Technology, 106, 103274 (2020).

Design and testing of a W-MoO3target system for electron linac production of 99Mo/99mTc

Jaewoong Jang, Hidetoshi Kikunaga, Shun Sekimoto, Makoto Inagaki, Tomohiko Kawakami, Tsutomu Ohtsuki, Shigeru Kashiwagi, Ken Takahashi, Kyo Tsukada, Katsuyoshi Tatenuma, Mitsuru Uesaka

Nucl. Instrum. Methods Phys. Res. A, 987 (2021) 164815

Electron Scattering for Exotic Nuclei"

T. Suda

J of Physics, 1643(2020) 012159.

The mean square radius of the neutron distribution and the skin thickness derived from electron scattering

Haruki Kurasawa, Toshimi Suda and Toshio Suzuki

Prog. Theoretical and Experimental Physics, 2021, 013D02 (40 pages).

Position tracking detector for J-PARC muon g-2/EDM experiment

T. Yamanaka, T. Aoyagi, H. Ikeda, M.Ikeno, T.Ito, K.Ueno,, T.Uchida, K.Kawagoe, T.Kishishita, T.Kume, T.Kohriki, N.Saito, O.Sasaki, T.Sata, N.Sato, Y.Sato, M.Shoji, S.Shirabe, T.Suehara, Y.Sue, T.Suda, H.Sendai, T.Takatomi, M.Tanaka, K.Tsukada, Y.Tsutsumi, J.Tojo, K.Namba, S.Nishimura, Y.Honda, M.Matama, T. Mibe, T. Murakami, H. Yasuda, T. Yoshioka
Nuclear Instruments and Methods in Physics A958 (2020) 162786

Performance evaluation of a silicon strip detector for positrons/electrons from a pulsed a muon beam.
T. Aoyagi, Y. Honda, H. Ikeda, M. Ikeno, K. Kawagoe, T. Kohriki, T. Kume, T. Mibe, K. Namba, S. Nishimura, N. Saito, O. Sasaki, N. Sato, Y. Sato, H. Sendai, K. Shimomura, S. Shirabe, M. Shoji, T. Suda, T. Suehara, T. Takatomi, M. Tanaka, J. Tojo, K. Tsukada, T. Uchida, T. Ushizawa, H. Wauke, T. Yamanaka, and T. Yoshioka
Journal of Instrumentation 15 (2020) P04027.

Co-precipitation behaviour of single atoms of rutherfordium in basic solutions
Y. Kasamatsu, K. Toyomura, H. Haba, T. Yokokita, Y. Shigekawa, A. Kino, Y. Yasuda,
Y. Komori, J. Kanaya, M. Huang, M. Murakami, H. Kikunaga, E. Watanabe, T. Yoshimura, K. Morita, T. Mitsugashira, K. Takamiya, T. Ohtsuki, A. Shinohara
Nature Chemistry, 13 (2021) 226-230

**Production of ^{266}Bh in the ^{248}Cm(^{23}Na,5n)^{266}Bh reaction and its decay properties*
H. Haba, F. Fan, D. Kaji, Y. Kasamatsu, H. Kikunaga, Y. Komori, N. Kondo, H. Kudo, K. Morimoto, K. Morita, M. Murakami, K. Nishio, J. P. Omtvedt, K. Ooe, Z. Qin, D. Sato,
N. Sato, T. K. Sato, Y. Shigekawa, and A. Shinohara
Physical Review C. 102 (2020) 024625/1-12

Optimized TES Microcalorimeters with 14 eV Energy Resolution at 30 keV for gamma-Ray Measurements of the Th-229 Isomer
H. Muramatsu, T. Hayashi, N. Yuasa, R. Konno, A. Yamaguchi, K. Mitsuda, N. Y. Yamasaki, K. Maehata, H. Kikunaga, M. Takimoto, K. Nakamura
Journal of Low Temperature Physics volume 200 (2020) 452-460

**Formation of α clusters in dilute neutron-rich matter*

Tanaka J, Yang Z, Typel S, Adachi S, Bai S, van Beek P, Beaumel D, Fujikawa Y, Han J, Heil S, Huang S, Inoue A, Jiang Y, Knösel M, Kobayashi N, Kubota Y, Liu W, Lou J, Maeda Y, Matsuda Y, Miki K, Nakamura S, Ogata K, Panin V, Scheit H, Schindler F, Schrock P, Symochko D, Tamii A, Uesaka T, Wagner V, Yoshida K, Zenihiro J, Aumann T
Science, 371 (2021) 260-264.

Electric and magnetic dipole strength in Sn 112,114,116,118,120,124

Bassauer S., Von Neumann-Cosel P., Reinhard P.G., Tamii A., Adachi S., Bertulani C.A., Chan P.Y., D'Alessio A., Fujioka H., Fujita H., Fujita Y., Gey G., Hilcker M., Hoang T.H., Inoue A., Isaak J., Iwamoto C., Klaus T., Kobayashi N., Maeda Y., Matsuda M., Nakatsuka N., Noji S., Ong H.J., Ou I., Pietralla N., Ponomarev V.Y., Reen M.S., Richter A., Singer M., Steinhilber G., Sudo T., Togano Y., Tsumura M., Watanabe Y., Werner V.
Physical Review C, 102 (2020) 034327.

Evolution of the dipole polarizability in the stable tin isotope chain

Bassauer S., von Neumann-Cosel P., Reinhard P.G., Tamii A., Adachi S., Bertulani C.A., Chan P.Y., Colò G., D'Alessio A., Fujioka H., Fujita H., Fujita Y., Gey G., Hilcker M., Hoang T.H., Inoue A., Isaak J., Iwamoto C., Klaus T., Kobayashi N., Maeda Y., Matsuda M., Nakatsuka N., Noji S., Ong H.J., Ou I., Paar N., Pietralla N., Ponomarev V.Y., Reen M.S., Richter A., Roca-Maza X., Singer M., Steinhilber G., Sudo T., Togano Y., Tsumura M., Watanabe Y., Werner V.
Physics Letters B, 810 (2020) 135804.

How Different is the Core of ^{25}F from $^{24}O_{g.s.}$?

Tang T.L., Uesaka T., Kawase S., Beaumel D., Dozono M., Fujii T., Fukuda N., Fukunaga T., Galindo-Uribarri A., Hwang S.H., Inabe N., Kameda D., Kawahara T., Kim W., Kisamori K., Kobayashi M., Kubo T., Kubota Y., Kusaka K., Lee C.S., Maeda Y., Matsubara H., Michimasa S., Miya H., Noro T., Obertelli A., Ogata K., Ota S., Padilla-Rodal E., Sakaguchi S., Sakai H., Sasano M., Shimoura S., Stepanyan S.S., Suzuki H., Takaki M., Takeda H., Tokieda H., Wakasa T., Wakui T., Yako K., Yanagisawa Y., Yasuda J., Yokoyama R., Yoshida K., Yoshida K., Zenihiro J.
Physical Review Letters, 124 (2020) 212502.

Spallation and fragmentation cross sections for 168 MeV/nucleon Xe 136 ions on proton, deuteron, and carbon targets

Sun X.H., Wang H., Otsu H., Sakurai H., Ahn D.S., Aikawa M., Fukuda N., Isobe T., Kawakami S., Koyama S., Kubo T., Kubono S., Lorusso G., Maeda Y., Makinaga A., Momiyama S., Nakano K., Nakayama S., Niikura M., Shiga Y., Söderström P.A., Suzuki H., Takeda H., Takeuchi S., Taniuchi R., Watanabe Y., Watanabe Y., Yamasaki H., Yang X.F., Ye Y.L., Yoshida K.
Physical Review C, 101 (2020) 064623.

Quasifree Neutron Knockout Reaction Reveals a Small s -Orbital Component in the Borromean Nucleus ^{17}B

Yang Z.H., Kubota Y., Corsi A., Yoshida K., Sun X.X., Li J.G., Kimura M., Michel N., Ogata K., Yuan C.X., Yuan Q., Authelet G., Baba H., Caesar C., Calvet D., Delbart A., Dozono M., Feng J., Flavigny F., Gheller J.M., Gibelin J., Giganon A., Gillibert A., Hasegawa K., Isobe T., Kanaya Y., Kawakami S., Kim D., Kiyokawa Y., Kobayashi M., Kobayashi N., Kobayashi T., Kondo Y., Korkulu Z., Koyama S., Lapoux V., Maeda Y., Marqués F.M., Motobayashi T., Miyazaki T., Nakamura T., Nakatsuka N., Nishio Y., Obertelli A., Ohkura A., Orr N.A., Ota S., Otsu H., Ozaki T., Panin V., Paschalis S., Pollacco E.C., Reichert S., Roussé J.Y., Saito A.T., Sakaguchi S., Sako M., Santamaria C., Sasano M., Sato H., Shikata M., Shimizu Y., Shindo Y., Stuhl L., Sumikama T., Sun Y.L., Tabata M., Togano Y., Tsubota J., Xu F.R., Yasuda J., Yoneda K., Zenihiro J., Zhou S.G., Zuo W., Uesaka T.
Physical Review Letters, 126 (2020) 082501.

Surface Localization of the Dineutron in ^{11}Li

Kubota Y., Corsi A., Authelet G., Baba H., Caesar C., Calvet D., Delbart A., Dozono M., Feng J., Flavigny F., Gheller J.M., Gibelin J., Giganon A., Gillibert A., Hasegawa K., Isobe T., Kanaya Y., Kawakami S., Kim D., Kikuchi Y., Kiyokawa Y., Kobayashi M., Kobayashi N., Kobayashi T., Kondo Y., Korkulu Z., Koyama S., Lapoux V., Maeda Y., Marqués F.M., Motobayashi T., Miyazaki T., Nakamura T., Nakatsuka N., Nishio Y., Obertelli A., Ogata K., Ohkura A., Orr N.A., Ota S., Otsu H., Ozaki T., Panin V., Paschalis S., Pollacco E.C., Reichert S., Roussé J.Y., Saito A.T., Sakaguchi S., Sako M., Santamaria C., Sasano M., Sato H., Shikata M., Shimizu Y., Shindo Y., Stuhl L., Sumikama T., Sun Y.L., Tabata M., Togano Y., Tsubota J., Yang Z.H., Yasuda J., Yoneda K., Zenihiro J., Uesaka T.
Physical Review Letters, 125 (2020) 252501.

Search for η' Bound Nuclei in the $^{12}C(\gamma,p)$ Reaction with Simultaneous Detection of Decay Products

N. Tomida, N. Muramatsu, M. Niiyama, J. K. Ahn, W. C. Chang, J. Y. Chen, M. L. Chu, S. Daté, T. Gogami, H. Goto, H. Hamano, T. Hashimoto, Q. H. He, K. Hicks, T. Hiraiwa, Y. Honda, T. Hotta, H. Ikuno, Y. Inoue, T. Ishikawa, I. Jaegle, J. M. Jo, Y. Kasamatsu, H. Katsuragawa, S. Kido, Y. Kon, T. Maruyama, S. Masumoto, Y. Matsumura, M. Miyabe, K. Mizutani, H. Nagahiro, T. Nakamura, T. Nakano, T. Nam, T. N. T. Ngan, Y. Nozawa, Y. Ohashi, H. Ohnishi, T. Ohta, K. Ozawa, C. Rangacharyulu, S. Y. Ryu, Y. Sada, M. Sasagawa, T. Shibukawa, H. Shimizu, R. Shirai, K. Shiraishi, E. A. Strokovsky, Y. Sugaya, M. Sumihama, S. Suzuki, S. Tanaka, A. Tokiyasu, Y. Tsuchikawa, T. Ueda, H. Yamazaki, R. Yamazaki, Y. Yanai, T. Yorita, C. Yoshida, M. Yosoi
Physical Review Letters 124 (2020) 202501

**An event excess observed in the deeply bound region of the ^{12}C (K⁻, p) missing-mass spectrum*
Yudai Ichikawa et al.,
Prog. Theor. Exp. Phys. 2020 (2020) 12, 123D01

**Observation of Coulomb-Assisted Nuclear Bound State of $X^{14}N$ System*
S. Hayakawa et al.,
Phys. Rev. Lett. 126 (2021) 062501 (Editors suggestion).

Calcium-regulated phosphorylation systems controlling uptake and balance of plant nutrients.
Saito, S., and Uozumi, N.
Front. Plant Sci., 11 (2020)
doi.org/10.3389/fpls.2020.00044

Functional characterization of multiple PAS domain-containing diguanylate cyclases in Synechocystis sp. PCC6803.
Ishikawa, K., Chubachi, C., Tochigi, S., Hoshi, N., Kojim, S., Hyodo, M.,
Hayakawa, Y., Furuta, T., Kera, K. and Uozumi, N.
Microbiology, 166, 659-668 (2020)
doi.org/10.1099/mic.0.000929

Diverse physiological functions of cation proton antiporters across bacteria and plant cells
Tsujii, M., Tanudjaja E. and Uozumi, N.
Int. J. Mol. Sci., 21 (12), 4566 (2020)

doi.org/10.3390/ijms21124566

Analysis of Arabidopsis TPK2 and KCO3 reveals structural properties required for K+ channel function
Uehara, C., Takeda, K., Ibuki, T., Furuta, T., Hoshi, N., Tanudjaja, E. and Uozumi, N.
Channels 14, 336-346 (2020)
doi.org/10.1080/19336950.2020.1825894

Hik36-Hik43 and Rre6 act as a two-component regulatory system to control cell aggregation in Synechocystis sp. PCC6803
Kera, K., Yoshizawa, Y., Shigehara, T., Nagayama, T., Tsujii, M., Tochigi, S., and Uozumi, N.
Sci. Rep. 10, 19405 (2020)
doi.org/10.1038/s41598-020-76264-2

＊Near-threshold production of antihydrogen positive ion in positronium--antihydrogen collision
Takuma Yamashita, Yasushi Kino, Emiko Hiyama, Svante Jonsell, Piotr Froelich
New Journal of Physics (Fast track communication), 23,(2021),012001-8 pages

Morphological reproductive characteristics of testes and fertilization capacity of cryopreserved sperm after the Fukushima accident in raccoon (Procyon lotor)
Kazuki Komatsu, Tsugumi Iwasaki, Kosuke Murata, Hideaki Yamashiro, Goh Swee Ting Valerie, Ryo Nakayama, Yohei Fujishima, Takumi Ono, Yasushi Kino, Yoshinaka Simizu, Atsushi Takahashi, Hisashi Shinoda, Kentaro Ariyoshi, Kosuke Kasai, Masatoshi Suzuki, Maria Grazia Palmerini, Manuel Belli, Guido Macchiarelli, Toshitaka Oka, Manabu Fukumoto, Mitsuaki A Yoshida, Akifumi Nakata, Tomisato Miura
Reproduction in Domestic Animals, ,56,(2021),484-497

X-ray Spectroscopy of Muonic Atoms Isolated in Vacuum with Transition Edge Sensors.
S Okada, T Azuma, DA Bennett, P Caradonna, WB Doriese, MS Durkin, JW Fowler, JD Gard, T Hashimoto, R Hayakawa, GC Hilton, Y Ichinohe, P Indelicato, T Isobe, S Kanda, M Katsuragawa, N Kawamura, Y Kino, Y Miyake, KM Morgan, K Ninomiya, H Noda, GC O'Neil, T Okumura, CD Reintsema, DR Schmidt, K Shimomura, P Strasser, DS Swetz, T Takahashi, S Takeda, S Takeshita, H Tatsuno, Y Ueno, JN Ullom, S Watanabe, S Yamada

Journal of Low Temperature Physics, 200, (2020) 445–451

External exposure dose estimation by electron spin resonance technique for wild Japanese macaque captured in Fukushima Prefecture

Toshitaka Oka, Atsushi Takahashi, Kazuma Koarai, Yusuke Mitsuyasu, Yasushi Kino, Tsutomu Sekine, Yoshinaka Shimizu, Mirei Chiba, Toshihiko Suzuki, Ken Osaka, Keiichi Sasaki, Yusuke Urushihara, Satoru Endo, Masatoshi Suzuki, Hisashi Shinoda, Manabu Fukumoto

Radiation Measurements,134 (2020) 106315-4 pages

Nucleon form factors and root-mean-square radii on a (10.8 fm)^4 lattice at the physical point

E. Shintani, K.-I. Ishikawa, Y. Kuramashi, S. Sasaki and T. Yamazaki, (PACS Collaboration),

Physical Review D102 (2020) 19902.

****Differential cross sections, photon beam asymmetries, and spin density matrix elements of ω photoproduction off the proton at $E\gamma = 1.3-2.4$ GeV***

N. Muramatsu, J. K. Ahn, W. C. Chang, J. Y. Chen, M. L. Chu, S. Daté, T. Gogami, H. Goto, H. Hamano, T. Hashimoto, Q. H. He, K. Hicks, T. Hiraiwa, Y. Honda, T. Hotta, H. Ikuno, Y. Inoue, T. Ishikawa, I. Jaegle, J. M. Jo, Y. Kasamatsu, H. Katsuragawa, S. Kido, Y. Kon, S. Masumoto, Y. Matsumura, M. Miyabe, K. Mizutani, T. Nakamura, T. Nakano, T. Nam, T. N. T. Ngan, M. Niiyama, Y. Nozawa, Y. Ohashi, H. Ohnishi, T. Ohta, K. Ozawa, C. Rangacharyulu, S. Y. Ryu, Y. Sada, M. Sasagawa, T. Shibukawa, H. Shimizu, R. Shirai, K. Shiraishi, E. A. Strokovsky, Y. Sugaya, M. Sumihama, S. Suzuki, S. Tanaka, A. Tokiyasu, N. Tomida, Y. Tsuchikawa, T. Ueda, H. Yamazaki, R. Yamazaki, Y. Yanai, T. Yorita, C. Yoshida, and M. Yosoi

Physical Review ***C***102(2020)2, 025201

****Observation of a $K^{bar}NN$ bound state in the $^3He(K^-, \Lambda p)n$ reaction***

T.Yamaga, S.Ajimura, H.Asano, G.Beer, C.Berucci, H.Bhang, M.Bragadireanu, P.Buehler, L.Bussog, M.Cargnelli, S.Choi, C.Curceanu, S.Enomoto, H.Fujioka, Y.Fujiwara, T.Fukuda, C.Guaraldo, T.Hashimoto, R.S.Hayano, T.Hiraiwa, M.Iio, M.Iliescu, K.Inoue, Y.Ishiguro, T.Ishikawa, S.Ishimoto, K.Itahashi, M.Iwasaki, K.Kanno, K.Kato, Y.Kato, S.Kawasaki, P.Kienle, H.Kou, Y.Ma, J.Marton, Y.Matsuda, Y.Mizoi, O.Morra, T.Nagae, H.Noumi, H.Ohnishi, S.Okada, H.Outa, K.Piscicchia, Y.Sada, A.Sakaguchi, F.Sakuma, M.Sato, A.Scordo,

M.Sekimoto, H.Shi, K.Shirotori, D.Sirghii, F.Sirghii, K.Suzuki, S.Suzuki, T.Suzuki, K.Tanida, H.Tatsuno, M.Tokuda, D.Tomono, A.Toyoda, K.Tsukada, O.VazquezDocei, E.Widmann, T.Yamazaki, Q.Zhang, J.Zmeskal
Physical Review C(102)4,044002

ωN scattering length from ω photoproduction on the proton near the reaction threshold

T. Ishikawa, H. Fujimura, H. Fukasawa, R. Hashimoto, Q. He, Y. Honda, A. Hosaka, T. Iwata, S. Kaida, J. Kasagi, A. Kawano, S. Kuwasaki, K. Maeda, S. Masumoto, M. Miyabe, F. Miyahara, K. Mochizuki, N. Muramatsu, Nakamura, S. X. Nakamura, K. Nawa, S. Ogushi, Y. Okada, K. Okamura, Y. Onodera, K. Ozawa, Y. Sakamoto, M. Sato, T. Sato, H. Shimizu, H. Sugai, K. Suzuki, Y. Tajima, S. Takahashi, Y. Taniguchi, Y. Tsuchikawa, H. Yamazaki, R. Yamazaki, and H. Y. Yoshida
Phys. Rev. C 101 (2020) 052201(R).

Experimental study of (p, 2p) reactions at 392 MeV on 12C, 16O, 40Ca and 208Pb nuclei leading to low-lying states of residual nuclei

Tetsuo Noro, Tomotsugu Wakasa, Takashi Ishida, Hidetomo P Yoshida, Masahiro Dozono, Hisako Fujimura, Kunihiro Fujita, Kichiji Hatanaka, Takatsugu Ishikawa, Masatoshi Itoh, Junichiro Kamiya, Takahiro Kawabata, Yoshikazu Maeda, Hiroaki Matsubara, Masanobu Nakamura, Harutaka Sakaguchi, Yasuhiro Sakemi, Yohei Shimizu, Hiroyuki Takeda, Yuji Tameshige, Atsushi Tamii, Keisuke Tamura, Satoru Terashima, Makoto Uchida, Yusuke Yasuda, Masaru Yosoi
Progress of Theoretical and Experimental Physics 2020 (9), 093D02 (2020).

****Spectroscopy of A=9 hyperlithium by the (e,e'K+) reaction***

T. Gogami,C. Chen, D. Kawama, P. Achenbach, A. Ahmidouch, I. Albayrak, D. Androic, A. Asaturyan, R. Asaturyan, O. Ates, P. Baturin, R. Badui, W. Boeglin, J. Bono, E. Brash, P. Carter, A. Chiba, E. Christy, S. Danagoulian, R. De Leo, D. Doi, M. Elaasar, R. Ent, Y. Fujii, M. Fujita, M. Furic, M. Gabrielyan, L. Gan, F. Garibaldi, D. Gaskell, A. Gasparian, Y. Han, O. Hashimoto,T. Horn, B. Hu, Ed. V. Hungerford, M. Jones, H. Kanda, M. Kaneta, S. Kato, M. Kawai, H. Khanal, M. Kohl, A. Liyanage, W. Luo, K. Maeda, A. Margaryan, P. Markowitz, T. Maruta, A. Matsumura, V. Maxwell, D. Meekins, A. Mkrtchyan, H. Mkrtchyan, S. Nagao, S. N. Nakamura, A. Narayan, C. Neville, G. Niculescu, M. I. Niculescu, A. Nunez, Nuruzzaman, Y. Okayasu, T. Petkovic, J. Pochodzalla, X. Qiu, J. Reinhold, V. M. Rodriguez, C. Samanta, B. Sawatzky, T. Seva, A. Shichijo, V. Tadevosyan, L. Tang, N. Taniya, K. Tsukada, M. Veilleux, W.

Vulcan, F. R. Wesselmann, S. A. Wood, T. Yamamoto, L. Ya, Z. Ye, K. Yokota, L. Yuan, S. Zhamkochyan, and L. Zhu
Phys. Rev. C, 103, L041301 (2021).
DOI: 10.1103/PhysRevC.103.L041301

Excess Energy Generation using a Nano-sized Multilayer Metal Composite and Hydrogen Gas
Y. Iwamura, T. Itoh, J. Kasagi, S. Murakami and M. Saito,
J. Condensed Matter Nucl. Sci. 33 (2020) 1–13.

Papers Published in Conference Proceedings, Books etc.

Radioactive isotope production via photo nuclear reaction using high power electron linac at ELPH, Tohoku University
S. Kashiwagi, H. Kikunaga, K. Takahashi, F. Hinode, T. Muto, S. Miura, H. Hama
Proc. The 3rd International Conference on Radiation and Emission in Materials (ICREM2021), Chiang Mai, Thailand, December 15-18, (2020).

コヒーレントTHzアンジュレータ放射の偏光スイッチング
柏木 茂, 齊藤 寛峻, 寺田 健人, 石附 勇人, 鹿又 健, 柴田 晃太朗, 髙橋 健, 長澤 育郎,
南部 健一, 日出 富士雄, 三浦 禎雄, 武藤 俊哉, 山田 悠樹, 山本 大喜, 濱 広幸, 全 炳俊, 入澤 明典
日本加速器学会 第17回年会プロシーディングス, (2020), 120-123

アンジュレータ超放射のコヒーレンスを用いた電子ビーム特性測定の検討
寺田 健人, 柏木 茂, 齊藤 寛峻, 石附 勇人, 鹿又 健, 柴田 晃太朗, 髙橋 健, 長澤 育郎, 南部 健一, 日出 富士雄, 三浦 禎雄, 武藤 俊哉, 山田 悠樹, 山本 大喜, 濱 広幸
日本加速器学会 第17回年会プロシーディングス, (2020), 124-126

チェレンコフ放射を用いたビーム位置モニターの開発
南部 健一, 柏木 茂, 鹿又 健, 柴田 晃太朗, 髙橋 健, 長澤 育郎, 日出 富士雄, 三浦 禎雄, 武藤 俊哉, 齊藤 寛峻, 寺田 健人, 石附 勇人, 山田 悠樹, 山本 大喜, 濱 広幸
日本加速器学会 第17回年会プロシーディングス, (2020), 482-484

極短電子ビームによるコヒーレントスミス＝パーセル放射の研究

山田 悠樹，日出 富士雄，柏木 茂，齊藤 寛峻，石附 勇人，寺田 健人，鹿又 健，柴田 晃太朗，高橋 健，南部 健一，三浦 禎雄，武藤 俊哉，濱 広幸

日本加速器学会 第17回年会プロシーディングス, (2020), 853-856

東北大学電子光理学研究センター加速器施設の現状

日出 富士雄，柏木 茂，鹿又 健，柴田 晃太朗，高橋 健，長澤 育郎，南部 健一，三浦 禎雄，武藤 俊哉，濱 広幸

日本加速器学会 第17回年会プロシーディングス, (2020), 934-936

Nb3Sn Formation Using Electroplating Method for SRF Cavity

Hayato Ito, Hitoshi Hayano, Hideaki Monjushiro, Shigeru Kashiwagi, Fuminori Honda, Akihiro, Kikuchi, Emanuela Barzi

Virtual International Workshop on Nb3Sn SRF Science, Technology, and Applications (Nb3SnSRF'20), November 10-13, 2020.

4K高Q値運転可能な超伝導加速空洞のための電気メッキ法によるNb3Sn成膜

井藤隼人，早野仁司，文珠四郎秀昭，柏木茂，本多史憲，菊池章弘

日本加速器学会 第17回年会プロシーディングス, (2020), 193-196.

Half-life of the ground state of Mn-52

H. Kikunaga, H. Ikeda, K. Shirasaki, H. Watabe

CYRIC Annual Report 2018-2019

＊Measurement for p-^{3}He Elastic Scattering with a 65 MeV Polarized Proton Beam

Nakai S., Sekiguchi K., Miki K., Watanabe A., Mukai T., Shibuya S., Watanabe M., Kawahara K., Sakai D., Wada Y., Shiokawa Y., Taguchi T., Eto D., Akieda T., Kon H., Ito M., Ino T., Hatanaka K., Tamii A., Ong H.J., Kobayashi N., Inoue A., Nakamura S., Wakasa T., Mitsumoto S., Ohshiro H., Goto S., Maeda Y., Sakai H., Uesaka T., Wakui T.

Springer Proceedings in Physics, 238 (2020) 513.

＊Structure of Beryllium Isotopes Beyond the Neutron Dripline

Monteagudo B., Gibelin J., Marqués F.M., Corsi A., Kubota Y., Orr N.A., Authelet G., Baba H., Caesar C., Calvet D., Delbart A., Dozono M., Feng J., Flavigny F., Gheller J.M., Giganon A., Gillibert A., Hasegawa K., Isobe T., Kanaya Y., Kawakami S., Kim D., Kiyokawa Y., Kobayashi M., Kobayashi N., Kobayashi T., Kondo Y., Korkulu Z., Koyama

S., Lapoux V., Maeda Y., Motobayashi T., Miyazaki T., Nakamura T., Nakatsuka N., Nishio Y., Obertelli A., Ohkura A., Ota S., Otsu H., Ozaki T., Panin V., Paschalis S., Pollacco E.C., Reichert S., Rousse J.Y., Saito A.T., Sakaguchi S., Sako M., Santamaria C., Sasano M., Sato H., Shikata M., Shimizu Y., Shindo Y., Stuhl L., Sumikama T., Tabata M., Togano Y., Tsubota J., Uesaka T., Yang Z.H., Yasuda J., Yoneda K., Zenihiro J.
Springer Proceedings in Physics, 238 (2020) 331.

Study of Multi-neutron Systems with SAMURAI Spectrometer

Yang Z.H., Marqués F.M., Achouri N.L., Ahn D.S., Aumann T., Baba H., Beaumel D., Böhmer M., Boretzky K., Caamaño M., Chen S., Chiga N., Cortés M.L., Cortina D., Doornenbal P., Douma C.A., Dufter F., Feng J., Fernández-Domínguez B., Elekes Z., Forsberg U., Fujino T., Fukuda N., Gašparić I., Ge Z., Gernhäuser R., Gheller J.M., Gibelin J., Gillibert A., Godoy B.M., Halász Z., Harada T., Harakeh M.N., Hirayama A., Huang S.W., Inabe N., Isobe T., Kahlbow J., Kalantar-Nayestanaki N., Kim D., Kim S., Knösel M.A., Kobayashi T., Kondo Y., Koseoglou P., Kubota Y., Kuti I., Lehr C., Li P.J., Liu Y., Maeda Y., Masuoka S., Matsumoto M., Mayer J., Miki H., Miwa M., Murray I., Nakamura T., Obertelli A., Orr N.A., Otsu H., Panin V., Park S., Parlog M., Paschalis S., Potlog M., Reichert S., Revel A., Rossi D., Saito A., Sasano M., Sato H., Scheit H., Schindler F., Shimada T., Shimizu Y., Shimoura S., Stefan I., Storck S., Stuhl L., Suzuki H., Symochko D., Takeda H., Takeuchi S., Tanaka J., Togano Y., Tomai T., Törnqvsit H.T., Tscheuschner J., Uesaka T., Wagner V., Wimmer K., Yamada H., Yang B., Yang L., Yasuda Y., Yoneda K., Zanetti L., Zenihiro J.
Springer Proceedings in Physics, 238 (2020) 529.

Experimental study of ^{4}n with ^{8}He(p,2p) reaction

Huang S.W., Yang H., Marqués F.M., Achouri N.L., Ahn D.S., Aumann T., Baba H., Beaumel D., Böhmer M., Boretzky K., Caamano M., Chen S., Chiga N., Cortés M.L., Cortina D., Doornenbal P., Douma C.A., Dufter F., Feng J., Fernández-Domínguez B., Elekes Z., Forsberg U., Fujino T., Fukuda N., Gašparić I., Ge Z., Gernhauser R., Gheller J.M., Gibelin J., Gillibert A., Godoy B.M., Halász Z., Harada T., Harakeh M.N., Hirayama A., Inabe N., Isobe T., Kahlbow J., Kalantar-Nayestanaki N., Kim D., Kim S., Knösel M.A., Kobayashi T., Kondo Y., Koseoglou P., Kubota Y., Kuti I., Lehr C., Li P.J., Liu Y., Maeda Y., Masuoka S., Matsumoto M., Mayer J., Miki H., Miwa M., Murray I., Nakamura T., Obertelli A., Orr N., Otsu H., Panin V., Park S., Parlog M., Paschalis S., Potlog M., Reichert S., Revel A., Rossi D., Saito A., Sasano M., Sato H., Scheit H., Schindler F., Shimada T., Shimizu Y., Shimoura S., Stefan I., Storck S., Stuhl L., Suzuki H., Symochko D., Takeda H., Takeuchi S., Tanaka J., Togano Y., Tomai

T., Törnqvsit H.T., Tscheuschner J., Uesaka T., Wagner V., Wimmer K., Yamada H., Yang B., Yang L., Yasuda Y., Yoneda K., Zanetti L., Zenihiro J., Elidiano T.
Journal of Physics: Conference Series, 1643 (2020) 012090.

Spectroscopy of ^{16}B from quasi-free (p,pn) reaction with ^{17}B
Yang Z.H., Kubota Y., Corsi A., Authelet G., Baba H., Caesar C., Calvet D., Delbart A., Dozono M., Feng J., Flavigny F., Gheller J.M., Gibelin J., Giganon A., Gillibert A., Hasegawa K., Isobe T., Kanaya Y., Kawakami S., Kim D., Kiyokawa Y., Kobayashi M., Kobayashi N., Kobayashi T., Kondo Y., Korkulu Z., Koyama S., Lapoux V., Maeda Y., Marqués F.M., Motobayashi T., Miyazaki T., Nakamura T., Nakatsuka N., Nishio Y., Obertelli A., Ohkura A., Orr N.A., Ota S., Otsu H., Ozaki T., Panin V., Paschalis S., Pollacco E.C., Reichert S., Roussé J.Y., Saito A.T., Sakaguchi S., Sako M., Santamaria C., Sasano M., Sato H., Shikata M., Shimizu Y., Shindo Y., Stuhl L., Sumikama T., Sun Y., Tabata M., Togano Y., Tsubota J., Uesaka T., Yasuda J., Yoneda K., Zenihiro J.
Journal of Physics: Conference Series, 1643 (2020) 012162.

Development of a spectrometer for ULQ2 experiment
Y. Honda, T. Aoyagi, C. Legris, T. Goke, K. Ishizaki, H. Kikunaga, Y. Maeda, S. Miura, M. Miyabe, T. Muto, K. Namba, K. Nanbu, S. Sasaki, T. Suda, K. Takahashi, S. Takayama, D. Taki1, T. Tamae, A. O. Tokiyasu, K. Tsukada, N. Tsukamoto, H. Wauke, and Z. Hang
ELPH annual report 2019 (2020) 85-90

Ten Years of the Asian Nuclear Physics Association (ANPhA) and Major Accelerator Facilities for Nuclear Physics in the Asia Pacific Region
Anthony W. Thomas, Andrew E. Stuchbery, Weiping Liu, Guoqing Xiao, Yugang Ma, Jun Cao, Avinash C. Pandey, B. K. Nayak, Sumit Som, Kazuhiro Tanaka, Tohru Motobayashi, Hirokazu Tamura, Atsushi Hosaka, Byungsik Hong
Nuclear Physics News 30 (2020) 3

葉緑体の光合成活性に関わるイオン輸送体の最近の知見と動向
辻井雅，魚住信之
生化学　みにれびゅう　92巻5号　748-752 (2020)

Towards prediction of the rates of antihydrogen positive ion production in collision of antihydrogen with excited positronium

Takuma Yamashita, Yasushi Kino, Svante Jonsell, Emiko Hiyama, Konrad Piszczatowski, Piotr Froelich
Journal of Physics: Conference Series, 1412, (2020), 052012-(7 pages)

Four-body calculation of energy levels of muonic molecule dtμe in muon catalyzed fusion
Motoaki Niiyama, Takuma Yamashita, Yasushi Kino
Journal of Physics: Conference Series,1412 (2020) 222013-222014
Journal of Physics: Conference Series,1412,(2020),222001-222002

＊帰還困難区域に生息するアライグマに対する個体毎の外部被ばく線量評価法の適用の検討
光安優典, 岡壽崇, 高橋温, 小荒井一真, 木野康志, 奥津賢一, 関根勉, 山下琢磨, 清水良央, 千葉美麗, 鈴木敏彦, 小坂健, 佐々木啓一, 藤嶋洋平, Valerie SweeTing Goh, 有吉健太郎, 中田章史, 山城秀昭, 篠田壽, 三浦富智
KEK Proceedings of the 21st Workshop on Environmental, Radioactivity, 144-149 (2020)

飯舘村産コナラの樹皮・幹材における放射性セシウムの分析
田巻廣明, 木野康志, 奥津賢一, 山下琢磨, 関根勉
KEK Proceedings of the 21st Workshop on Environmental Radioactivity, 69-74 (2020)

野生ニホンザルにおける放射性セシウム体内動態解析
漆原佑介、鈴木敏彦、清水良央、鈴木正敏、桑原義和、木野康志、関根勉、篠田壽、青野辰雄、福本学
KEK Proceedings of the 21st Workshop on Environmental Radioactivity, 141-143 (2020)

陽電子原子の三粒子描像による高精度構造解析I：束縛状態
山下琢磨, 木野康志
陽電子科学,15, (2020), 17-27

Incorporation and Accumulation of Strontium-90 in the Hard Tissue of Animals and Their Relationship with Strontium-90 Pollution in the Environment
Kazuma Koarai, Yasushi Kino, Toshitaka Oka, Atsushi Takahashi, Toshihiko Suzuki, Yoshinaka Shimizu, Mirei Chiba, Ken Osaka, Keiichi Sasaki, Yusuke Urushihara, Tomokazu Fukuda, Emiko Isogai, Hideaki Yamashiro, Manabu Fukumoto, Tsutomu Sekine, Hisashi Shinoda

Low-Dose Radiation Effects on Animals and Ecosystems, Springer, Singapore, pp.53-62 (2020)

Analysis of Ovaries and Fertilities in Domestic Animals Affected by the Fukushima Daiichi Nuclear Power Plant Accident

Yasuyuki Abe, Hideaki Yamashiro, Yasushi Kino, Toshinori Oikawa, Masatoshi Suzuki, Yusuke Urushihara, Yoshikazu Kuwahara, Motoko Morimoto, Jin Kobayashi, Tsutomu Sekine, Tomokazu Fukuda, Emiko Isogai, Manabu Fukumoto
Low-Dose Radiation Effects on Animals and Ecosystems, Springer, Singapore, pp.113-123 (2020)

Transgenerational Effects on Calf Spermatogenesis and Metabolome Associated with Paternal Exposure to the Fukushima Nuclear Power Plant Accident

Banri Suzuki, Shigefumi Tanaka, Kohichi Nishikawa, Chikako Yoshida, Takahisa Yamada, Yasuyuki Abe, Tomokazu Fukuda, Jin Kobayashi, Gohei Hayashi, Masatoshi Suzuki, Yusuke Urushihara, Kazuma Koarai, Yasushi Kino, Tsutomu Sekine, Atsushi Takahasi, Toshihiro Shimizu, Hisashi Shinoda, Kazuki Saito, Emiko Isogai, Koh Kawasumi, Satoshi Sugimura, Hideaki Yamashiro, Manabu Fukumoto
Low-Dose Radiation Effects on Animals and Ecosystems, Springer, Singapore, pp.125-138 (2020)

The Effect of Radiation on the Immune System in Pigs Affected by the Fukushima Daiichi Nuclear Power Plant Accident

Motoko Morimoto, Ayaka Kato, Jin Kobayashi, Kei Okuda, Yoshikazu Kuwahara, Yasushi Kino, Yasuyuki Abe, Tsutomu Sekine, Tomokazu Fukuda, Emiko Isogai, Manabu Fukumoto
Low-Dose Radiation Effects on Animals and Ecosystems, Springer, Singapore, pp.139-151 (2020)

Nucleon isovector couplings from 2+1 flavor lattice QCD at the physical point

N. Tsukamoto, Y. Aoki, K.-I. Ishikawa, Y. Kuramashi, E. Shintani, S. Sasaki and T. Yamazaki (PACS Collaboration),
Proceedings of science, LATTICE2019 (2020) 132.

Kbar-Nuclear Bound State at J-PARC

F.Sakuma, S.Ajimura, H.Asano, G.Beer, C.Berucci, H.Bhang, M.Bragadireanu, P.Buehler, L.Bussog, M.Cargnelli, S.Choi, C.Curceanu, S.Enomoto, H.Fujioka, Y.Fujiwara, T.Fukuda, C.Guaraldo, T.Hashimoto, R.S.Hayano, T.Hiraiwa, M.Iio, M.Iliescu, K.Inoue, Y.Ishiguro, T.Ishikawa, S.Ishimoto, K.Itahashi, M.Iwasaki, K.Kanno, K.Kato, Y.Kato, S.Kawasaki, P.Kienle, H.Kou, Y.Ma, J.Marton, Y.Matsuda, Y.Mizoi, O.Morra, T.Nagae, H.Noumi, H.Ohnishi, S.Okada, H.Outa, K.Piscicchia, Y.Sada, A.Sakaguchi, M.Sato, A.Scordo, M.Sekimoto, H.Shi, K.Shirotori, D.Sirghii, F.Sirghii, K.Suzuki, S.Suzuki, T.Suzuki, K.Tanida, H.Tatsuno, M.Tokuda, D.Tomono, A.Toyoda, K.Tsukada, O.VazquezDocei, E.Widmann, T.Yamaga, T.Yamazaki, Q.Zhang, J.Zmeskal
JPS Conf.Proc. 32 (2020) 010088,
Proceedings, 13th International Conference on Nucleus-Nucleus Collisions (NN 2018)

K-pp bound state at J-PARC

F.Sakuma, S.Ajimura, H.Asano, G.Beer, C.Berucci, H.Bhang, M.Bragadireanu, P.Buehler, L.Bussog, M.Cargnelli, S.Choi, C.Curceanu, S.Enomoto, H.Fujioka, Y.Fujiwara, T.Fukuda, C.Guaraldo, T.Hashimoto, R.S.Hayano, T.Hiraiwa, M.Iio, M.Iliescu, K.Inoue, Y.Ishiguro, T.Ishikawa, S.Ishimoto, K.Itahashi, M.Iwasaki, K.Kanno, K.Kato, Y.Kato, S.Kawasaki, P.Kienle, H.Kou, Y.Ma, J.Marton, Y.Matsuda, Y.Mizoi, O.Morra, T.Nagae, H.Noumi, H.Ohnishi, S.Okada, H.Outa, K.Piscicchia, Y.Sada, A.Sakaguchi, M.Sato, A.Scordo, M.Sekimoto, H.Shi, K.Shirotori, D.Sirghii, F.Sirghii, K.Suzuki, S.Suzuki, T.Suzuki, K.Tanida, H.Tatsuno, M.Tokuda, D.Tomono, A.Toyoda, K.Tsukada, O.VazquezDocei, E.Widmann, T.Yamaga, T.Yamazaki, Q.Zhang, J.Zmeskal
AIP. Conf. Proc. 2249(2020)1, 0200005
Proceedings, 15th International Conference on Meson-Nucleon Physics and the Structure of the Nucleon (MENU 2019)

Study on the variation of efficiency and time resolution depending on the electrode material of Resistive Plate Chamber

J. Takahashi, H. Ohnishi, M. Miyabe, A. O. Tokiyasu, Y. Sada, C. Yoshida, H. Saito, M. Turuta, R. Nishikawa, and T. Nobata
ELPH annual report 2019

Performance Evaluations of Resistive Plate Chamber with R1234ze as eco-friendly gas

Ryota NISHIKAWA, Kazuya NOBATA, Junpei TAKAHASHI, and Hiroaki OHNISHI
ELPH annual report 2019

＊Studies for nuclear medium modification of the η′ meson mass at the SPring-8 BGOegg experiment

N. Muramatsu, N. Tomida, Y. Matsumura, J.K. Ahn, W.C. Chang, J.Y. Chen, M.L. Chu, S. Daté, T. Gogami, H. Goto, H. Hamano, T. Hashimoto, Q.H. He, K. Hicks, T. Hiraiwa, Y. Honda, T. Hotta, H. Ikuno, Y. Inoue, T. Ishikawa, I. Jaegle, J.M. Jo, Y. Kasamatsu, H. Katsuragawa, S. Kido, Y. Kon, T. Maruyama, S. Masumoto, K. Miki, M. Miyabe, K. Mizutani, H. Nagahiro, T. Nakamura, T. Nakano, T. Nam, T.N.T. Ngan, M. Niiyama, Y. Nozawa, Y. Ohashi, H. Ohkuma, H. Ohnishi, T. Ohta, M. Oka, M. Okabe, K. Ozawa, C. Rangacharyulu, S.Y. Ryu, Y. Sada, T. Shibukawa, H. Shimizu, R. Shirai, K. Shiraishi, E.A. Strokovsky, Y. Sugaya, M. Sumihama, S. Suzuki, S. Tanaka, Y. Taniguchi, A. Tokiyasu, Y. Tsuchikawa, T. Ueda, H. Yamazaki, R. Yamazaki, Y. Yanai, T. Yorita, C. Yoshida, and M. Yosoi
ELPH Annual Report 2019 (2020) 59–63.

Experimental studies to produce a high energy photon beam by inverse Compton scattering of soft X-rays

Norihito Muramatsu, Masahiro Okabe, Shinsuke Suzuki, Schin Daté, Hajime Shimizu, Haruo Ohkuma, Kazuhiro Kanda, Shuji Miyamoto, Tetsuo Harada, Takeo Watanabe, Manabu Miyabe, and Atsushi Tokiyasu
LASTI Annual Report Vol.21 (2020) 39–41.

BL31LEP (Laser-Electron Photon II)

Masayuki Niiyama and Norihito Muramatsu
SPring-8/SACLA Annual Report 2019 (2020).

Non-strange dibaryons studied in coherent double neutral-meson photoproduction on the deuteron

Takatsugu Ishikawa, Hisako Fujimura, Hiroshi Fukasawa, Ryo Hashimoto, Qinghua He, Yuki Honda, Takahiro Iwata, Shun Kaida, Hiroki Kanda, Jirohta Kasagi, Atsushi Kawano, Shuzo Kuwasaki, Kazushige Maeda, Shin'ichi Masumoto, Manabu Miyabe, Fusashi Miyahara, Keiichi Mochizuki, Norihito Muramatsu, Akihiko Nakamura, Ken'ichi Nawa, Shoei Ogushi, Yasuyuki Okada, Ken'yu Okamura, Yoshihito Onodera, Kyoichiro Ozawa, Yasunobu Sakamoto, Hajime Shimizu, Hiroyuki Sugai, Koutaku Suzuki, Yasuhisa Tajima, Shin'ichiro Takahashi, Yusuke Taniguchi, Yusuke Tsuchikawa, Hirohito Yamazaki, Ryuji Yamazaki, Hiroshi Yoshida

Proceedings, 12th International Workshop on the Physics of Excited Nucleons (NSTAR 2019)
EPJ Web Conf. 241, 01007 (2020).

ωN scattering length from ω photoproduction on the proton near the threshold
Takatsugu Ishikawa, Hisako Fujimura, Hiroshi Fukasawa, Ryo Hashimoto, Qinghua He, Yuki Honda, Atsushi Hosaka, Takahiro Iwata, Shun Kaida, Jirohta Kasagi, Atsushi Kawano, Shuzo Kuwasaki, Kazushige Maeda, Shin'ichi Masumoto, Manabu Miyabe, Fusashi Miyahara, Keiichi Mochizuki, Norihito Muramatsu, Akihiko Nakamura, Satoshi X Nakamura, Ken'ichi Nawa, Shoei Ogushi, Yasuyuki Okada, Ken'yu Okamura, Yoshihito Onodera, Kyoichiro Ozawa, Yasunobu Sakamoto, Mamoru Sato, Toru Sato, Hajime Shimizu, Hiroyuki Sugai, Koutaku Suzuki, Shin'ichiro Takahashi, Yasuhisa Tajima, Yusuke Taniguchi, Yusuke Tsuchikawa, Hirohito Yamazaki, Ryuji Yamazaki, Hiroshi Yoshida
Proceedings of the 15th International Conference on Meson-Nucleon Physics and the Structure of the Nucleon (MENU2019),
AIP Conference Proceedings 2249, 030027 (2020).

Neutron-neutron scattering length from π^+ photoproduction on the deuteron
S.X. Nakamura, T. Ishikawa, T. Sato
arXiv preprint arXiv:2003.02497 (2020).

Development of a silica aerogel Cherenkov detector for π/K separation fitted to the FOREST/BLC experiment
T. Yuzawa, Y. Emoto, K. Fujihara, T. Ishikawa, R. Kanai, H. Kawai, S. Kimata, S. Kimura, A. Kobayashi, M. Miyabe, K. Okuhata, and M. Tabata1 for the FOREST/BLC collaboration
ELPH Annual Report 2019, Research Center for Electron Photon Science, Tohoku University, 81 (2021).

Current status of the FOREST/BLC experiments at ELPH
T. Ishikawa, K. Aoki, H. Fujioka, Y. Honda, T. Hotta, K. Itahashi, H. Kanda, H. Kawai, K. Maeda, Y. Matsumura, M. Miyabe, S. Miyata, N. Muramatsu, H. Ohnishi, K. Ozawa, Y. Sada, H. Shimizu, M. Tabata, A.O. Tokiyasu, and Y. Tsuchikawa for the FOREST/BLC collaboration
ELPH Annual Report 2019, Research Center for Electron Photon Science, Tohoku University, 35 (2021).

Measure of the equality of two distributions

T. Ishikawa

ELPH Annual Report 2019, Research Center for Electron Photon Science, Tohoku University, 31 (2021).

Coherent photoproduction of the neutral pion and etameson on the deuteron

T. Ishikawa, H. Fujimura, H. Fukasawa, R. Hashimoto, Q. He, Y. Honda, T. Iwata, S. Kaida, J. Kasagi, A. Kawano, S. Kuwasaki, K. Maeda, S. Masumoto, M. Miyabe, F. Miyahara, K. Mochizuki, N. Muramatsu, A. Nakamura, K. Nawa, S. Ogushi, Y. Okada, K. Okamura, Y. Onodera, K. Ozawa, Y. Sakamoto, M. Sato, H. Shimizu, H. Sugai, K. Suzuki, Y. Tajima, S. Takahashi, Y. Taniguchi, Y. Tsuchikawa, H. Yamazaki, R. Yamazaki, and H.Y. Yoshida

ELPH Annual Report 2019, Research Center for Electron Photon Science, Tohoku University, 23 (2021).

The performance study of the aerogel Cherenkov counter for the LEPS2-solenoid experiment

C. Yoshida, A.O. Tokiyasu, H. Ohnishi, T. Ishikawa, M. Miyabe, H. Saito, J. Takahashi, and M. Tsuruta

ELPH Annual Report 2019, Research Center for Electron Photon Science, Tohoku University, 51 (2021).

Status of LEPS2-solenoid experiment in 2019

Atsushi Tokiyasu, Yuta Sada, and LEPS2 collaboration

ELPH annual report 2020

****Status of hypertriton binding energy measurements at the Mainz Microtron***

Patrick Achenbach, Sergio Alves Garre, Philipp Eckert, Saül Garcia Orri, Philipp Herrmann, Pascal Klag, Marten Mildeberger, Josef Pochodzalla, Masashi Kaneta, Yoshihiro Konishi, Sho Nagao, Satoshi N. Nakamura, Yuichi Toyama and Toshiyuki Gogami on behalf of the A1 Collaboration

Hadron Spectroscopy and Structure, pp. 713-717 (2020)

https://doi.org/10.1142/9789811219313_0123

****Isospin dependence study of potassium hypernuclei via the high-resolution mass spectroscopy at JLab.***

Sho Nagao, Satoshi N Nakamura, Franco Garibaldi, Pete Markowit, Joerg Reinhold, Liguang Tang, Guido Urciuoli

Bulletin of the American Physical Society, 2020 Fall Meeting of APS Div. of Nucl. Phys.

Status of the experiment of Lambda-n interaction measrement via FSI egffect in gamma+d reaction at ELPH, Tohoku Univ.

Masashi Kaneta, Takeru Akiyama, Hiroyuki Fujioka, Tomomasa Fujiwara, Kenji Fukada, Kousuke Itabashi, Masaya Mizuno, Sho Nagao, Satoshi N. Nakamura, Yuki R. Nakamura, Kazuki Okuyama, Yuichi Toyama, Keita Uehara, Hiroo Umetsu

Bulletin of the American Physical Society, 2020 Fall Meeting of APS Div. of Nucl. Phys.

Inclusive measurement of strangeness photo-production and NΔ resonance state search on a deuterium target

Yuichi Toyama, Masashi Kaneta, Sho Nagao, Satoshi N, Nakamura for NKS2 collaboration

Bulletin of the American Physical Society, 2020 Fall Meeting of APS Div. of Nucl. Phys.

Calibration of Sendai Mass-Flow-Calorimeter and Heat Measurement of Recycled Sample

M. Takeya, T. Itoh, J. Kasagi, Y. Iwamura

Proceedings of the 20th Meeting of Japan CF Research Society JCF20 (Japan CF Research Society, 2020) pp. 106 - 120;

(http://www.jcfrs.org/file/jcf20-proceedings.pdf)

Invited Talk, Oral, and Poster Presentations at International Conferences

RADIOACTIVE ISOTOPE PRODUCTION VIA PHOTO NUCLEAR REACTION USING HIGH POWER ELECTRON LINAC AT ELPH, TOHOKU UNIVERSITY (Invited)

Shigeru Kashiwagi, Hidetoshi Kikunaga, Ken Takahashi, Fujio Hinode, Toshiya Muto, Sadao Miura, Hiroyuki Hama,

The 3rdInternational Conference on Radiation and Emission in Materials, Chiang Mai University, Chiang Mai, Thailand, December 15-18, 2020.

RADIOACTIVE ISOTOPE PRODUCTION VIA PHOTO NUCLEAR REACTION USING HIGH POWER ELECTRON LINAC AT ELPH, TOHOKU UNIVERSITY (Invited)

Shigeru Kashiwagi*, Hidetoshi Kikunaga, Ken Takahashi, Fujio Hinode, Toshiya Muto, Sadao Miura, Hiroyuki Hama,

The 3rdInternational Conference on Radiation and Emission in Materials, Chiang Mai University, Chiang Mai, Thailand, December 15-18, 2020.

Recent Progress of Nuclear Physics in Japan

H. Tamura

ANPHA Symposium 2020, online (hosted by Hong Kong Univ.) Decamber 10, 2020（招待講演）

Gamma-Ray Spectroscopy of Hypernuclei

H. Tamura

Symposium on JPS Nuclear Physics and Physical Review C, JSP fall meeting, online, September 14-17, 2020 （招待講演）.

Elucidation of the mechanism of Na+ and Cs+-induced cell growth through cation transporters

Nobuyuki Uozumi, Masaru Tsujii, Ellen Tanudjaja and Kota Kera

18th International Workshop on Plant Membrane Biology, July 7-12, Glasgow UK

Proton radius measurement with low-energy electron scattering at ELPH

Yuki Honda

he 8th Asia-Pacific Conference on Few-Body Problems in Physics, 1-5 March 2021, Kanazawa

Study of Internal Structure of Unstable Nuclei by Electron Scattering

Hikari Wauke

SNP School 2020, International school of Strangeness Nuclear Physics, Yang Researchers Session, Dec. 2-5(presentation day:4th), J-PARC, Tokai, Japan

Oral presentation (Online)

Proton charge radius measurement

Clement Leglis

CNS summer school 2020, 2020/08/17-21, Wako, Saitama, Japan

Oral presentation (Online)

**Differential cross section of the p(e,e'K+)Λ/Σ0 reaction at Q2～0.5 [(GeV/c)2]*

Kazuki Okuyama et al.

Fall meeting of Division of Nuclear Physics of American Physical Society (APS-

DNP20) (on-line) Oct 30, 2020 口頭発表

Inclusive measurement of strangeness photo-production and N$¥Delta$ resonance state search on a deuterium target

Yuichi Toyama et al.

Fall meeting of Division of Nuclear Physics of American Physical Society (APS-DNP20) (on-line) (2020/11/1) 口頭発表

Development and Performance of Cherenkov Detectors for Spectroscopy of Medium-Heavy Λ Hypernuclei at JLab

Takeru Akiyam

Young Researchers' Session, SNP School 2020, Tokai, Japan 口頭発表

Development of a new ToF counter with MPPC for Λ hypernuclei experiments at ELPH

Tomomasa Fujiwara

Young Researchers' Session, SNP School 2020, Tokai, Japan 口頭発表

Analysis status of ^{3}H(e,e' K$^+$)X at JLab

Kosuke Itabashi

Young Researchers' Session, SNP School 2020, Tokai, Japan 口頭発表

Study of the nnΛ state and Λn interaction at Jefferson Lab

Kosuke Itabashi

Yamada Conference LXXII: The 8th Asia-Pacific Conference on Few-Body Problems in Physics, 2 March 2021, Kanazawa, JAPAN

(ハイブリッド開催) 現地口頭発表、

Search for NΔ resonance state via the exclusive measurement of $\gamma d \rightarrow d\pi^+\pi^-$ reaction

Yuichi Toyama

Yamada Conference LXXII: The 8th Asia-Pacific Conference on Few-Body Problems in Physics, 2 March 2021, Kanazawa, JAPAN (ハイブリッド開催) オンライン口頭発表

Summary of the LGAD test beam at ELPH, Tohoku University

Taikan Suehara,
CALICE Collaboration Meeting, Mar. 2021, Online

学位論文（センター内）

修士（理学）

石附 勇人
「コヒーレントスミス＝パーセル放射を用いた極短電子ビームのバンチ長測定に関する研究」（指導教員：濱 広幸）

寺田 健人
「低エミッタンス極短電子ビームを用いたアンジュレータ超放射のコヒーレンスに関する研究」（指導教員：濱 広幸）

瀧 大祐
「陽子電荷半径測定用電子スペクトロメータの性能評価」（指導教員：須田 利美）

齋藤 肇
「LEPS2 ビームラインにおける光子ビーム透過率測定システムの開発」
（指導教員：大西 宏明）

高橋 準平
「J-PARC におけるチャームバリオン分光実験のための高時間分解能検出器の開発」
（指導教員：大西 宏明）

学位論文（センター外）

修士論文

秋山タケル
「JLab における中重ラムダハイパー核分光実験のための水チェレンコフ測定器の開発」
（指導教員：中村 哲）

奥山 和樹
「p(e,e^' K^+) Λ/Σ^0 反応を用いたハイペロン電磁生成の研究」(指導教員:中村 哲)

Zhao Hang（宮崎大学）

「電子-陽子弾性散乱実験による陽子半径測定のためのポリエチレン標的開発及びイオンチェンバーの性能評価」　（指導教員：前田 幸重）

T. C. Nunes: Osaka University

"Design and Performance Evaluation of a Low-Mass In-Beam Charged Particle Detector for the KOTO Experiment at J-PARC"

指導教員　山中卓

白石諒太　大阪大学

"J-PARC KOTO 実験に用いる高レート荷電粒子検出器のための 信号増幅および波形整形回路の開発 "

指導教員　山中卓

IV. Members of Committees

Steering Committee

2020

HAMA Hiroyuki*	ELPH
SUDA Toshimi	ELPH
OHNISHI Hiroaki	ELPH
HINODE Fujio	ELPH
KASHIWAGI Shigeru	ELPH
MURAMATSU Norihito	ELPH
KIKUNAGA Hidetoshi	ELPH
TAMURA Hirokazu	Graduate School of Science
NAKAMURA Satoshi	Graduate School of Science
SASAKI Shoichi	Graduate School of Science
MISAIZU Fuminori	Graduate School of Science
KINO Yasushi	Graduate School of Science
UOZUMI Nobuyuki	Graduate School of Engineering
MATSUYAMA Shigeo	Graduate School of Engineering
KASADA Ryuta	Institute for Materials Research
TAKAKUWA Yuji	Institute of Multidisciplinary Research for Advanced Materials
EJIMA Takeo	Institute of Multidisciplinary Research for Advanced Materials
EDAMATSU Keiichi	Research Institute of Electrical Communication
ITOH Masatoshi	Cyclotron and Radioisotope Center
TSUDA Kenji	Frontier Research Institute for Interdisciplinary Sciences

* Chairperson

General Advisory Committee

2020

HAMA Hiroyuki*	ELPH, Tohoku University
SUDA Toshimi	ELPH, Tohoku University
OHNISHI Hiroaki	ELPH, Tohoku University
KIKUNAGA Hidetoshi	ELPH, Tohoku University
TAMURA Hirokazu	Graduate School of Science, Tohoku University
KINO Yasushi	Graduate School of Science, Tohoku University
ITOH Masatoshi	Cyclotron and Radioisotope Center, Tohoku University
TSUDA Kenji	Frontier Research Institute for Interdisciplinary Sciences, Tohoku University
UESAKA Tomohiro	RIKEN Nishina Center
HIRENZAKI Satoru	Faculty Division of Natural Science, Nara Women's University
NAKANO Takashi	RCNP, Osaka University
SAWADA Shinya	Institute for Particle and Nuclear Studies, KEK
KATO Ryukou	Accelerator Laboratory, KEK
OHGAKI Hideaki	IAE, Kyoto University
SHINOHAR Atsushi	Graduate School of Science, Osaka University
OURA Yasuji	Graduate School of Science and Engineering, Tokyo Metropolitan University

* Chairperson

Program Advisory Committee

2019

SUDA Toshimi	ELPH, Tohoku University
OHNISHI Hiroaki	ELPH, Tohoku University
KASHIWAGI Shigeru	ELPH, Tohoku University
KIKUNAGA Hidetoshi	ELPH, Tohoku University
NAKAMURA Satoshi*	Graduate School of Science, Tohoku University
SUGIYAMA Kazumasa	Institute for Materials Research, Tohoku University
OZAWA Kyoichiro	Graduate School of Science, KEK2
HOTTA Tomoaki	RCNP, Osaka University
FUJIOKA Hiroyuki	School of Science, Tokyo Institute of Technology
SHOJI Yoshihiko	LASTI, University of Hyogo
GOTO Shin-ichi	Graduate School of Science and Technology, Niigata University
KUBOTA Takumi	Institute for Integrated Radiation and Nuclear Science, Kyoto University

* Chairperson

V. Approved Experiments

2020 年度採択課題

《2020 年度前期申込分》

課題番号	研究代表者	所　属	課　　題　　名	採択シフト
＜素粒子・原子核関連分野＞				
2942	大西 宏明	東北大電子光	新電極素材を使った　Resistive plate chamber (RPC) 建設に向けた基礎研究	2
2943	木河 達也	京大・理	T2K 実験ミューオンモニターのための新型検出器･電子増倍管の電子ビームを用いた性能評価	2
2944	本多良太郎	東北大理	J-PARC E50 実験用 MPPC 読み出し回路の高レート環境下での性能試験	2
＜放射化学物性関連分野＞				
2945	窪田 卓見	京大複合研	カドミウムを標的とした光核反応による無担体放射性パラジウムの製造	2
2946	菊永 英寿	東北大電子光	光量子放射化分析を用いたハロゲン等ルーチン分析のための基礎研究	4
2947	菊永 英寿	東北大電子光	電子ライナックを用いた長寿命/短寿命有用放射性トレーサー製造法の開発 2	12
2948	後藤 真一	新潟大自然科学	Cn の化学研究に向けた Hg の気相化学実験のための無担体 203Hg の製造	3
2949	池田 隼人	東北大 CYRIC/電子光	金の制動放射線照射によるキャリアフリー白金-195m 製造法の検討	2
2950	池田 隼人	東北大 CYRIC/電子光	濃縮同位体を用いた K-43 製造のための新規化学分離法の開発	2
2951	大浦 泰嗣	首都大理	単一コンパレータ光量子放射化分析法による環境試料の元素組成定量	2

《2020 年度後期申込分》

課題番号	研究代表者	所　属	課　　題　　名	採択シフト
＜素粒子・原子核関連分野＞				
2952	佐田 優太	東北大電子光	4 年生学生実験：3 次元飛跡検出器 Time　projection chamber の基礎研究	留保
2953	大西 宏明	東北大電子光	LEPS2/BGOegg 実験用前方陽子識別検出器の開発	2
2954	髙橋 準平	東北大電子光	J-PARC E50 実験のための高時間分解能飛行時間差測定装置試作機の性能評価	2

2955	山中 卓	大阪大	J-PARC KOTO 実験のための、上流 Veto カウンターの性能評価	2
2956	南野 彰宏	横浜国立大	ニュートリノ反応断面積の精密測定に向けた原子核乾板の陽電子に対する性能評価	2
2957	中條 達也	筑波大	ALICE FoCal 実験用　Si-W 電磁カロリメータ検出器に用いる p 型 シリコンセンサの基礎特性評価	2
2958	末原 大幹	九州大	高い時間分解能・位置分解能を実現する新型シリコンセンサーの評価	2
＜放射化学物性関連分野＞				
2959	秋山 和彦	都立大理	光量子放射化法によるプロメチウム（Pm）内包金属フラーレンの合成を目的とした RI 製造　V	2
2960	上坂 充	東京大学	電子ライナックγ線と Ra-226 を用いた Ac-225 生成における炭化ケイ素繊維ターゲットの検討	4
2961	大浦 泰嗣	都立大理	化学分離法検討のための RI トレーサ製造	1

《2020 年度随時申込分》

＜素粒子・原子核関連分野＞			
2962	Jianbei Liu	Univ. of Science and Technology of China Beam test of Ring Imaging CHerenkov (RICH) prototype for CEPC R&D project	-

ELPH Annual Report 2020

(April 2020-March 2021) March 2022
ONLINE ISSN 2435-9165

Published by
Research Center for Electron-Photon Science (ELPH), Tohoku University
1-2-1 Mikamine, Taihaku, Sendai, Miyagi 982-0826, Japan
Phone: +81-22-743-3411
FAX: +81-22-743-3402
Email: koho@lns.tohoku.ac.jp
Homepage: https://www.lns.tohoku.ac.jp/

2022 年（令和 4 年）3 月 31 日 発行
発行者 国立大学法人東北大学電子光理学研究センター
センター長 須田 利美
〒982-0826 宮城県仙台市太白区三神峯 1－2－1
電話： 022-743-3411
FAX： 022-743-3402
Email： koho@lns.tohoku.ac.jp
ホームページ：https://www.lns.tohoku.ac.jp/